NASA CONTRACTOR REPORT 189706

AN INVESTIGATION OF THE THERMOVISCOPLASTIC BEHAVIOR OF A METAL MATRIX COMPOSITE AT ELEVATED TEMPERATURES

John R. Rogacki and Mark E. Tuttle

University of Washington
Seattle, WA 98195

Grant NAG1-974
October 1992

National Aeronautics and Space Administration

LANGLEY RESEARCH CENTER
Hampton, Virginia 23681

TABLE OF CONTENTS

LIST OF FIGURES

An Investigation of the Thermoviscoplastic Behavior of a Metal Matrix Composite at Elevated Temperatures

by

John R. Rogacki, United States Air Force Academy
Mark E. Tuttle, University of Washington

ABSTRACT

This research investigates the response of a fiberless thirteen layer hot isostatically pressed Ti-15-3 laminate to creep, constant strain rate, and cyclic constant strain rate loading at temperatures ranging from 482°C to 649°C. Creep stresses from 48 to 260 MPa and strain rates of .0001 to .01 m/m/sec were used. Material parameters for three unified constitutive models (Bodner-Partom, Miller, and Walker models) were determined for Ti-15-3 from the experimental data.

Each of the three models was subsequently incorporated into a rule of mixtures and evaluted for accuracy and ease of use in predicting the thermoviscoplastic response of unidirectional metal matrix composite laminates (both 0° and 90°). The laminates were comprised of a Ti-15-3 matrix with 29 volume percent SCS_6 fibers. The predicted values were compared to experimentally determined creep and constant strain rate data. It was found that all three models predicted the viscoplastic response of the 0° specimens reasonably well, but seriously underestimated the viscoplastic response of the 90° specimens. It is believed that this discrepancy is due to compliant and/or weak fiber-matrix interphase.

In general, it was found that of the three models studied the Bodner-Partom model was easiest to implement, primarily because this model does not require the use of cyclic constant strain rate tests to determine the material parameters involved. However, the version of the Bodner-Partom model used in this study does not include back stress as an internal state variable, and hence may not be suitable for use with materials which exhibit a pronounced Baushinger effect. The back stress is accounted for in both the Walker and Miller models; determination of the material parameters associated with the Walker model was somewhat easier than in the Miller model.

ACKNOWLEDGEMENTS

This research was funded by the NASA-Langley Research Center via Grant No. NAG-1-974. The authors' are extremely grateful for this support, as well as the patience and many helpful suggestions of the Program Monitor, Dr. W. Steve Johnson.

CHAPTER 1 INTRODUCTION

1.1 Background

In recent years, metal matrix composites (MMCs) have been widely investigated for use in satisfying structural requirements in high temperature, high performance aerospace applications. Titanium alloys reinforced with silicon carbide fibers are currently being considered for use on the National Aerospace Plane (NASP). This type of MMC combines a relatively ductile metal matrix material with stiff, brittle ceramic fibers. Although the thermoviscoplastic behavior of titanium and other metals has been modeled by a number of researchers [2, 7-9, 11, 14, 16-18, 25, 27, 29-31, 42-44, 47-48], the presence of stiff, brittle fibers significantly alters the behavior of MMC's. To date, little has been done to model the thermoviscoplastic behavior of MMC's at elevated temperatures.

The specific MMC studied in this work has a Ti-15-3 matrix reinforced with continuous silicon carbide (SCS_6) fibers. Ti-15-3, a metastable beta strip titanium alloy, is ageable to a high strength and is relatively insensitive to certain corrosive environments. The Ti-15-3 matrix undergoes significant inelastic deformation at elevated temperatures. In contrast, during this study it will be assumed that the SCS_6 fibers deform elastically, even at elevated temperatures.

One of the central issues of this investigation is the selection of a constitutive model capable of accurately predicting the thermoviscoplastic behavior of Ti-15-3. Three thermoviscoplastic constitutive models--the Bodner-Partom, Miller, and Walker models--have been selected for study in this work. The goal of the research described herein is to develop a combined experimental-analytic methodology for predicting the thermoviscoplastic behavior of unidirectional MMC laminates at elevated temperatures.

Because each of these models has previously been used to describe the behavior of one or more thermoviscoplastic materials, it is reasonable to expect that the thermoviscoplastic behavior of Ti-15-3 can be adequately predicted by a modified form of one or more of these models. Furthermore, the experimental parameters

associated with each of these models can be derived from roughly the same database. By generating an appropriate database for Ti-15-3, the predictive power of each of the models can be assessed for the "neat" (fiberless) material. Each model can then be integrated into an appropriate form for a unidirectional laminate using a "rule of mixtures" approach.

1.2 Project Phases

This study was initiated in February 1989 via a grant (NAG-1-974) from the NASA Langley Research Center (LARC). The project was completed in three phases.

- Phase 1: Phase 1 consisted of extensive testing at both UW and LARC using neat Ti-15-3 specimens. During this phase an extensive database for the thermo-viscoplastic response of Ti-15-3 at elevated temperatures was established, and parameters for the three thermoviscoplastic constitutive models were determined. Portions of this work have been reported previously by Rogacki and Tuttle [34-35, 45].

- Phase 2: During Phase 2 the thermoviscoplastic behavior of unidirectional SCS_6/Ti-15-3 MMC's was measured at UW and LARC.

- Phase 3: The "rule of mixtures" formulation (described in Chapter 4) was used to predict the thermoviscoplastic response of unidirectional SCS_6/Ti-15-3 MMC's during Phase 3. This entailed combining the results of Phases 1 and 2 and comparing the predictions with the measurements obtained during the MMC tests.

CHAPTER 2 DESCRIPTION OF LAMINATE MATERIALS

2.1 Laminate

The specific MMC studied was manufactured by Textron Specialty Materials of Lowell, MA, using a Timet Ti-15-3 matrix (a shortened designation for Ti-15V-3Cr-3Al-3Sn) reinforced with continuous SCS_6 fibers made by Textron. The neat laminates consisted of thirteen layers of Ti-15-3 foil joined by hot isostatic pressing (HIP). Although the fiber volume fraction (V_f) was specified as 32%, subsequent analysis of micrographs revealed that the V_f was closer to 29%. (See Figure 2.1. Note: all figures are located at the end of the respective chapters.) The fibered laminates, eight layers thick, had alternating layers of Ti-15-3 foil and continuous SCS_6 fibers joined by hot isostatic pressing.

For the case of strong, brittle SCS_6 fibers in a more ductile Ti-15-3 matrix, the fibers will deform elastically while the matrix deforms first elastically then viscoplastically. As long as the fibers are not degraded by a chemical reaction with the matrix and the composite contains more than a certain minimum volume percent of fibers, the composite will fail at a total strain approximately equal to the strain of the fibers at their ultimate tensile strength [40]. Therefore, the fibers are treated as being purely elastic over the strain ranges encountered in this analysis, and the viscoplastic behavior of the MMC is assumed to be directly attributable to the matrix material.

2.2 Matrix

Ti-15-3 is a metastable beta strip titanium alloy. The alloy is weldable, ageable to high strength, and relatively insensitive to certain corrosive environments. Ti-15-3 also offers cost advantages when compared to some other titanium alloys with comparable properties [38].

Ti-15-3, like other metastable β-Ti alloys, was developed to satisfy the need for strip producible, cold formable, high strength titanium alloys [4]. β-Ti alloys have suppressed β transus temperatures and can be quenched from above the material's β-transus without martensitically decomposing the β-phase. Metastable β-Ti alloys decompose into an α+β mixture upon aging, wherein the α phase has a hexagonal close packed crystalline structure and the β is body centered cubic. Ti-15-3 is solute rich, and, as such, nucleation kinetics are slower than for solute lean alloys. Also, solute rich β-Ti alloys do not form the athermal omega phase. In Ti-15-3, the addition of tin as an alloying ingredient helps suppress omega formation [4]. Grain boundary α is present in essentially all β-Ti alloys, limiting their toughness [15].

In order to optimize ductility, Ti-15-3 is delivered in its metastable beta form. After shaping is completed, the alloy is strengthened (and simultaneously made more brittle) by causing it to a undergo a phase transformation to its stable alpha phase. This aging process is accomplished at temperatures 150-350°F below the β transus (1400 ± 15°F) for varying lengths of time, depending on the aging temperature. In this temperature regime, the α phase precipitates directly [3,20].

Figure 2.2a is a photograph of the "as received" neat Ti-15-3 laminate at 200x magnification. The large beta grain structure is readily apparent. The material was mounted, sanded, polished, and etched with Kroll's reagent prior to the photograph. The dark spots within the photograph are most likely small clusters of the alpha phase which were precipitated during the HIP process. (Some of the spots may also be voids or contaminants within the material.) Since in many places the beta grain boundaries extend across the original lamina interface, the specimens seem to have been very well consolidated during the HIP process. However, the fact that the interfaces are readily apparent after etching indicates preferential alpha formation and/or the possible presence of contaminants on the surfaces of the foil. Figure 2.2b shows a heat treated 13 ply neat Ti-15-3 laminate after creep testing at 566°C (100x magnification). The dark appearance of the specimen indicates the rather widespread precipitation of the alpha phase after aging. No distortion of the beta grains as a result of the creep test is evident.

Ti-15-3 exhibits minimal directionality as 0.0065 inch foil [23]. The alloy has been shown to exhibit significant thermoviscoplastic behavior [15,37]. Final strength is dependent upon aging temperature and prior cold work, with lower aging

temperatures (to approximately 900°F minimum) and greater cold working (to approximately 60% maximum) producing the strongest material [36,41]. The higher the aging temperature, the coarser the α particles [20]. At optimum strength, metastable β-Ti alloys may contain up to 60% α [13]. Ti-15-3 plates less than 0.250 inches thick can be fully solution treated by air cooling without difficulty [2,28].

2.3 Fibers

The fibered laminates tested in this work had continuous SCS_6 (silicon carbide) fibers. The fibers were manufactured by Textron using a chemical vapor deposition (CVD) process. In the CVD process, a carbon monofilament fiber substrate is resistively heated in a tubular glass reactor. Pyrolytic graphite approximately one micron thick is deposited on the substrate to smooth the surface and enhance electrical conductivity. Then, the substrate is exposed to silane and hydrogen gases. The silane (silicon hydride) decomposes to form silicon carbide on the substrate, and the fiber is complete (see Figure 2.1) [12].

SCS_6 fibers are relatively oxidation resistant and retain more of their strength and stiffness at elevated temperatures than other types of ceramic fibers (e.g. boron). The room temperature strength of silicon carbide fibers ranges from 450 to 700 ksi and the modulus of elasticity is in the 60 Msi range [40]. Fiber properties provided by the manufacturer are listed in Table 2.1.

Table 2.1 Room Temperature Physical Properties of SCS_6 fibers [12]

Property	Value
Tensile strength	3400MPa (500ksi)
Tensile modulus	400GPa (60msi)
Coefficient of Thermal Expansion	1.5 $X10^{-6}$/°C (2.7x10^{-6}/°F)

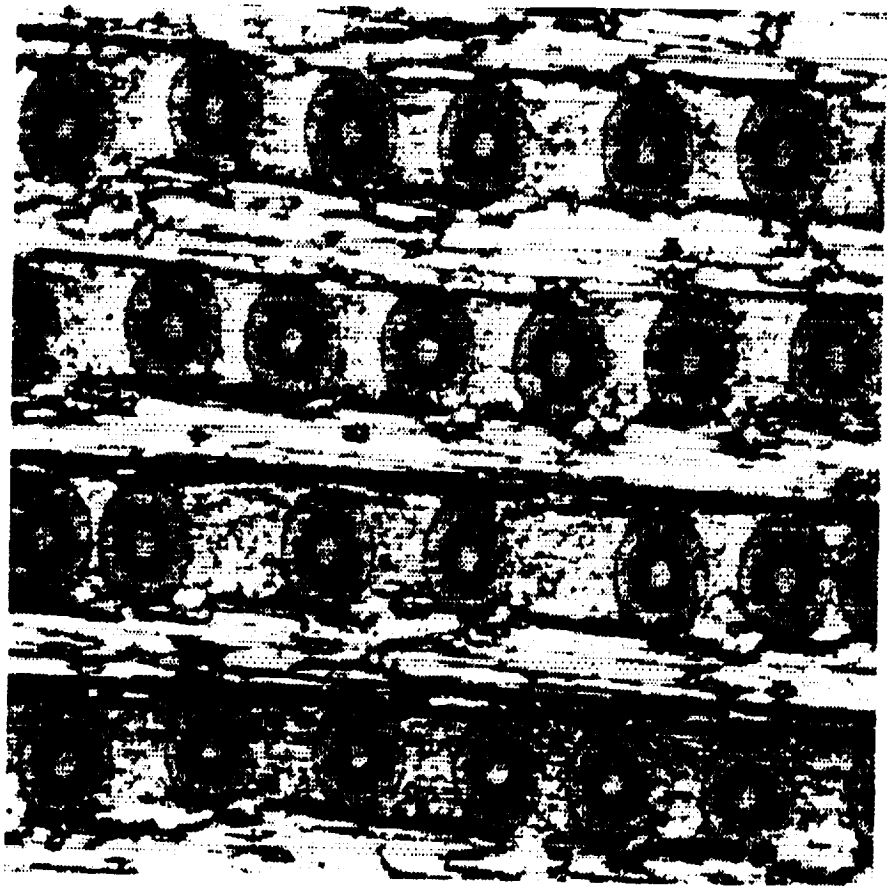

Figure 2.1 Photograph of "as received" Ti-15-3/SCS_6 unidirectional MMC. Note carbon substrate in center of fibers and silicon carbide outer layer. Lightest areas are Ti-15-3.

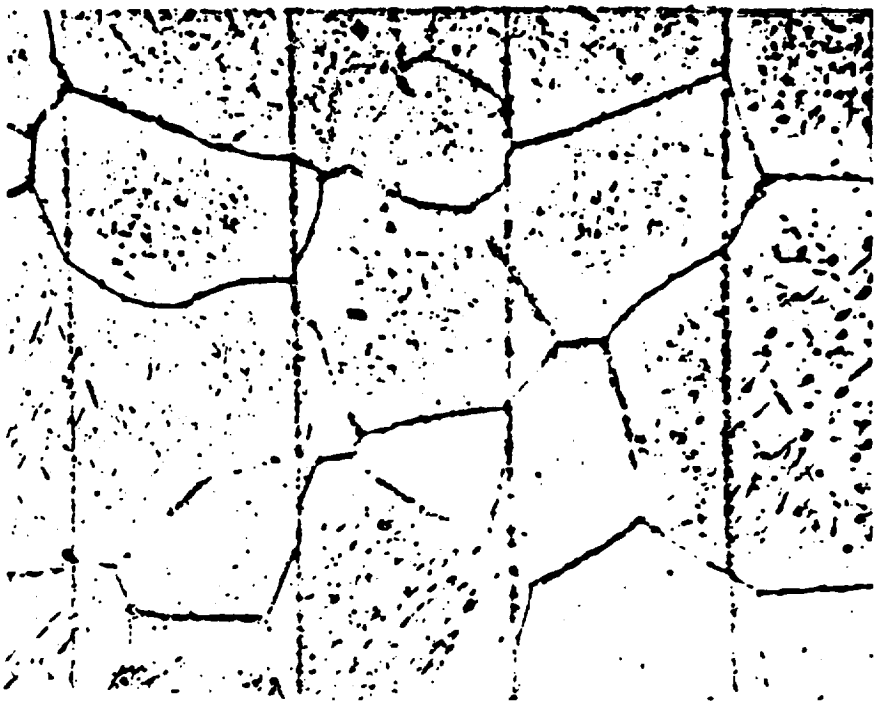

Figure 2.2a Photograph of "as received" neat Ti-15-3 laminate etched with Kroll's reagent (200x). The large beta grain structure is readily apparent. The straight lines are the original lamina interfaces, which were invisible prior to etching.

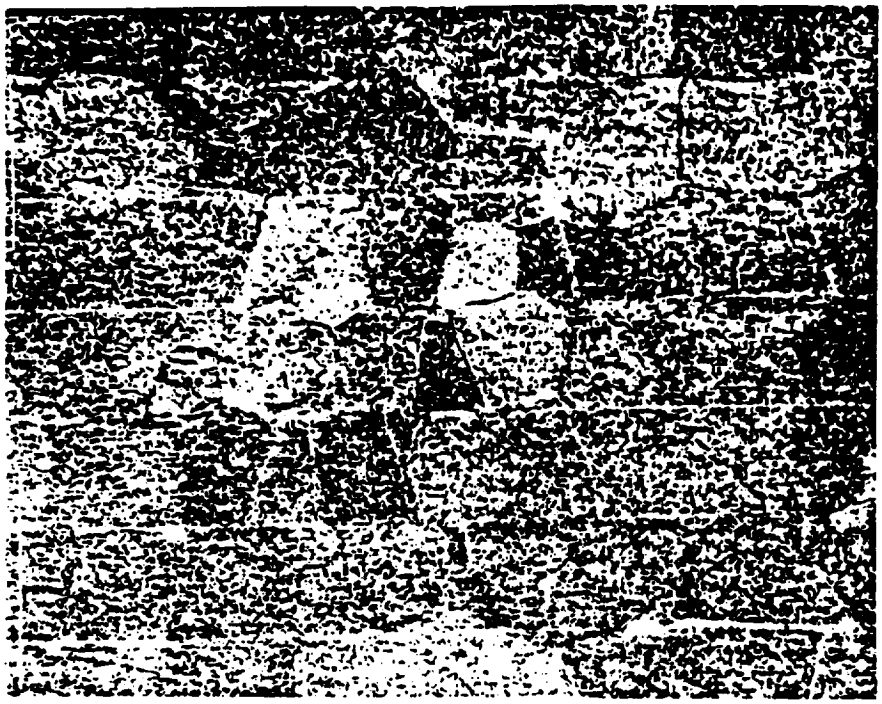

Figure 2.2b Photograph of heat treated 13 ply neat Ti-15-3 laminate after creep testing at 566°C (200x). The dark appearance indicates widespread precipitation of the alpha phase after aging. No distortion of the beta grains as a result of the creep test is evident.

CHAPTER 3 DESCRIPTION OF THERMOVISCOPLASTIC MODELS

3.1 General Description

Early models of inelastic behavior were dependent upon some type of yield function, a plastic or inelastic flow rule, and a hardening rule, and they assumed that plasticity and creep could be separated. Other theories, based upon microphenomenological behavior or thermodynamics, have more recently been proposed to describe inelastic deformation. These models can be further categorized as either unified or uncoupled theories. The two differ in their treatment of time-dependent and time-independent inelastic strain components. The uncoupled theories separate inelastic strain into plastic and creep components; the unified theories do not. It should be noted, however, that there is no formal micromechanical basis for separating the plastic and creep components. Indeed, the two behaviors might be inextricably related [24]. It is this area of unified constitutive modeling that the present work investigates.

3.2 Internal State Variables

The unified constitutive models are based upon a number of state variables which are used to account for elastic and inelastic material behavior [6]. In the general case, state variables include such quantities as applied stress, Young's modulus, internal energy, absolute temperature, heat flux, etc., as well as several internal state variables (ISVs). For the unified constitutive models in particular, the ISVs are specifically used to account for inelastic material behavior. Various constitutive models include or omit different ISV's. Three ISV's of special relevance to the models considered in this study are inelastic strain, back stress, and drag stress.

Inelastic Strain (ε_I), as defined in this work, equals total strain minus elastic and thermal strain. It includes both plastic and creep deformation.

Back stress (B) is a parameter used to account for kinematic hardening. During inelastic deformation, dislocations pile up on slip planes at barriers in the crystal. The pile ups produce a back stress which opposes the applied stress on the slip plane. When the slip direction is reversed, dislocations that previously piled up aid in dislocation movement. This ISV relates to kinematic hardening or the "Bauschinger effect" whereby the tensile plastic deformation of a metal increases the tensile yield strength and decreases the compressive yield strength, or vice-versa. Back stress has also been referred to as "rest" or "equilibrium" stress in the literature [24,27].

Drag stress (D) corresponds to the average dislocation density, which results in isotropic hardening. This ISV accounts for cyclic hardening or softening of the material. The effect of drag stress is similar to isotropic hardening in time-independent classical plasticity [15,42]. Physical mechanisms and microstructural features contributing to drag stress might include grain boundaries, subgrains, dislocation tangles, solute atoms, and precipitate particles [30].

The three thermoviscoplastic models considered in this study all involve two or more of the above ISV's; they differ only in how the evolution of the ISV's with time and loading is described mathematically. However, the procedures described in the literature for evaluating the parameters from experimental data are extremely vague, especially for the Miller and Walker models; a reasonably detailed (and usable) description was found for only the Bodner-Partom model. Therefore algorithms which can be used to determine the parameters involved with each model from experimental data were developed as a part of this study, and will be described in detail in this chapter. In so far as possible these algorithms have been verified by comparison with previous work. For example, the algorithms developed for this study reproduced the published Bodner-Partom parameters for Rene 95 [9] and In 718 [5], as well as the the published Miller and Walker parameters for Hastelloy at 1800°F [24].

3.3 The Bodner-Partom Model

3.3.1 Description

The Bodner-Partom theory is a microphenomonologically based, unified constitutive theory for characterizing inelastic behavior. It assumes that the total strain rate is separable into elastic and inelastic components. The model uses two ISV's: inelastic strain ε_I, and drag stress, D. Strain hardening is related to plastic work. The Bodner-Partom model assumes isotropic material behavior and isothermal conditions. The theory is independent of a yield criterion and loading or unloading conditions. There is no back stress parameter, so the theory cannot account for the Bauschinger effect in kinematic hardening materials. Later modifications to the theory include back stress as an ISV [8]. The Bodner-Partom model is considered especially useful for metals at elevated temperatures where the back stress saturates to a constant value. It is relatively simple to construct, well verified, and requires a minimum of experimentation. Other researchers report that good agreement of analytical and experimental results for commercially pure titanium has been obtained.

For uniaxial loading, Bodner's model may be written [24]:

$$\sigma = E(\varepsilon - \varepsilon_I - \varepsilon_T) \tag{3.1}$$

$$\dot{\varepsilon}_I = \left(\frac{2}{\sqrt{3}}\right)\varepsilon_0 \exp\left[\frac{-(n+1)}{2n}\left\{\frac{\sigma}{D}\right\}^{-2n}\right]\mathrm{sgn}(\sigma) \tag{3.2}$$

$$\dot{D}_I = m(D_1 - D)\,\dot{W}_p - AD_1\left[\frac{D - D_2}{D_1}\right]^r \tag{3.3}$$

$$\dot{W}_p = \sigma\,\dot{\varepsilon}_I \tag{3.4}$$

where ϵ = total strain
ϵ_I = inelastic strain
ϵ_T = thermal strain
E = Young's modulus
W_p = plastic work
D = Drag stress
m, D_1, D_2, r, A, n = material constants
ϵ_0 = limiting value of the inelastic strain rate

The "sgn" function assigns a value of (+1) if the argument is positive and (-1) if the argument is negative.

3.3.2 Data Analysis Procedures

The Bodner-Partom model requires determination of nine constants: E, ϵ_0, n, m, A, r, D_0, D_1, and D_2. Two types of tests are required to determine these constants:

- constant strain rate tensile tests at several strain rates, and

- creep tests at several stress levels for each temperature of interest.

Strain rates and stress levels for the above mentioned tests should be compatible with the values used during numerical simulation.

A diagram of the procedure used to determine the Bodner-Partom constants is shown in Figure 3.1. (Figures are at the end of each chapter.) Young's modulus (E) is determined from the initial stress-strain response when the load is applied at test temperature. The constant ϵ_0 is assumed to be 10^4/sec for all materials, unless the applied strain rates are very high.

The parameters n, m, D_0, and D_1 are obtained from constant strain rate tensile data. When stress reaches a saturated value, equation (3.2) can only be satisfied if D is a constant. Therefore, neglecting recovery (by rapidly loading the specimen), D can be assumed to be in its fully work-hardened condition and at its maximum value, D_1. Equation (3.2) can be written as:

$$\ln\left\{-\ln\left(\frac{\sqrt{3}\varepsilon_I}{2\varepsilon_0}\right)\right\} = -2n\ln(\sigma) + \left[2n\ln D_1 + \ln\left(\frac{n+1}{2n}\right)\right] \qquad (3.5)$$

Therefore, the values of n and D_1 can be obtained by plotting the quanity $\ln\left\{-\ln\left(\frac{\sqrt{3}\varepsilon_I}{2\varepsilon_0}\right)\right\}$ versus $\ln(\sigma)$. The slope of this curve equals -2n, and the y-intercept equals the quanity $\left[2n\ln D_1 + \ln\left(\frac{n+1}{2n}\right)\right]$, from which the value of D_1 can be deduced. An example of this procedure is shown in Figure 3.2.

If work hardening is assumed to be negligible (i.e. during the initial nonlinear portion of the tensile response), and using rapid loading to avoid the effects of recovery, Eq (3.3) becomes:

$$dD = m(D_1 - D)dW_p \qquad (3.6)$$

which can be integrated to give:

$$\ln(D_1 - D) = -mW_p + \ln(D_1 - D_0) \qquad (3.7)$$

where W_p is the inelastic work and D_0 is the drag stress for an annealed (i.e., non cold-worked) material. An expression for D as a function of stress and inelastic strain rate is obtained by inverting Eq (3.2):

$$D = \sigma\left[\left(\frac{2n}{n+1}\right)\ln\left(\frac{2\varepsilon_0}{\sqrt{3}\,\dot{\varepsilon}_I}\right)\right]^{\frac{1}{2n}} \qquad (3.8)$$

Values for D can be obtained by inserting values of stress and inelastic strain rate (taken from several points along the nonlinear portion of the tensile response data) into Eq (3.8). The constants m and D_0 can then be obtained from Eq (3.7). A plot of $\ln(D_1 - D)$ vs W_p (from the constant strain rate tests) gives m (the slope) and D_0 (the intercept).

The constants A, r, and D_2 are computed from data obtained during constant stress creep tests. D_2 is the minimum calculated value of D, found using Eq (3.8). During secondary creep (i.e., where the creep rate is approximately constant), Eq (3.3) becomes:

$$m\,(D_1 - D)\,\dot{W}_p = A\,D_1\left[\frac{D - D_2}{D_1}\right]^r \qquad (3.9)$$

or

$$\ln\left[m\,(D_1 - D)\,\dot{W}_p\right] = r\,\ln\left[\frac{D - D_2}{D_1}\right] + \ln\,(A\,D_1) \qquad (3.10)$$

By plotting the quantity $\ln\left[m\,(D_1 - D)\,\dot{W}_p\right]$ versus the quantity $r\,\ln\left[\frac{D - D_2}{D_1}\right]$, obtained during constant stress creep tests, the slope and intercept define the constants r and A, respectively.

3.4 The Miller Model

3.4.1 Description

The second model considered during this study was proposed by Miller [30, 31]. Like the Bodner-Partom model, Miller's constitutive model is strongly related to underlying microscopic physical mechanisms. Miller's theory consists of a hyperbolic sine strain-rate equation, which represents all of the inelastic strain, plus

work hardening/recovery equations for the two history variables. It contains three ISV's: inelastic strain, back stress, and drag stress.

This model is most suitable for strongly workhardening materials, such as stainless steels. Miller's model has a demonstrated ability to simulate annealing, the effects of warm working, cyclic hardenening, cyclic softening, the Bauschinger effect, and various transient phenomena [6,30]. It does not contain an explicit yield stress, and hence is classified as a unified theory.

On the basis of Young and Sherby's work [49], Miller assumes in the development of his model that the relationship between room temperature yield strength and prior creep stress is insensitive to prior creep temperature. He assumes that drag stress and back stress reach constant values during steady state creep. Miller also assumes that the steady state drag stress during creep, D_{ss}, is independent of creep temperature and that D_{ss} is related to steady state creep stress, σ_{ss}, by a simple relationship. These same assumptions are made in the application of Miller's model to the present study of Ti-15-3.

The uniaxial differential form of Miller's constitutive model can be summarized by the following four equations [24]:

$$\sigma = E(\varepsilon - \varepsilon_I - \varepsilon_T) \tag{3.11}$$

$$\dot{\varepsilon}_I = \beta_c \theta' \left\{ \sinh\left(\frac{\sigma - B}{D} \right)^{\frac{1}{1-m}} \right\}^n \operatorname{sgn}(\sigma - B) \tag{3.12}$$

$$\dot{B} = H_1 \dot{\varepsilon}_I - H_1 \beta_c \theta' \left[\sinh A_1 |B| \right]^n \operatorname{sgn}(B) \tag{3.13}$$

$$\dot{D} = H_2 \left| \dot{\varepsilon}_I \right| \left[C_2 + |B| - \frac{A_2 D^3}{A_1} \right] - H_2 C_2 \beta_c \theta' \left[\sinh(A_2 D^3) \right]^n \tag{3.14}$$

where ε = total strain

ε_I = inelastic strain

ε_T = thermal strain

E = Young's modulus

D = Drag stress

B = Back stress

and

$\beta_c\theta'$, m, n, A_1, A_2, C_2, H_1, H_2, = material constants

The parameter θ', defined by Miller in [30], is related to the activation energy for plastic flow. (Note: θ' is not calculated directly, but is instead determined as part of the term $\beta_c\theta'$.)

3.4.2 Data Analysis Procedure

As discussed in [24], the material parameters for Miller's theory are found through a series of constant strain rate steady state hysteresis loops under fully reversed strain controlled conditions at a constant temperature. The procedure used to determine the material parameters is outlined in Figure 3.3.

During monotonic loading under steady state conditions, the back stress and drag stress are both constant. Setting Eqs (3.13) and (3.14) to zero and solving for the steady state inelastic strain rate:

$$\dot{\varepsilon}_{Iss} = \beta_c\theta'\left[\sinh(A\sigma_{ss})\right]^n \tag{3.15}$$

As shown by Imbrie, Haisler, and Allen, [24] the constant A can be found from the relationship:

$$\left[\frac{\ln \dot{\varepsilon}_4 - \ln \dot{\varepsilon}_5}{\ln \dot{\varepsilon}_1 - \ln \dot{\varepsilon}_5}\right] = \left[\frac{f(\sigma_4) - f(\sigma_5)}{f(\sigma_1) - f(\sigma_5)}\right] \tag{3.16}$$

where f(x) = ln[sinh(Ax)] and σ_1 is the steady state asymptotic stress in a CCSR test conducted at strain rate $\dot{\varepsilon}_1$. The value of "A" which satisfies Eq (3.16) is selected iteratively. Next, from Eq (3.15), the following relationship is derived:

$$\ln(\dot{\varepsilon}_{ss}) = \ln(\beta_c \theta') + n \ln[\sinh(A\sigma_{ss})] \tag{3.17}$$

When values of $\ln(\dot{\varepsilon}_{ss})$ vs $\ln[\sinh(A\sigma_{ss})]$ are plotted, the slope is n and the y intercept is $\ln(\beta_c \theta')$.

The constant "A" does not appear explicitly in (3.12) through (3.14), but it is needed to calculate A_1 and A_2. As shown in [24]:

$$A_2 = [A/(1 - C_1)]^3 \tag{3.18}$$

and

$$A_1 = A/C_1 \tag{3.19}$$

where C_1 is a constant obtainable from the cyclic stress vs cyclic strain data. C_2 and H_1 are also estimated from cyclic stress vs cyclic strain data, using a trial and error best fit procedure. The next parameter to be determined is H_2, which is obtained from a best fit of data from either constant strain rate tensile tests or creep tests. The initial value of back stress is assumed to be zero. The initial value of drag stress, D_0, is found from:

$$D_0 = \frac{\sigma_{ys} - 0.002\,H_1}{\left\{\sinh^{-1}\left[(\dot{\varepsilon}/\beta_c\theta')^{1/n}\right]^{0.677}\right\}} \tag{3.20}$$

where σ_{ys} is the 0.2% offset yield strength at the temperature of interest and a strain rate $\dot{\varepsilon}$.

Two modifications to the theory were necessary during the present study to improve the agreement between experiment and theory. First, a new parameter, H_4, was added to the initial drag stress equation (i.e., Eq 3.20):

$$D_0 = \frac{H_4 (\sigma_{ys} - 0.002 H_1)}{\left\{\sinh^{-1}\left[(\dot{\varepsilon}/\beta_c\theta')^{1/n}\right]^{0.677}\right\}} \qquad (3.21)$$

Inclusion of this new parameter permitted modelling of the inverse strain rate sensitivity observed at 482°C.

Second, H_4 as well as a second new parameter, H_3, were added to the relationship for back stress rate (i.e., Eq 3.13):

$$\dot{B} = H_3 H_4 \{H_1 \dot{\varepsilon}_1 - H_1 \beta_c \theta' \left[\sinh A_1 |B|\right]^n \text{sgn}(B)\} \qquad (3.22)$$

Together parameters H_3 and H_4 increase the strain rate sensitivity of the model with temperature, in accordance with measurements obtained during the present study at 562 and 649°C. In order to reach the desired asymptotic stress extremes for the range of strain rates, the simulated CCSR curves were less "squared" then the experimental curves. A closer agreement between simulated and expermental CCSR data is obtainable by including the parameter H_3 in the model. The constants H_3 and H_4 are determined from a trial and error best fit of the CCSR data. A comparison of predicted response to experimental results is presented in Chapter 6. Thus, the parameters to be determined for the (modified) Miller model are E, $\beta_c\theta'$, n, H_1, H_2, H_3, H_4, A_1, A_2, C_2, and D_0.

3.5 The Walker Model

3.5.1 Description

Walker's constitutive theory [47] is based upon a nonlinear modification to a three-parameter solid (a spring and Voigt element in series). It contains three ISV's: back stress, drag stress, and inelastic strain. The growth law for the back stress contains both dynamic and static recovery terms. (A dynamic term differs from a static term in that a dynamic term is activated only in the presence of an inelastic strain rate.) In Walker's theory, at "high" strain rates the static recovery term is assumed insignificant compared to the dynamic recovery term and the back stress becomes independent of strain rate. Only dynamic recovery terms are included in the growth law for the drag stress. Creep, relaxation and strain rate effects are modeled by a power law for the inelastic strain rate, and all of the material constants in the theory are functions of temperature and must be determined experimentally for each temperature of interest. Walker obtained favorable results from tests of nickel based Hastelloy-X at high temperatures. For uniaxial conditions the Walker model is represented by the following 6 equations:

$$\sigma = E(\varepsilon - \varepsilon_I - \varepsilon_T) \tag{3.23}$$

$$\dot{\varepsilon}_I = \frac{\left|\sigma - B\right|^{n-1}}{Dn}(\sigma - B) \tag{3.24}$$

$$\dot{B} = (n_1 + n_2)\dot{\varepsilon}_I - (B - \mathring{B} - n_1\varepsilon_I)\dot{G} \tag{3.25}$$

$$\dot{D} = n_8\left|\dot{\varepsilon}_I\right| - n_9\left|\dot{\varepsilon}_I\right|D - n_{10}(D - D_0)^q \tag{3.26}$$

$$\dot{G} = \left|\dot{\varepsilon}_I\right|\frac{\delta}{\delta R}\left[(n_3 + n_4 R)\ln\left(\frac{n_5 R}{1 + n_6 R} + 1\right) + n_7\left|B - \dot{B}\right|^{m-1}\right] \tag{3.27}$$

$$R = \int_0^t \left| \frac{\delta \varepsilon_I}{\delta t'} \right| dt' \qquad (3.28)$$

Walker's model requires determination of 16 constants. However, if one assumes drag stress to be constant (as Walker did for Hastelloy-X), the number of constants is reduced to nine, and the growth law for back stress (Eq 3.25) is simplified to:

$$\dot{B} = (n_1 + n_2)\,\dot{\varepsilon}_I - (B - \overset{\circ}{B} - n_1 \dot{\varepsilon}_I)\left[n_9\,\dot{\varepsilon}_I + n_7 \left| B - \overset{\circ}{B} \right|^{m-1} \right] \qquad (3.29)$$

leaving only 9 parameters to be determined: E, n, m, n_1 , n_2 , n_7 , n_9 , $\overset{\circ}{B}$, and D. Thus, equations (3.23) and (3.24) remain unchanged by this simplifying assumption, while the drag stress is constant, and hence Eq (3.26) becomes $\dot{D} = 0$. This simplifying assumption was also made during this study.

3.5.2 Data Analysis Procedure

The procedure used to determine the parameters for Walker's model is outlined in Figure 3.4. Walker's theory requires two types of tests:

- fully reversed cyclic stress-strain tests over various strain rates and temperatures;

- stress relaxation tests starting from different points on steady state hysteresis loops.

The first material parameter to be determined is $\overset{\circ}{B}$. (The reader is cautioned to distinguish between the material parameter $\overset{\circ}{B}$ and the time rate of change in back

stress, $\dot{B}$.) Since the back stress saturates to a constant value as ε_1 approaches ∞ (assuming $n_1 = 0$), Walker showed that for rapid cyclic loading:

$$\dot{B} = \frac{1}{2}\left(\sigma^t_{max} - \sigma^c_{max}\right) \tag{3.30}$$

where σ^t_{max} and σ^c_{max} are the maximum values of tensile and compressive stress.

For large strains,

$$\sigma = B + D(\dot{\varepsilon})^{1/n} \tag{3.31}$$

In terms of steady state values of σ and B in tension,

$$\dot{\varepsilon} = \left[\frac{\sigma^t_{max} - B^t_{max}}{B}\right]^n \tag{3.32}$$

If σ_1 and σ_2 denote the maximum tensile stresses at the two maximum strain rates, $\dot{\varepsilon}_1$ and $\dot{\varepsilon}_2$, (B attains its saturated values for each strain rate at these stresses) then:

$$n = \frac{\ln\left\{\frac{\dot{\varepsilon}_1}{\dot{\varepsilon}_2}\right\}}{\ln\left\{\frac{\sigma_1 - B^t_{max}}{\sigma_2 - B^t_{max}}\right\}} \tag{3.33}$$

and

$$D = (\sigma_1 - B^t_{max})(\dot{\varepsilon})^{-1/n} \tag{3.34}$$

The constant B^t_{max} is determined using stress drop tests, as follows. A point is sought on the hysteresis loop such that the creep rate is initially zero when the stress is held at a constant value. Walker indicates that this is difficult to do because the creep rates are usually very small during unloading. He suggests using a relaxation test, in which the strain level at which the initial relaxation changes from positive (stress decrease) to negative (stress increase) is determined. This procedure was used during this study. During one CCSR test at each temperature (tests L22 through L24), the specimen was cyclically loaded until a steady state hysteresis loop developed. Then, during the unloading portion of the test, the strain was held at a predetermined value, allowing the specimen to relax. The stress vs time data was recorded to determine the initial stress rate during relaxation. After several minutes the specimen was again cycled until a steady state hysteresis loop developed. This procedure of cyclic loading followed by relaxation was repeated five times at each temperature, stopping at a different strain value each time. A best fit of the data from the five points at each temperature was subsequently used to estimate the strain at which the initial relaxation stress rate was zero.

Constants n_2 and n_9 are determined from the initial monotonic stress-strain curve. For rapid loading rates,

$$n_1 = 0 \qquad \text{and} \qquad \dot{G} = n_9 \dot{R}$$

where R is the cumulative inelastic strain. Therefore,

$$B = \overset{\circ}{B} + (B^t_{max} - \overset{\circ}{B}) \left\{1 - \exp[-n_9(\varepsilon - \sigma/E)]\right\} \tag{3.35}$$

Also,

$$n_9 = \left(\varepsilon - \frac{\sigma}{E}\right)^{-1} \ln\left[\frac{B^t_{max} - \overset{\circ}{B}}{B^t_{max} - \sigma + D(\dot{\varepsilon})^{1/n}\left\{1 - \frac{d\sigma}{E\,d\varepsilon}\right\}^{1/n}}\right] \tag{3.36}$$

where $d\sigma/d\varepsilon$ is the instantaneous slope of the uniaxial monotonic stress-strain curve at the point where the stress is σ and the strain is ε. Constant n_2 can then be estimated by:

$$n_2 = \frac{B^t_{max} - \overset{\circ}{B}}{n_9} \tag{3.37}$$

The final two constants, m and n_7, are determined as follows. At the peaks of the hysteresis loops, $\dot{B} = \dot{\sigma} = 0$ for tensile loadings, and it can be shown for these conditions:

$$n_2 \dot{\varepsilon}_4 = (B_4 - \overset{\circ}{B})\, n_9 \dot{\varepsilon}_4 + n_7 (B_4 - \overset{\circ}{B})^m \tag{3.38}$$

and

$$n_2 \dot{\varepsilon}_5 = (B_5 - \overset{\circ}{B})\, n_9 \dot{\varepsilon}_5 + n_7 (B_5 - \overset{\circ}{B})^m \tag{3.39}$$

If σ_4 and σ_5 denote the maximum tensile stresses at the two smallest strain rates, $\dot{\varepsilon}_4$ and $\dot{\varepsilon}_5$, B_4 and B_5 (the saturated back stresses for these two strain rates) may be determined by equation (3.31). Then, combining (3.38) and (3.39), m is obtained by:

$$m = \frac{W_1}{W_2} \tag{3.40}$$

where

$$W_1 = \ln\left[\frac{n_2 \dot{\varepsilon}_4 - n_9 \dot{\varepsilon}_4 (B_4 - \overset{\circ}{B})}{n_2 \dot{\varepsilon}_5 - n_9 \dot{\varepsilon}_5 (B_5 - \overset{\circ}{B})}\right] \tag{3.41}$$

and

$$W_2 = \ln\left[\frac{B_4 - \mathring{B}}{B_5 - \mathring{B}}\right] \tag{3.42}$$

Once m is known, n_7 may be found from (3.38) or (3.39).

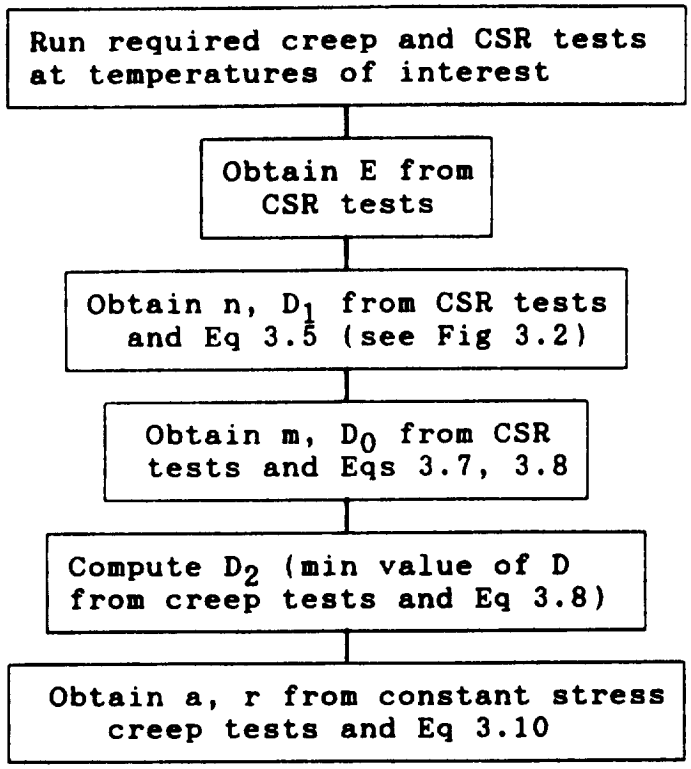

Figure 3.1 Determination of Bodner-Partom model parameters.

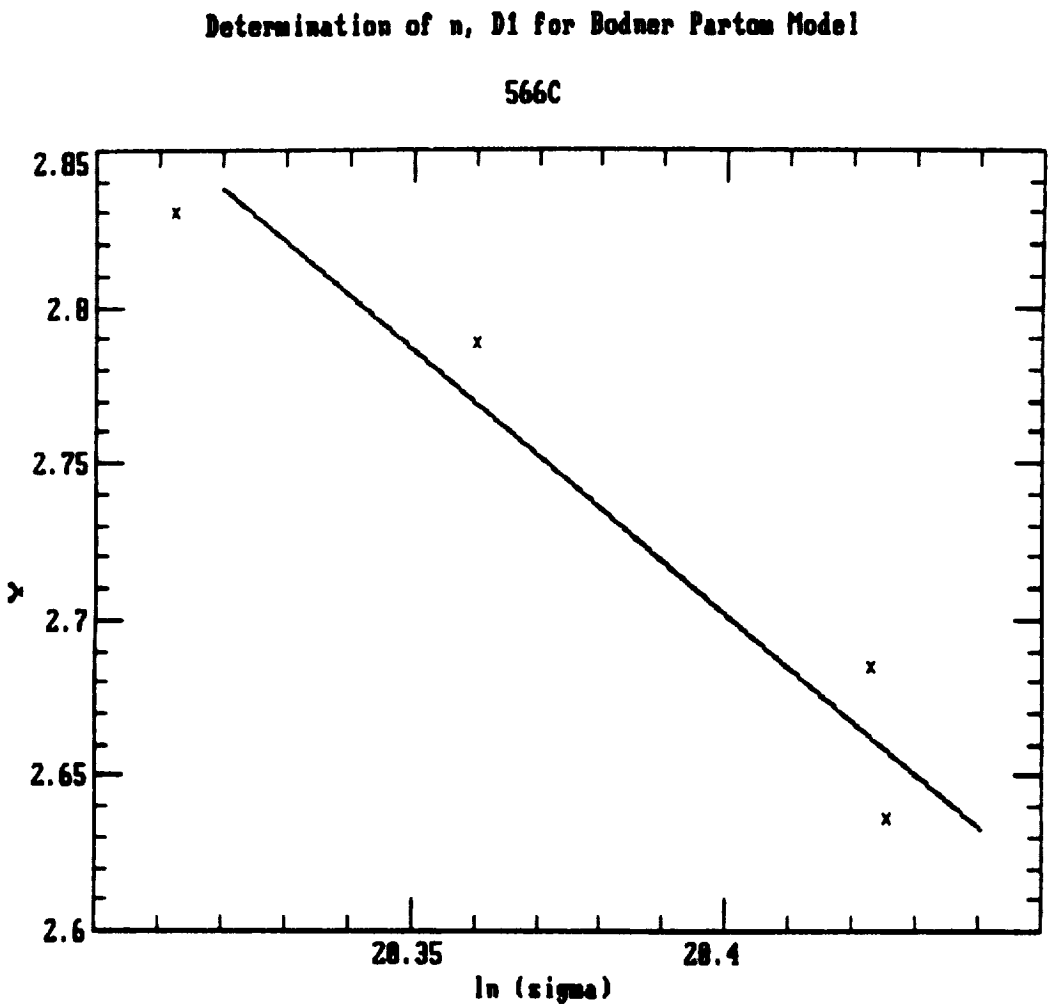

Fig 3.2 Plot of $\ln\left[-\ln\left(\frac{\sqrt{3}\,\epsilon_I}{2\,\epsilon_0}\right)\right]$ vs $\ln\sigma$

where "Y" = $\ln\left[-\ln\left(\frac{\sqrt{3}\,\epsilon_I}{2\,\epsilon_0}\right)\right]$.

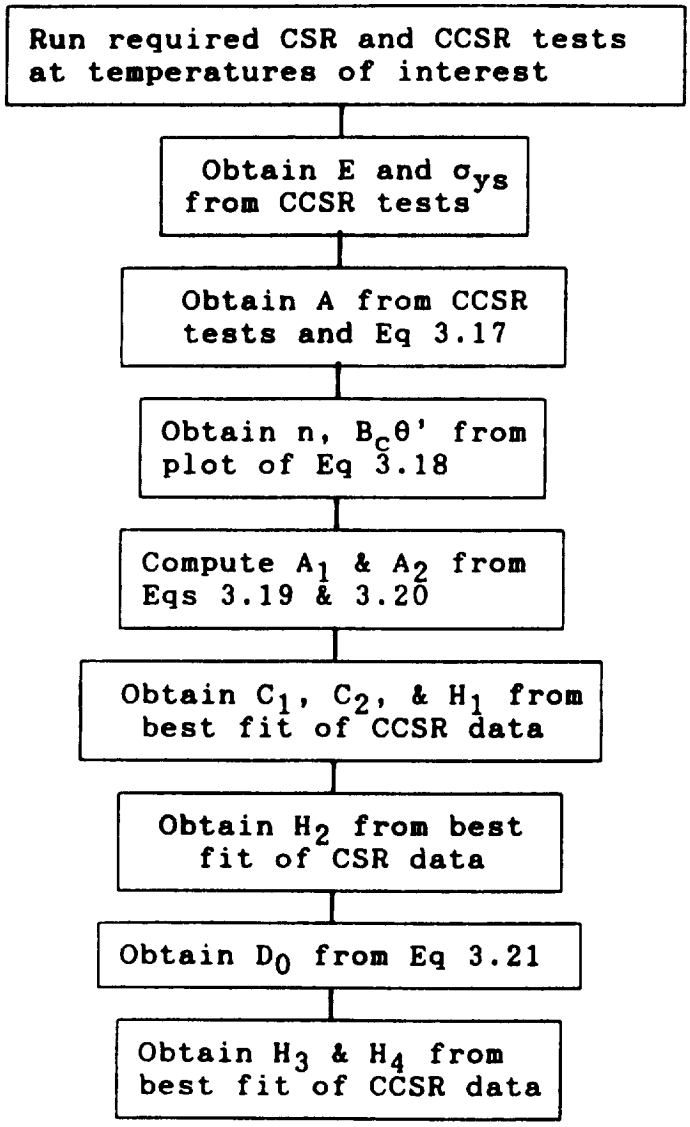

Figure 3.3 Determination of Miller model parameters.

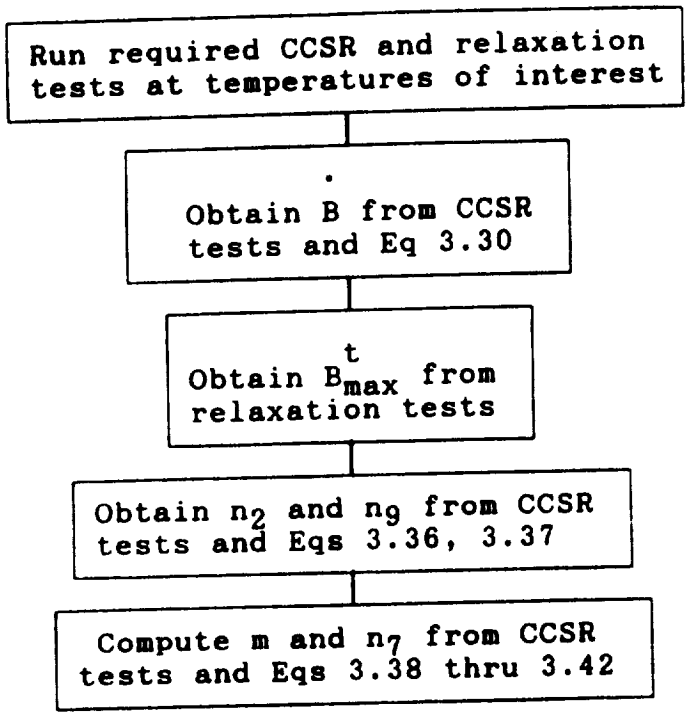

Figure 3.4 Determination of Walker model parameters.

CHAPTER 4 EXPERIMENTAL PROCEDURES AND EQUIPMENT

4.1 Test Matrix

Tables 4.1 and 4.2 contain details of the creep, constant strain rate, and cyclic constant strain rate tests completed in this program. The purpose of these tests was to build a data base for Ti-15-3, determine the experimental parameters required for the three constitutive models, and to verify and evaluate each of the models for use in a rule of mixtures formulation for unidirectional laminates. The following abbreviations are used in the tables:

SSC - single step creep

MSC - multistep creep

CSR - constant strain rate

CCSR - cyclic constant strain rate

4.2 Test Equipment and Facilities

Testing for this program was accomplished at the University of Washington and at NASA Langley Research Center. In addition, a small amount of verification took place at the United States Air Force Academy.

4.2.1 University of Washington

Tests at the University of Washington were accomplished using a SATEC Model G creep rupture tester (#G-2860-P). The tester features a power positioning resistance furnace, automatic load leveling, and a choice of 6:1 or 30:1 lever arm ratio. Three type K Chromel-Alumel thermocouples monitored temperature in the gage length (center two inches) of each specimen. The temperature data was recorded on a Fluke

model 2200B Datalogger (#3425007). Displacements were measured by a SATEC Model 200 extensometer in conjunction with an ATS Linearly Varying Displacement Transducer (LVDT). The LVDT was used to measure displacements and hence strains over a 5.08 cm (2.0 in) gage length. The LVDT had a linear displacement range of 0.050 inches. The input voltage (6.5V) for the LVDT was supplied by a Fluke 3330B Programmable constant voltage calibrator (#2111011). Displacement data was recorded on an IBM PC/AT using an IBM PC Data Acquisition and Control Adaptor.

4.2.2 NASA Langley Research Center

Tests at NASA LARC were run using two MTS Model 810 Servo-hydraulic Material System Testers with Instron hydraulically activated grips. One tester featured an induction furnace which used two infrared pyrometers for temperature control, while the other had a quartz lamp heating system equipped with thermocouples for temperature control. Displacements were measured by quartz-rod extensometers having a 1 inch gage length and a ± 0.15 inch linear range. Data was recorded with Nicolet XF-44 Data Storage systems backed by an X-Y analog plotter.

4.3 Test Specimens

4.3.1 Creep Test Specimens

All of the neat specimens used for creep tests consisted of thirteen plies of Ti-15-3 foil, hot isostatically pressed, as manufactured by Textron for NASA LARC. The nominal specimen dimensions for the neat specimens was 0.145 X 1.27 X 15.25 cm. The fibered specimens were eight plies thick with nominal specimen dimensions of 0.18 X 1.91 X 15.25 cm. All specimen material was received in the annealed condition and subsequently aged at 649°C for one hour prior to testing to precipitate the alpha phase and stabilize the microstructure.

4.3.2 Constant Strain Rate Test Specimens

The neat specimens used for CSR tests, like those used for creep tests, consisted of thirteen plies of hot isostatically pressed Ti-15-3 foil. Nominal specimen dimensions for the neat CSR specimens were the same as described in Section 4.3.1 for creep test specimens.

4.3.3 Cyclic Constant Strain Rate Test Specimens

Because of the requirement in both Miller's and Walker's models for fully reversed, strain-controlled cyclic loading, the parameters for these models were not attainable from the thin axially loaded neat specimens which were initially available for this work. The thin laminated specimens, preferable because they more closely resemble the fibered specimens, could not be used for CCSR testing because they buckle when subjected to compressive loads sufficiently high to cause plastic deformation. Therefore, thicker specimens were required for these tests. The specimens used for CCSR tests were machined from a 0.64 cm thick solid (not laminated) plate of Ti-15-3. All CCSR specimen material was received in an annealed condition and subsequently aged at 649°C for one hour prior to testing.

4.4 Test Procedures

Before each test, specimen dimensions were recorded, test equipment was warmed up, and associated computer equipment for test control and data acquisition was programmed. Finally, in order to stabilize the microstructure and simulate use conditions, the test specimens were aged at 649°C for one hour.

4.4.1 Creep Tests

Two types of creep tests were accomplished at the University of Washington: single step creep (SSC) and multi-step creep (MSC). During the creep tests, constant tensile loads were applied to each specimen using the lever arm creep frame. The resulting axial strain was recorded as a function of time. SSC tests on neat specimens

were conducted at three different temperatures--482, 566, and 649°C (900, 1050, and 1200°F)--and five different stresses--34.5, 69, 103.4, 138, and 172.4 MPa (5, 10, 15, 20 and 25 ksi). The MSC tests were designed to represent a "complex" load history. Two creep tests were accomplished using fibered specimens. Details concerning the creep tests are given in Table 4.1.

4.4.2 Constant Strain Rate Tests

Two types of tests were conducted at NASA LaRC: CSR and CCSR tests. In the constant strain rate tests, a variable tensile load was applied such that a constant strain rate was induced in the specimen. The CSR tests were accomplished at five different strain rates (1×10^{-4}, 5×10^{-4}, 1×10^{-3}, 5×10^{-3}, and 1×10^{-2}/sec) and three different temperatures--482, 566, and 649°C (900, 1050, and 1200°F)--for a total of 15 tests. These 15 tests were done on neat (fiberless) specimens. Additionally, CSR tests were completed on four fibered specimens. The neat CSR specimens were strained to approximately 6%, while the fibered specimens were strained to approximately 0.67%.

4.4.3 Cyclic Constant Strain Rate Tests

Fully-reversed strain-controlled loading was required for the CCSR tests. In the cyclic constant strain rate tests, a variable tensile load was applied such that a constant strain rate was induced in the specimen. At a predetermined strain limit (normally 0.9 or 1.0% strain, except as noted below), the load was reversed. In most cases, the specimens were tested for a minimum of 20 cycles, or until the hysteresis loop stabilized.

Five different strain rates were used for the CCSR tests--1×10^{-4}, 5×10^{-4}, 1×10^{-3}, 5×10^{-3}, and 1×10^{-2}/sec--and three different temperatures--482, 566, and 649°C (900, 1050, and 1200°F)--for a total of 15 tests. These 15 tests were done on neat (fiberless) specimens.

As previously mentioned, three of the CCSR tests (tests L22, 23, and 24) were specifically modified to accomodate the Walker model. After the material response was stabilized during the CCSR tests, the strain was stopped at a predetermined value and stress relaxation behavior was measured. After a period of time the cycling was reinitiated until the response was again stabilized, and then the strain was stopped at a different value. This process was continued until relaxation was measured at a total of five different strain values.

Three other CCSR tests were altered to accomodate the Miller model (tests L25, 26, and 27). In these tests, the strain limits were increased in five increments from ±0.2 to ±1.2%. The specimens were cycled approximately 30 to 40 times within each of the limits before proceeding to the next.

4.5 Algorithms For Application of Models

The following relationships were used in computing the unidirectional laminate longitudinal (E_1) and transverse (E_2) moduli:

$$E_1 = E_f V_f + E_m V_m \tag{4.1}$$

$$E_2 = \frac{E_f E_m}{E_f V_m + E_m V_f} \tag{4.2}$$

where: E_f = elastic modulus of the fibers

E_m = elastic modulus of the matrix

V_f = volume fraction of fibers

V_m = volume fraction of matrix

As is typical with rule of mixtures analyses, it was assumed that the fiber and matrix strains were equal in the longitudinal direction, and the fiber and matrix stresses were equal in the transverse direction. Outlines of the computer algorithms are supplied below.

4.5.1 Constant Strain Rate Tests Using Neat or 0° Unidirectional Specimens

The algorithm used for predicting the CSR response of either neat or 0° unidirectional laminated specimens is shown in Figure 4.1. First, the desired theory for modeling the thermoviscoplastic response of the matrix is selected. As previously mentioned, the fibers are assumed to deform elastically. Next, the volume fraction of fibers (V_f) is input and the volume fraction of matrix material (V_m) is calculated. When simulating a test with a neat specimen, the volume fraction of fibers is set equal to zero. Each of the constitutive models has a number of constants (e.g. Young's modulus for fibers and matrix, initial value of drag stress, etc.), and these are input next along with program parameters. Program parameters for the constant strain rate tests are strain rate, time step size, and time limit. The longitudinal modulus (E_1) is computed using Eq 4.1, and the initial elastic strain of the composite (ε_c), matrix stress (σ_m), and fiber stress (σ_f) are found.

Once the initial steps are completed, iteration with respect to time begins. Time is increased incrementally as before, and for each time increment matrix incremental inelastic strain, ε_I, is calculated using the selected constitutive model and then summed. The matrix stress (σ_m) and fiber stress (σ_f) are increased incrementally for each time step by the relations:

$$\sigma_m = \sigma_m + E_m^*(dt^*\text{strain rate} - \varepsilon_I) \quad (4.3)$$

and

$$\sigma_f = \sigma_f + E_f^*(dt^*\text{strain rate}) \quad (4.4)$$

The stress in the laminate is determined by a rule of mixtures combination of fiber and matrix stresses:

$$\sigma_c = \sigma_m V_m + \sigma_f V_f \quad (4.5)$$

Next, the incremental changes in drag stress, back stress, and work hardening parameter for the selected model are computed. This process is repeated (back to {A} on the diagram) until the desired total strain is reached.

4.5.2 Constant Strain Rate Tests Using 90° Unidirectional Specimens

The algorithm used for predicting the CSR response of 90° unidirectional laminated specimens is shown in Figure 4.2. The initial several steps are identical to the algorithm described above in section 4.5.1 for the CSR response of neat or 0° unidirectional laminate specimens. The transverse elastic modulus (E_2) is calculated using Eq 4.2 prior to time step iteration.

Once the initial steps are completed, time is increased incrementally as before. For each time increment, matrix incremental inelastic strain is calculated using the selected constitutive model and then summed. The incremental changes in drag stress, back stress, and work hardening parameter for the selected model are then computed. The matrix stress (σ_m) and fiber stress (σ_f) are assumed to be equal to the laminate stress which is determined by the relation:

$$\sigma_c = \sigma_c + E_2^*(dt^*\text{strain rate} - V_m\varepsilon_I) \quad (4.6)$$

This process is repeated (back to {A} on the diagram) until the desired total strain is reached.

4.5.3 Creep Tests Using Neat or 0° Unidirectional Specimens

A flow diagram depicting the algorithm used for predicting the creep response of neat or 0° unidirectional laminated specimens is shown in Figure 4.3. When simulating a test with a neat specimen, the volume fraction of fibers is set equal to zero. The initial several steps are identical to the algorithms described in sections 4.5.1 and 4.5.2 for the CSR response of 0° and 90° unidirectional laminate specimens. In the case of the creep test simulations, however, the algorithm requires that the creep stress be specified instead of the strain rate. For the case of 0° fibered laminate creep, the composite strain is assumed to equal the fiber and matrix strain.

During computer simulation of creep tests using the Miller model, it was found that computational problems arise when the creep stress is applied instantaneously. In order to overcome these numerical problems in the simulations and to more closely model the way the creep stress is applied in real tests, a "ramp" loading approach is used in the simulations. That is, the constant strain rate algorithm (described in section 4.5.1) is used until the stress in the specimen reaches 99% of the desired creep stress value. At that point, the program switches over to the creep test algorithm (shown in Figure 4.3).

The above steps are completed before iterating with respect to time. Time is then increased by an increment dt (typically from .01 to .0005 seconds, depending on the numerical stability of the model). For each time increment, matrix incremental inelastic strain, ε_I, is calculated using the selected constitutive model. Next, the matrix inelastic strain is summed and the incremental changes in drag stress, back stress, and work hardening parameter for the model are computed. Finally, updated values of σ_m, σ_f, and ε_c are determined. This process is repeated (back to {A} on the diagram) until the desired time is reached.

4.5.4 Creep Tests Using 90° Unidirectional Specimens

The algorithm used for predicting the creep response of 90° unidirectional laminated specimens is shown in Figure 4.4. The initial several steps are identical to the algorithm described above in section 4.5.3 for the creep response of neat or 0° unidirectional laminate specimens. In the case of 90° fibered laminate creep, however, the initial composite elastic strain (ε_c) is a rule of mixtures combination of fiber and matrix strains:

$$\varepsilon_c = \sigma^*(V_f/E_f + V_m/E_m) \qquad (4.7)$$

The creep stress is applied using a constant strain rate approach as previously described in section 4.5.3. Then, time is increased incrementally, and for each time increment, matrix incremental inelastic strain, ε_I, is calculated using the selected constitutive model. The matrix inelastic strain is summed and a portion of the incremental matrix inelastic strain is added to the total laminate strain according to the relation:

$$\varepsilon_{total} = \varepsilon_{total} + V_m{}^* \varepsilon_I \qquad (4.8)$$

Next, the incremental changes in drag stress, back stress, and work hardening parameter for the selected model are computed. This process is repeated (back to {A} on the diagram) until the desired time is reached.

TABLE 4.1 Tests Conducted At Univ Of Washington

Test		Nominal	Temp	Type
U1	SSC	34.5	482	NEAT
U2	SSC	34.5	482	NEAT
U4	SSC	34.5	566	NEAT
U5	SSC	34.5	649	NEAT
U6	SSC	34.5	649	NEAT
U7	SSC	69	482	NEAT
U8	SSC	69	482	NEAT
U9	SSC	69	566	NEAT
U10	SSC	69	566	NEAT
U11	SSC	69	649	NEAT
U12	SSC	69	649	NEAT
U13	SSC	103.4	482	NEAT
U14	SSC	103.4	482	NEAT
U15	SSC	103.4	538	NEAT
U16	SSC	103.4	566	NEAT
U17	SSC	103.4	649	NEAT
U18	SSC	103.4	649	NEAT
U19	SSC	138	482	NEAT
U20	SSC	138	482	NEAT
U21	SSC	138	566	NEAT
U22	SSC	138	566	NEAT
U23	SSC	138	649	NEAT
U24	SSC	138	649	NEAT
U26	SSC	172.4	482	NEAT
U27	SSC	172.4	566	NEAT
U28	SSC	172.4	566	NEAT
U29	SSC	172.4	649	NEAT
U30	SSC	172.4	649	NEAT
U31	MSC	48.3/96.6	482	NEAT
U32	MSC	48.3/96.6	482	NEAT
U33	MSC	48.3/96.6	566	NEAT
U34	MSC	48.3/96.6	566	NEAT
U35	MSC	48.3/96.6	649	NEAT
U36	MSC	48.3/96.6	649	NEAT
U38	MSC	*Various	566	0
U41	MSC	48.3/96.6	566	90

*Test U38 had creep stresses of 48.3, 96.5, 167, and 262 MPa.

Table 4.2 Tests Conducted At LARC

TEST #	TYPE	STRAIN RATE(1/s)	TEMP °C	TYPE SPECIMEN
L1	CSR	1X10-4	482	NEAT
L2	CSR	1X10-4	566	NEAT
L3	CSR	1X10-4	649	NEAT
L4	CSR	5X10-4	482	NEAT
L5	CSR	5X10-4	566	NEAT
L6	CSR	5X10-4	649	NEAT
L7	CSR	1X10-3	482	NEAT
L8	CSR	1X10-3	566	NEAT
L9	CSR	1X10-3	649	NEAT
L10	CSR	5X10-3	482	NEAT
L11	CSR	5X10-3	566	NEAT
L12	CSR	5X10-3	649	NEAT
L13	CSR	1X10-2	482	NEAT
L14	CSR	1X10-2	566	NEAT
L15	CSR	1X10-2	649	NEAT
L16	CCSR	1X10-4	482	NEAT
L17	CCSR	1X10-4	566	NEAT
L18	CCSR	1X10-4	649	NEAT
L19	CCSR	5X10-4	482	NEAT
L20	CCSR	5X10-4	566	NEAT
L21	CCSR	5X10-4	649	NEAT
L22	CCSR	1X10-3	482	NEAT
L23	CCSR	1X10-3	566	NEAT
L24	CCSR	1X10-3	649	NEAT
L25	CCSR	5X10-3	482	NEAT
L26	CCSR	5X10-3	566	NEAT
L27	CCSR	5X10-3	649	NEAT
L28	CCSR	1X10-2	482	NEAT
L29	CCSR	1X10-2	566	NEAT
L30	CCSR	1X10-2	649	NEAT
L33	CCSR	1X10-4	649	0
L34	CCSR	1X10-4	482	90
L35	CCSR	1X10-4	566	90
L36	CCSR	1X10-4	649	90

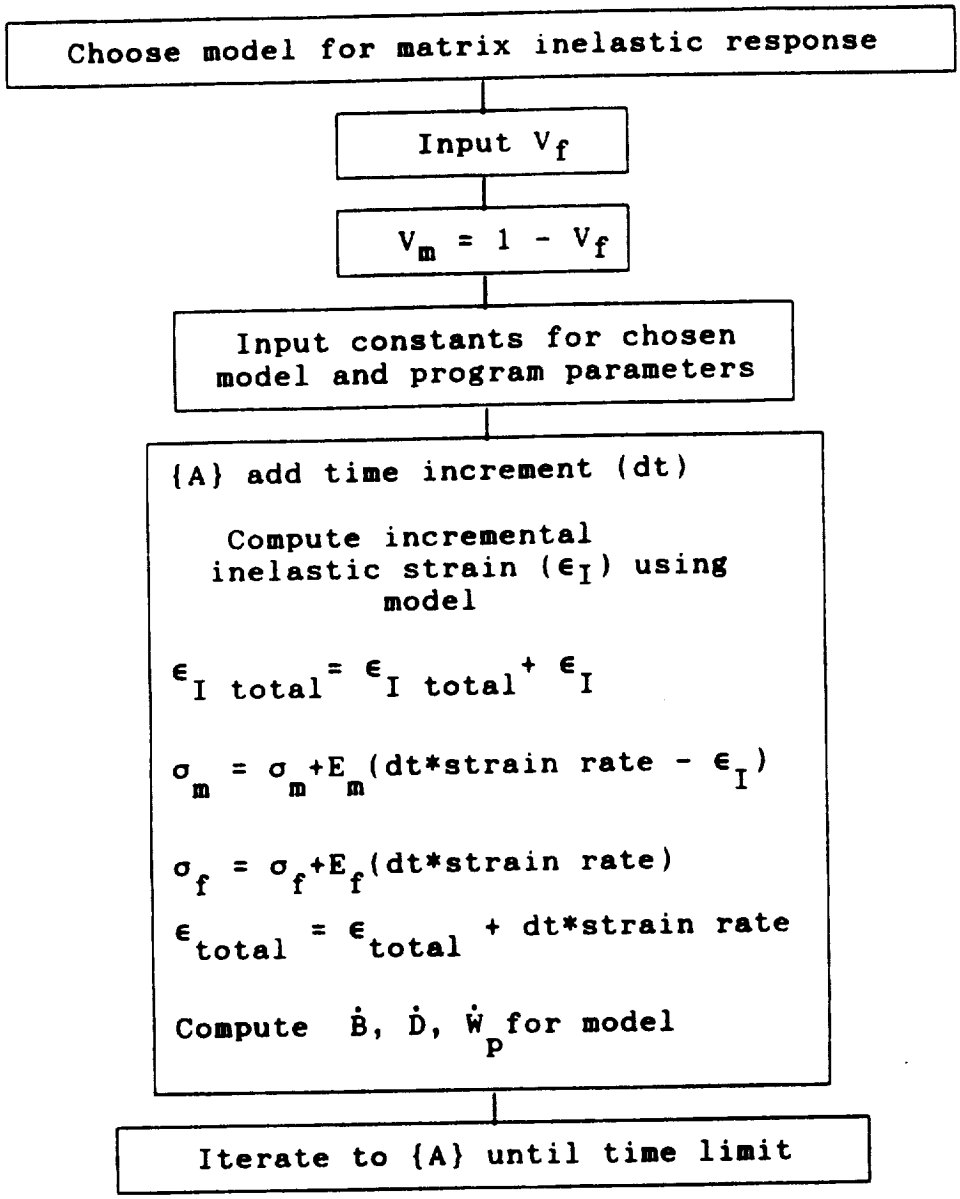

Figure 4.1 Constant strain rate test algorithm for neat or 0° unidirectional specimens.

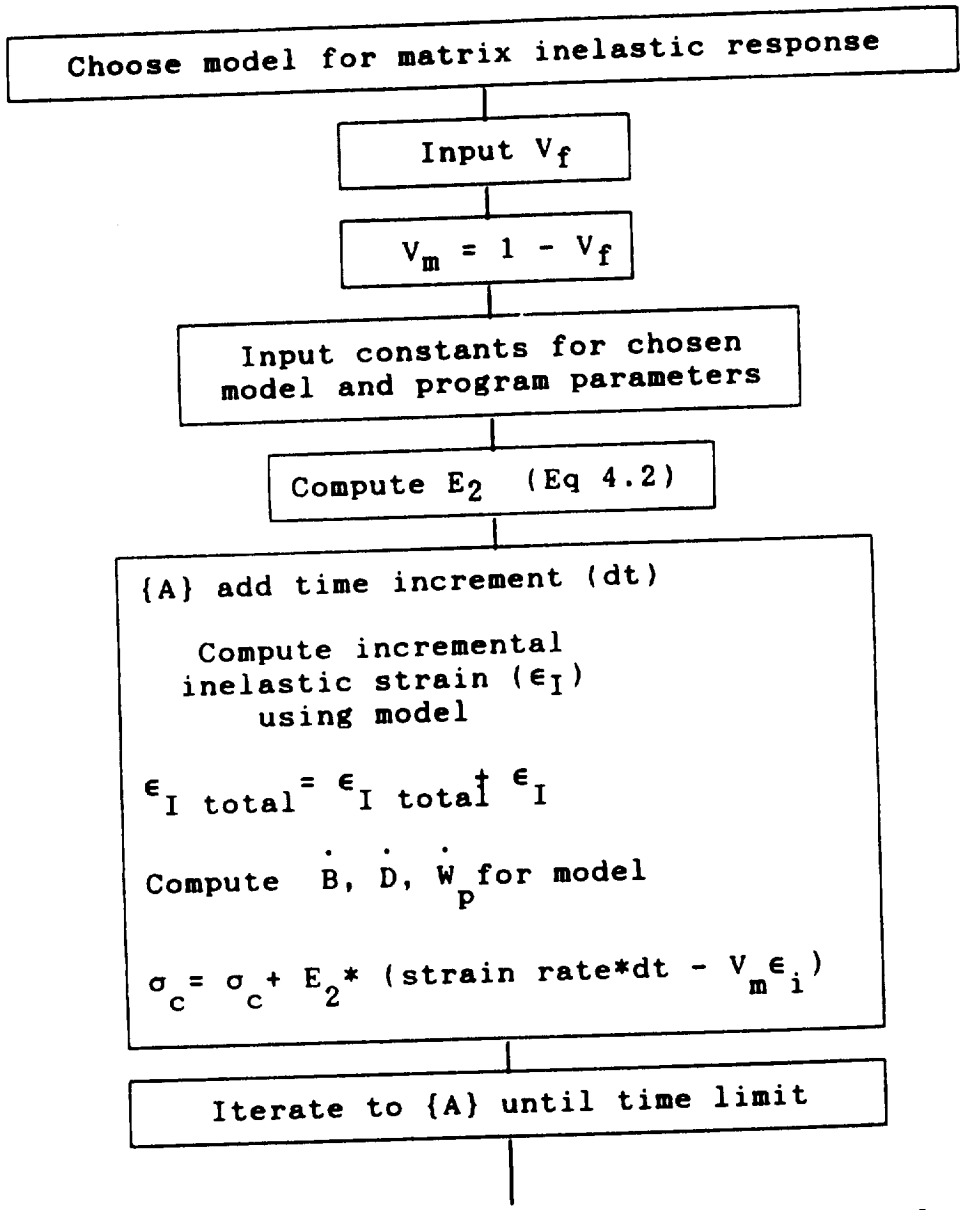

Figure 4.2 Constant strain rate test algorithm for 90° unidirectional specimens.

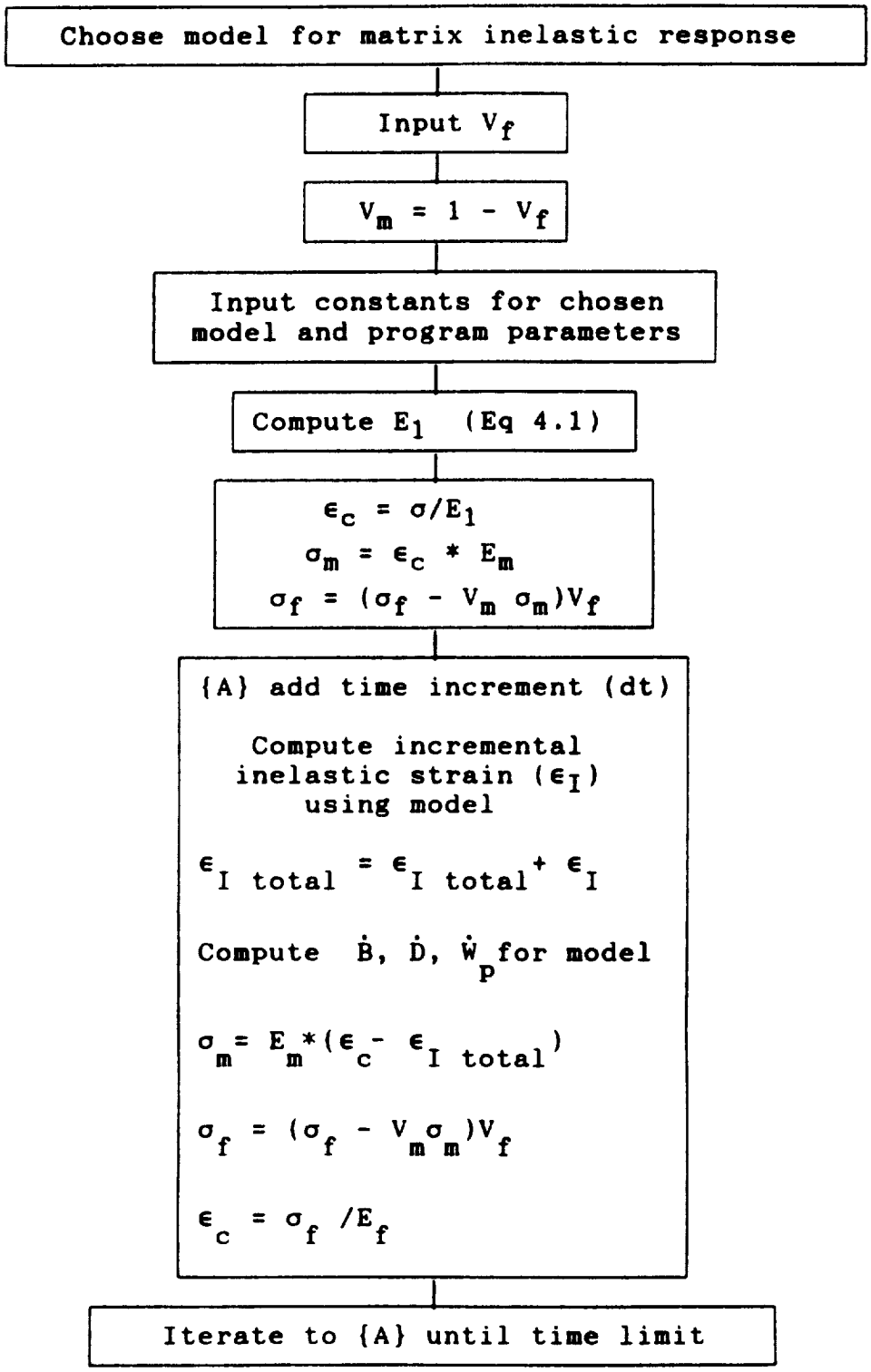

Figure 4.3 Creep test algorithm for neat or 0° unidirectional specimens.

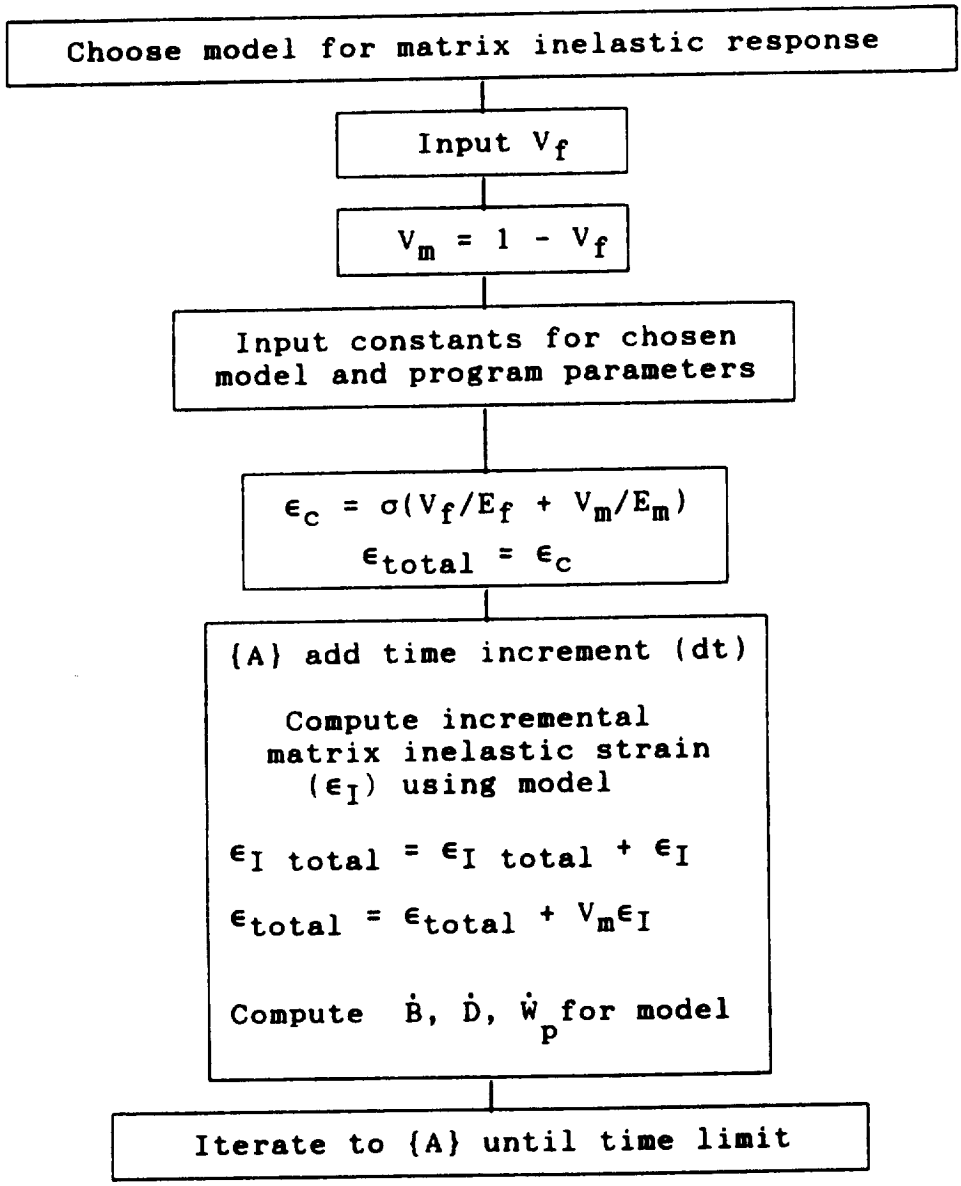

Figure 4.4 Creep test algorithm for 90° unidirectional specimens.

CHAPTER 5 EXPERIMENTAL RESULTS

Much of the data collected during this study has been described in an earlier report, which was released in 1991 [45]. In particular, all measurements obtained using neat (or fiberless) specimens have been described in Ref 45. This earlier report contains roughly seventy plots of data which were collected during the course of this study. A limited number of tests were performed using fiber-reinforced specimens. The data collected during these tests were not presented in the earlier report and are included herein in Appendix A. A brief discussion of the main features associated with each type of test will be presented in this Chapter.

5.1 Neat Specimen Results

Since all of the data collected using neat specimens have been reported elsewhere[45], in the interests of brevity the original data plots for neat specimens will not be repeated in this report. Comparisons between theory and measurements for selected tests will be presented in Chapter 6.

5.1.1 Creep Tests

Data measured during the Creep tests using neat specimens are plotted in Appendix A, Reference 45. As described in Chapter 4 of the present report, creep tests were conducted at three different temperatures (482°C, 566°C, and 649°C) and five different stress levels ranging from 34.5 MPa to 172.4 MPa. The creep rate of the neat Ti-15-3 specimens increased with increasing creep stress and increasing temperature, as would be expected. A very rapid increase in creep rate occurred above 566°C and/or 103.4 MPa. The creep compliance curves imply that Ti-15-3 is linearly viscoplastic at temperatures at or below 482°C and nonlinear viscoplastic at the two higher temperatures.

5.1.2 Constant Strain Rate Tests

Data measured during the Constant Strain Rate Tests using neat specimens are plotted in Appendix B, Reference 45. During the constant strain rate tests, stress was

controlled so as to produce a predetermined strain rate. Five different strain rates were imposed, ranging from a low of .0001/s to a high of .01/sec. Once again, the three test temperatures of 482°C, 566°C, and 649°C were utilized in conjunction with each of the five strain rates.

Interestingly, Ti-15-3 exhibited strain softening at high strain levels during all CSR tests; at strain levels beyond yielding, the slope of the stress-strain curve became negative. Also, in many of the CSR tests (as well as several of the CCSR tests) Ti-15-3 exhibited an upper/lower yield point phenomenen.

The initial modulus of Ti-15-3 was relatively insensitive to strain rate but generally decreased with increasing temperature. The modulus decreased from a reported value of 104.8 GPa at room temperature [26] to 70.7 GPa at 649°C, a drop of approximately 33 percent. The yield stress and tensile stength were found to be highly sensitive to both temperature and strain rate.

5.1.3 Cyclic Constant Strain Rate Tests

Data measured during the Cyclic Constant Strain Rate Tests using neat specimens are plotted in Appendix C, Reference 45. During the cyclic constant strain rate tests, stress was controlled so as to produce a predetermined strain rate until a limiting total strain was reached (usually ± 0.01) at which time the loading was reversed. Five different strain rates were imposed, ranging from a low of .0001/s to a high of .01/sec. Once again, the three test temperatures of 482°C, 566°C, and 649°C were utilized in conjunction with each of the five strain rates.

As discussed in [45], the CCSR tests were extremely difficult to accomplish. Many of the tests had to be repeated; one was attempted five times before even marginal results could be attained. Additionally, during the tests in which an inductance furnace was used to heat the specimens the data recorded by the Nicolet XF-44 was severely contaminated by electronic noise. Although the source of the noise has not been clearly established, it is almost certainly linked to the induction furnace. Where possible the data obtained during these tests were smoothed using a

commercially available software package called Vupoint [46]. Smoothing was accomplished by fitting the data, segment by segment, with polynomials of order 2 through 8. The data collected during tests in which a quartz lamp was used to heatthe specimens resulted in a much "quieter" electronic environment in which to record the CCSR data; this data did not require smoothing.

5.2 Fibered Specimen Results

The data collected using fiber-reinforced specimens is presented in Appendix A of this report. A brief description of each type of test conducted is given below.

5.2.1 Creep Tests

Two creep tests were completed using laminated specimens. Creep strains measured for a 90° laminate at 566°C and 48.3 MPa are shown in Figure A.1, and the creep response of a 0° laminate at 566°C and various incrementally increasing loads is shown in Figure A.2. Because of the high stiffness of the 0° specimen, the deformations experienced at low loads were too small for the extensometer and LVDT to accurately measure. As a result, during subsequent comparisons with theory a correction was made to the data by adding the expected elastic strains to the original data. The resulting values are plotted in Figure B.69 for a creep stress level of 262 MPa.

5.2.2 Constant Strain Rate Tests

Four constant strain rate tests were completed using laminated specimens. The results of L33, shown in Figure A.3, are for a 0° laminate at 649°C and a strain rate of .0001 m/m/sec. Figures A.4 through A.6 show the CSR response of 90° laminates at 482, 566, and 649°C from tests L34 through L36, respectively. The stresses induced by the enforced strain histroy are much lower than expected--even lower than the corresponding stresses measured using neat specimens. The probable explanation for this discrepancy is that the fiber-matrix interface was extremely weak, reducing the stiffness of the laminates in the transverse direction.

CHAPTER 6 APPLICATION OF THE CONSTITUTIVE MODELS

6.1 Measured Model Parameters for Ti-15-3

6.1.1 The Bodner-Partom Model

As described in Chapter 3, the Bodner-Partom theory assumes that the inelastic component of deformation rate is a function of inelastic strain, ε_I, and drag stress, D. Strain hardening is related to plastic work. There is no back stress parameter in the form of the model used in this study, so it has been useful for metals where the back stress saturates to a constant value.

The method used to determine the Bodner-Partom parameters was presented in detail in Chapter 3. The method requires data from constant strain rate (CSR) tests at several strain rates and from creep tests at several stress levels. Since the Bodner-Partom parameters are temperature dependent, the approach used in modelling Ti-15-3 was to find one set of parameters for each temperature to fit all five strain rates. This approach met with moderate success. It was determined that (for Ti-15-3, at least) the parameters are also somewhat strain-rate dependent. That is, the parameters that fit the data from the CSR tests having the four fastest strain rates (5×10^{-4}, 10^{-3}, 5×10^{-3}, and 10^{-2}/sec) had to be adjusted to fit the data from the CSR test with the slowest strain rate (10^{-4}/sec).

Contributing to this difficulty is the fact that Ti-15-3 exhibits an upper-lower yield point phenomenon and strain softening. These characteristics greatly complicate the Bodner-Partom parameter analysis. Because the theory was under consideration for implementation into a "rule of mixtures" analysis for a composite laminate, the decision was made to use the parameters that best fit the data up to approximately 0.8% strain.

Table 6.1 contains the values obtained for the Bodner-Partom parameters at the three test temperatures and five strain rates considered. Those values marked by an

asterisk were found to be particularily strain rate dependent; the values listed are the recommended "best" value for Ti-15-3 at the strain rates considered in this study.

6.1.2 Miller Model

Miller's constitutive model, as described in Chapters 3 and 4, requires creep, constant strain rate, and cyclic constant strain rate tests, including CCSR tests in which the strain limits are increased in increments. As expected, the Miller parameters for Ti-15-3 are highly temperature dependent. The material behavior is substantially affected by strain rate. At 900°F, Ti-15-3 shows an inverse strain rate sensitivity. Unlike most materials, there is more inelastic deformation at the stress and strain extremes at the fastest strain rate than there is at the slowest. At the two higher temperatures, the trend was reversed: there is more inelastic deformation at the stress and strain extremes at the slowest strain rates than there is at the fastest. A difficulty arises, however, because the asymptotic stress for each of the two highest temperatures at the fastest strain rate was double the stress at the slowest strain rate. This feature could not be accounted for using the original version of the Miller model, and hence the modifications described in Chapter 3 were implemented.

Table 6.2 contains values for Ti-15-3 Miller parameters at the three test temperatures considered. All of the parameters were found to be rate insensitive, except for the parameter H_4 at 482°C. The value listedfor H_4 is the recommended "best" value for Ti-15-3 at the strain rates considered in this study.

6.1.3 Walker Model

The method used to determine the Walker parameters was described in detail in Chapter 3. The method requires data from cyclic constant strain rate (CCSR) tests at several strain rates and from stress drop or relaxation tests at several strains. As

expected, the Walker parameters for Ti-15-3 are highly temperature dependent. At 566°C and 649°C the parameters were found to be essentially independent of strain rate, but at 482°C the parameters were somewhat strain rate dependent.

As with the Bodner-Partom and Miller models, initial values for the Walker parameters were obtained using methods described above. Once the initial values were obtained, adjustments were made to the parameters to improve agreement between the experimental and predicted results. The Walker model values took less time to adjust than did the parameters for the other two models. Table 6.3 contains values for Ti-15-3 Walker parameters at the three test temperatures considered. The parameters were found to be strain-rate independent, except as noted by an asterisk.

6.2 Algorithms Used To Generate CCSR, CSR, and Creep Curves

6.2.1 Bodner-Partom Model

The algorithm used to generate a prediction of the CCSR response of Ti-15-3 based on the Bodner-Partom model is shown in Figure 6.1. First, the Bodner-Partom model parameters are input along with certain program parameters, including strain rate, time step, and strain limit. Strain is then increased by an amount equal to the strain rate times the time increment (dt). Assuming that the initial response is elastic, the resulting stress is computed from Eq 3.1.

The iterative portion of the algorithm begins at the line designated by {A}. For each new time increment (dt), the time rate of change of inelastic strain, plastic work, and drag stress are calculated. Also computed are the total inelastic strain, drag stress, total strain, and stress. This iterative process is continued until either the strain limit or the time limit is reached. Each time the strain limit is reached, the strain rate is reversed. When the time limit is reached, the program is ended.

The algorithms for generating CSR and creep curves with the Bodner-Partom model are identical to the CCSR algorithm with the following exceptions. For CSR curves, the strain rate is not reversed when the strain limit is reached. Instead, the program is ended. For creep tests, the CCSR approach is used until the stress is within one percent of the predetermined creep stress. At this point, the stress is held constant, and the iterative process starting at {A} in Figure 6.1 is continued. In the case of creep, however, the total strain increases for each time step by the incremental inelastic strain only; i.e., because the stress is constant, the elastic strain does not change as it does in the case of CSR or CCSR tests.

6.2.2 Miller Model

The algorithm used to generate a prediction of the CCSR response of Ti-15-3 based on the Miller model is shown in Figure 6.2. The process is identical to the one described for the Bodner-Partom model in section 6.2.1 with a few minor differences. First, the time rate of change of both back stress and drag stress are calculated for the Miller model. Second, new values for both back stress and drag stress are calculated at each time increment. Recall that the back stress was assumed constant in the Bodner-Partom model. Similarly, the algorithms for generating CSR and creep curves with the Miller model differ from the corresponding Bodner-Partom algorithms only in the requirement to calculate an incrementally changing back stress.

6.2.3 Walker Model

The algorithm used to generate a prediction of the CCSR response of Ti-15-3 is shown in Figure 6.3. The process is identical to the one described in section 6.2.1 for the Bodner-Partom model with a few minor differences. First, the drag stress is assumed constant with the Walker model, so the time rate of change of back stress and a new value for back stress are calculated at each time increment. Recall that the back stress was assumed constant in the Bodner-Partom model. Similarly, the

algorithms for generating CSR and creep curves with the Walker model differ from the corresponding Bodner-Partom algorithms only in the requirement to calculate an incrementally changing back stress.

6.3 Computer Simulation of Neat Specimen Response

6.3.1 Neat Specimen CSR Results

Figures B.1 through B.15 (Appendix B) compare the predictions obtained using the Bodner-Partom model with experimental measurement for the neat specimen CSR response. (The predicted CSR response using the Miller and Walker models can be seen by examining the CCSR results.) The Bodner-Partom model gave fairly accurate CSR predictions at all temperatures and strain rates with one noted exception: the model did not accurately predict the material's upper/lower yield point phenomenon exhibited under some conditions.

6.3.2 Neat Specimen CCSR Results

6.3.2.1 Bodner-Partom Model

As previously mentioned, the version of the Bodner-Partom model used in this work does not have back stress as an ISV. Hence, the ability of the model to simulate cyclic loading for a material exhibiting a changing back stress is uncertain. Furthermore, since only CSR and creep tests are required to determine the Bodner-Partom constants, the data obtained from the experimental CCSR tests are not used. Therefore, it is of interest to assess the CCSR predictive capabilities of the Bodner-Partom model with regard to Ti-15-3.

Figures B.16 through B.30 (Appendix B) compare the Bodner-Partom model's prediction of neat specimen CCSR response to the experimental data attained during

testing at NASA LaRC. The Bodner-Partom model generally did an adequate job in simulating the CCSR response of Ti-15-3 at the three test temperatures. The best agreement to experimental data seemed to be at the fastest strain rate (.01/sec) and at the highest temperature (649°C). The Bodner-Partom model worked well when the material behaved in a nearly elastic-perfectly plastic manner.

The largest differences between experiment and prediction came in the tests where the material exhibited an upper/lower yield point (e.g. Figure B.18). As mentioned previously, none of the models simulate this phenomenon. The ultimate goal of this study was to apply the three models considered to a unidirectional composite with ceramic fibers. Ceramic fibers generally fail at low values of strain (<1%). Therefore, when determining the Bodner-Partom parameters, the decision was made to take into account the higher value of stress associated with the upper yield point. As a result, the predicted CCSR stresses at the strain extremes tended to be greater than the experimental stresses. An alternative approach would be to fit the data to the lower stresses occurring at greater strains (beyond the upper yield point).

6.3.2.2 Miller Model

Figures B.31 through B.45 compare the Miller model's prediction of neat specimen CCSR response to the experimental data attained during testing at NASA LaRC. After the modifications described in section 3.4.2 were made, the Miller model generally did a good job in simulating the CCSR response of Ti-15-3 at the three test temperatures. The best agreement to experimental data seemed to be at 482°C. At the two higher test temperatures, where the material behaved in a nearly elastic-perfectly plastic manner, the model was less accurate. This is not unexpected because, as mentioned in Chapter 3, the model was developed for and performs best with strongly workhardening materials.

6.3.2.3 Walker Model

Figures B.46 through B.60 compare the Walker model's prediction of neat specimen CCSR response to the experimental data attained during testing at NASA LaRC. The Walker model was less accurate in predicting the CCSR response of Ti-15-3 than the Miller model, but more accurate than the Bodner-Partom model. Predicted stresses were generally within about 10-20% of experimental values at the three test temperatures. Unlike the Miller model, the Walker equations were able to model the elastic-perfectly plastic shape characteristics of the Ti-15-3 hysteresis curve, but difficulty was encountered in accurately matching the stress extremes. The best agreement with experimental data seemed to be at the two higher test temperatures, where the material behaved in a nearly elastic-perfectly plastic manner. The model was less accurate at 482°C.

6.3.3 Neat Specimen Creep Results

Figures B.61 through B.66 compare the creep response predicted by the three models to the experimental results. Comparisons are made at two creep stresses (34.5 and 172 MPa) and the three previously specified test temperatures.

The models have limited accuracy in predicting the creep response of Ti-15-3. In each of the six cases, all of the models predict a linear creep response, representative of steady-state creep. Conversely, the experimental results for Ti-15-3 in all six cases clearly show that a non-linear creep response (sometimes referred to as "phase-one creep" or "primary creep") precedes steady state creep.

If a comparison is made on the basis of the linear region, the Walker model most closely matches the slope of the creep vs time curves in three of the six cases (Figures B.61, 63, and 66), while the Miller model matches most closely in only one (Figure B.65). Note that the Bodner-Partom and Walker predictions coincide on Figure B.61. Also, the Miller model over-predicts the steady-state creep rate in four of the six cases. Finally, although time dependent deformation actually occurred in all six

cases, the Bodner-Partom model predicts only elastic deformation in three of the six cases (Figures B.61, 62, and 63).

6.4 Computer Simulation of Laminate Response

Figures B.67 through B.71 compare experimental results to predictions obtained using the three models for a unidirectional laminate (V_f = .29) subjected to various loading conditions. In Figure B.67, the predicted 566°C creep response of a 0° laminate is shown for a creep stress of 262 MPa. Figure B.68 shows the 566°C predicted creep response of a 90° laminate at a creep stress of 48.3 MPa. Predicted 0° laminate CSR response at 649°C and .0001 m/m/sec is shown in Figure B.69. Figures B.70 through B.72 show predictions of the 90° laminate CSR response at .0001 m/m/sec for each of the three test temperatures (482, 566, and 649°C respectively).

All three models gave very accurate predictions of the 0° CSR results at 649°C. The Bodner-Partom model resulted in the most accuratepredictions for the 0° creep results at 262 MPa. The creep and CSR results for the 90° specimens were inconclusive in all cases due to the unexpected weakness of the laminate in the transverse direction.

Table 6.1 Bodner-Partom Parameters For Ti-15-3

Parameter	482°C	566°C	649°C
n	9.69	.3354	*.212
D_1	89.47E7	17.27E9	28.9E9
m	2.357E-7	2.012E-7	.0001
D_0	72.69E7	16.28E9	2.3E9
r	11.934	*2.931	2.39
a	*.2532	*.031	.2
D_2	12.67E7	3.242E9	3.5E8
E	79.2E9	73.33E9	72.5E9

*a = 1.27 for 482°C, .0001/s. r = 6 and a = .55 for 566°C, .0001/s. n = .206 for 649°C, .0005 and .0001/s.

Table 6.2 Miller Parameters For Ti-15-3

Parameter	482°C	566°C	649°C
E (MPa)	78.0E3	75.6E6	68.5E3
σ_{ys}	533	258	180
ϵ	.0001	.0001	.0001
n	.7882	.9516	3.73
$B_c\theta'$	2.36E-7	2.658E-8	5.65E-4
H_1	1.733E5	9.5E4	8.685E4
a	.00194	.00181	2.7E-4
H_2	.1034	.15	.6893
C_1	.05	.05	.05
C_2	.69	.69	.69
H_3	1.5	5	6
H_4	*var	1	1

*H_4 = .6, .7, .9, 1.1, 1.15 for .0001, .0005, .001, .005, .01/s respectively at 482°C

Table 6.3 Walker Parameters For Ti-15-3

Parameter	482°C	566°C	649°C
E	11.49E6	10.95E6	10.37E6
n	4.282	5.577	7.825
m	0	.9878	9.405
n_2	*29690	1076000	10950000
n_7	0	.2146	3.14E-30
n_9	*.8723	214.3	2028.2
B_{circ}	2038	-1020.5	-258.5
D_0	*770440	154000	69038

* at 482°C, n_2 = 296900 and n_9 = 8.723 for .005/s and .01/s; D_0 = 539300, 462300, 277400, and 308200 for .0005, .001, .005, and .01 respectively.

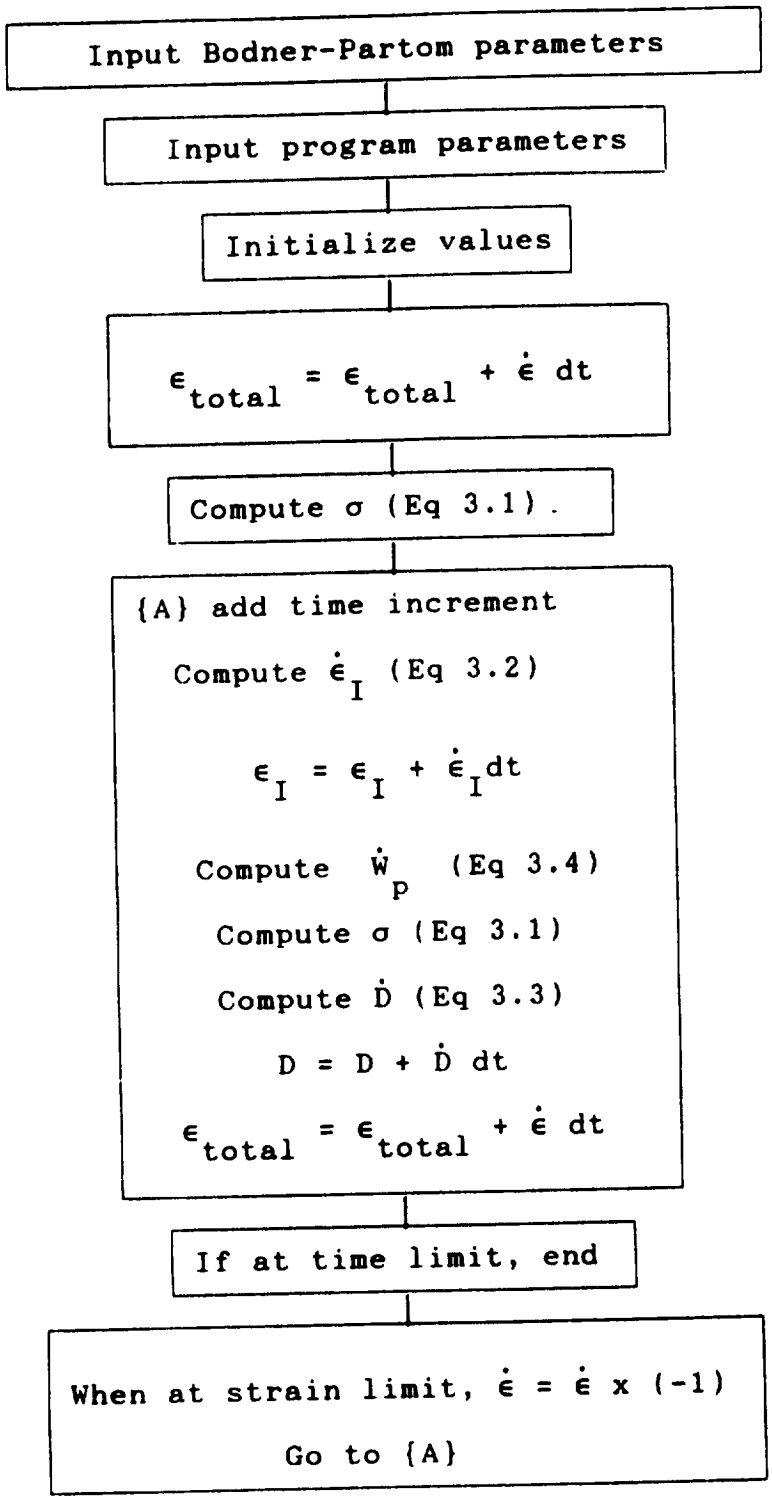

Figure 6.1 Bodner-Partom Model CCSR Algorithm

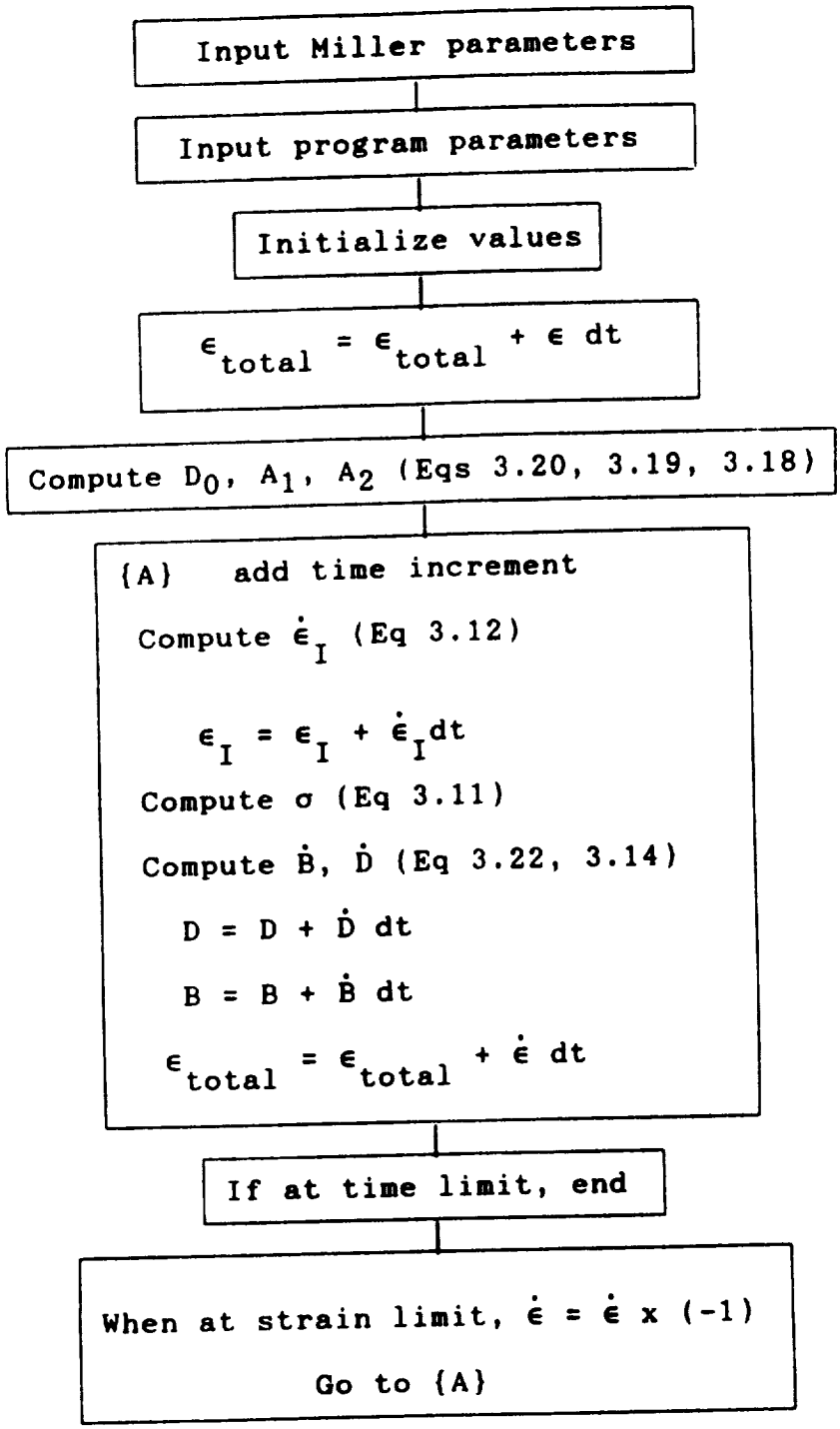

Figure 6.2 Miller Model CCSR Algorithm

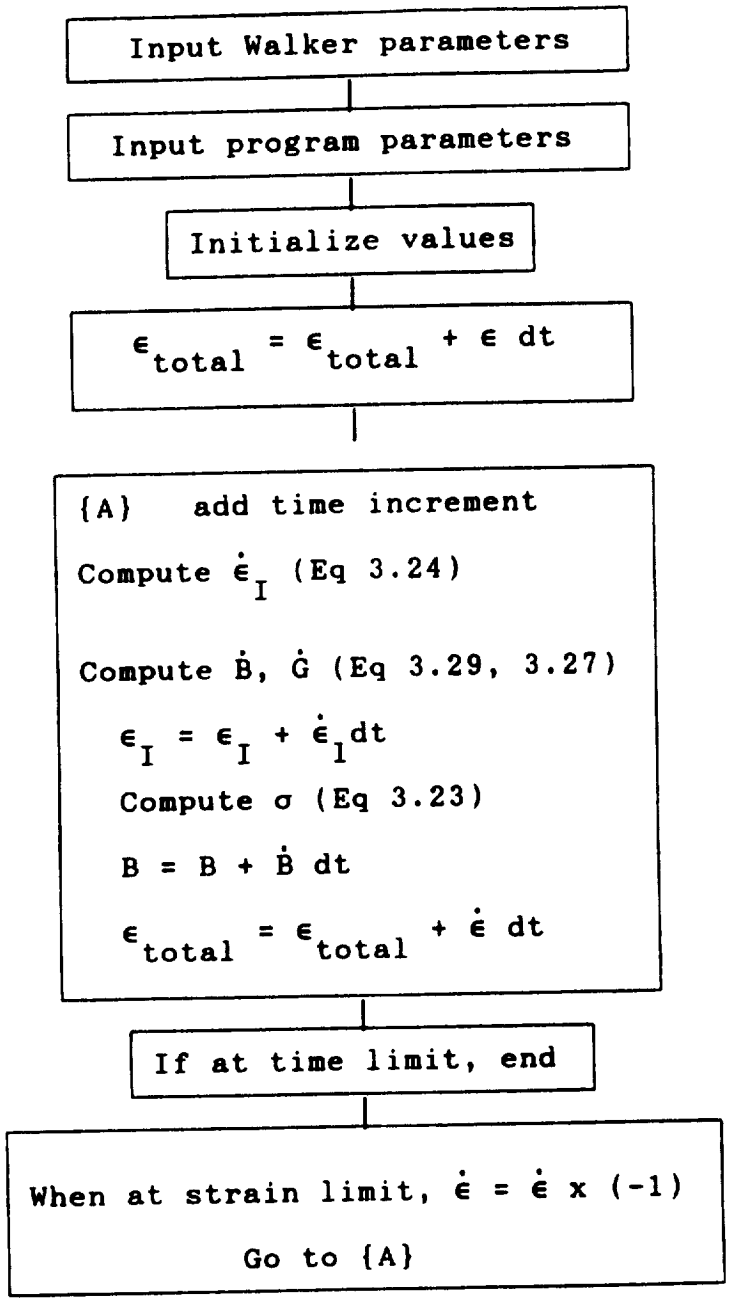

Figure 6.3 Walker Model CCSR Algorithm

CHAPTER 7 CONCLUSIONS AND RECOMMENDATIONS

7.1 General Behavior of Ti-15-3 at Elevated Temperatures

Ti-15-3 exhibits significant inelastic deformation for creep stresses above 34 MPa at temperatures above 482°C. The initial modulus is dependent on temperature, decreasing by about 33% as temperature is increased from 20°C to 649°C. The 0.2% yield stress and ultimate tensile strength are both strain rate and temperature dependent. Strengths decrease with increasing temperature and decreasing strain rate. Under constant strain rate or cyclic constant strain rate conditions at elevated temperatures, Ti-15-3 exhibits an upper yield strength effect and strain softening at all temperatures tested. In the fibered laminate tests, the upper yield point phenomenon was observed in only the 649°C 90° CSR test (Figure B.72).

7.2 General Assessment of the Viscoplastic Models Considered

The mechanical response of Ti-15-3 to various loading conditions at elevated temperatures can be reasonably modeled by all three thermoviscoplastic constitutive theories considered, although obtaining the required material parameters required extensive efforts. In all cases the analysis was complicated by the upper yield point and strain softening phenomenon exhibited by Ti-15-3, which none of the models considered is capable of predicting.

When combined with the simnple rule of mixtures formulation, all three models produced good predictions for a 0° laminate loaded under constant strain rate conditions as well as under constant load (creep) conditions. However, evaluation of the models for 90° specimens was inconclusive, since even the measured viscoplastic response of the 90° specimens was much higher than expected; the viscoplastic response measured for the 90° specimens was more pronounced than that measured for the neat (fiberless) specimens. It is believed that the very high

viscoplastic response of the 90° specimens is due to a low strength fiber-matrix interface. The predictions obtained using all three models significantly underestimated the creep strain response and overestimated the constant strain rate stress response for the 90° specimens. These discrepancies will be further discussed in section 7.2.2.1.

7.2.1 Ease of Use

All three models required extensive testing and considerable curve fitting. The parameters for each of the three models were temperature dependent, and in some cases strain-rate dependent.

The Bodner-Partom model was judged easiest to use for two reasons. First, the procedure to determine the parameters is more clearly described in the literature than for the other two models. Second, the version of the Bodner-Partom model used does not require elevated temperature CCSR testing, which is very beneficial from a practical standpoint. On the other hand, the version used does not include back stress as an ISV, which may be a significant limitation, particularly when attempting to model the cyclic loading of a material in which a changing back stress occurs. Since the version used has no provision for changing back stress, it is most appropriate for materials whose back stress quickly saturates to a constant value. Unfortunately, this may not be apparent until testing is completed.

Once the test matrix was completed, the parameters were determined for each model. Although each of the three models required a certain amount of "curve fitting", parameters for the Walker model were easiest to obtain for Ti-15-3. The nearly elastic-perfectly plastic response of Ti-15-3 contributed to the curve fitting difficulties encountered with the Miller model.

7.2.2 Predictive Accuracy

7.2.2.1 Fibered Specimen Constant Strain Rate Tests

Four unidirectional specimens were successfully tested under constant strain rate conditions at NASA Langley. One 0° specimen was tested at 649°C and .0001/s (test L33). As shown in Figure B.69, all three constitutive models predicted the stress-strain response within about 10 percent, with the Miller model being slightly more accurate.

Three 90° specimens were tested (tests L34, 35, and 36) under a strain rate of .0001/s, one at each of the three test temperatures (482, 566, 649°C). The predicted response and experimental results of these tests are shown in Figures B.70 through B.72. In each case, the specimens were initially stiffer than neat specimens tested under identical conditions (as expected). However, as the applied strain increased the corresponding stress level did not increase as expected. Near the extremes of applied strain, the stresses induced were lower than that measured for neat specimens, and only 25-35% of the predicted values for fibered specimens. Similar results were obtained during creep tests using the 90° specimens (described below). Since the initial elastic modulus of the 90° specimens was fairly well-predicted using the rule of mixtures, and the 0° specimen behaved as predicted, it has been concluded that the pronounced viscoplastic response of the 90° specimens was due to a very compliant and/or weak fiber/matrix interface. This argument is substantiated by the results of Johnson et al [26], who report that the fiber-matrix interface in this MMC is very weak at room temperature.

7.2.2.2 Fibered Specimen Creep Tests

One 0° (test U38) and one 90° (test U41) specimen were creep tested at 566°C. The 90° specimen experienced a much higher inelastic strain rate than expected, probably due to a weak fiber-matrix interface. As a result, inelastic strains were two to four times as high as predicted. Figure B.68 shows the experimental results and the

predicted response from each of the three models. As shown in Figure B.67, the 0° test and theory agreed much more closely than did the 90° test and theory. The Bodner-Partom model agreed most closely with experimental results, followed by the Miller and Walker models. All three overpredicted the inelastic deformation.

7.3 Recommendations

The following recommendations are submitted as a result of this study:

1. The use of an induction furnace during the CSR and CCSR testing resulted in electronic noise contamination of the data and should be avoided in future testing. Quartz lamp heaters used in some of the CCSR tests provided a far superior electronic environment for high temperature testing, and is recommended.

2. Cyclic constant strain rate testing is very difficult to perform. Two of the models investigated during this study (the Miller or Walker models) require CCSR test results to determine model paramters. It is recommended that alternate means of determining these parameters from experimental data, which avoid the use of CCSR testing, be developed.

3. For materials in which back stress is constant, or nearly constant, then the Bodner Partom model in its presently used form provides accurate and easily obtainable results. Otherwise, the Miller and Walker models are best. From a purely practical standpoint, the parameters for the Walker model were easier to obtain during this study than those for the Miller model. Therefore, the Walker model would be recommended for use in modeling a material which demonstrates a pronounced Baushinger effect.

4. The strength of the fiber/matrix interface in the Ti-15-3/SCS_6 MMC considered in this study must be improved. Once this is accomplished, additional creep and CSR tests, with both 0° and 90° laminates, should be performed.

REFERENCES

1. Allen, D.H. & Beek, J.M., "On the Use of Internal State Variables in Thermoviscoplastic Constitutive Equations," Mechanics and Materials Center, Texas A&M University, College Station, TX, #MM NAG3-491-84-12, May 1984.

2. Anand, L. "Constitutive Equations for the Rate Dependent Deformation of Metals at Elevated Temperatures," ASME JRNL ENG MATLS AND TECH, Vol. 104, January 1982, pp. 12-17.

3. Ankem, S., & Seagle, S.R., "Heat Treatment of Beta Titanium Alloys," in Beta Titanium Alloys in the 1980's, Edited by R.R. Boyer & H.W. Rosenberg, AIME 1983, pp.107-128.

4. Bania, P.J., Lenning, G.A., & Hall, J.A., "Development and Properties of Ti-15V-3Cr-3Sn-3Al (Ti-15-3)," in Beta Titanium Alloys in the 1980's, Edited by R.R. Boyer & H.W. Rosenberg, AIME 1983, pp.209-230.

5. Beaman, Rebecca L., "The Determination of the Bodner Material Coefficients for IN 718 and Their Effects on Cyclic Loading," M.S. Thesis, AFIT, WPAFB, OH, AFIT/GAE/AA/84M-1, March 1984.

6. Beek, J.M., Allen, D.H., & Milly, T.M., "A Qualitative Comparison of Current Models For Nonlinear Rate-Dependent Materials Behaviour of Crystalline Solids," Mechanics and Materials Center, Texas A&M University, College Station, TX, #MM 4246T-83-14, Nov 1983.

7. Bodner, S.R., and Partom, Y., "Constitutive Equations for Elastic-Viscoplastic Strain-Hardening Materials," JRNL APPL MECH, Vol 42, pp. 385-389 (1975).

8. Bodner, S.R., Partom, I., and Partom, Y., "Uniaxial Cyclic Loading of Elastic-Viscoplastic Materials," JRNL APPL MECH, Vol 46, pp. 805-810 (1979).

9. Bodner, S.R., "Representation of Time Dependent Mechanical Behavior of Rene 95 by Constitutive Equations," Tech Report AFML-TR-79-4116, Aug 1979.

10. Boyer, Rodney R., "Titanium and Titanium Alloys," ASM METALS HANDBOOK, 1988, pp. 458-475.

11. Chan, K.S., Bodner, S.R., & Linholm, U.S., "Phenomenological Modeling of Hardening and Thermal Recovery in Metals," JRNL ENG MATLS AND TECH, Vol. 110, January 1988, pp. 1-8.

12. "Continuous Silicon Carbide Metal Matrix Composites," Product Information Brochure, Textron Specialty Materials, Textron, Inc., Lowell, MA.

13. Costa, J.E., Banerjee, D., & Williams, J.C., "Hydrogen Effects in ß-Titanium Alloys," in Beta Titanium Alloys in the 1980's, Edited by R.R. Boyer & H.W. Rosenberg, AIME 1983, pp.69-84.

14. Ding, J.L., & Lee, S.R., "Constitutive modeling of the Material Behavior at Elevated Temperatures and Related Material Testing," INTL JRNL PLASTICITY, Vol 4, pp. 146-161, (1988).

15. Duerig, T.W. & Williams, J.C., "Overview: Microstructure and Properties of Beta Titanium Alloys," in Beta Titanium Alloys in the 1980's, Edited by R.R. Boyer & H.W. Rosenberg, AIME 1983, pp.20-68.

16. Dvorak, G.J., & Bahei-El-Din, Y.A., "A Bimodal Plasticity Theory of Fibrous Composite Materials," ACTA MECHANICA, Vol 69, pp. 219-241 (1987).

17. Eisenberg, M.A., & Yen, C.-F., "A Theory of Multiaxial Anisotropic Viscoplasticity," JRNL APPL MECH, Vol 48, pp. 276-284 (1981).

18. Eisenberg, M.A., & Yen, C.-F., "Application of a Theory of Viscoplasticity to Uniaxial Cyclic Loading," JRNL ENG MATLS AND TECH, Vol. 105, pp. 106-112 (1983).

19. Flugge, W., Viscoelasticity, Blaisdell Publishing Co., Waltham, MA., 1967.

20. Hall, J.A., "Primary Processing of Beta and Near Beta Titanium Alloys," in Beta Titanium Alloys in the 1980's, Edited by R.R. Boyer & H.W. Rosenberg, AIME 1983, pp.129-144.

21. Hartmann, G., & Kollman, F.G., "A Computational Comparison of the Inelastic Constitutive Models of Hart and Miller," ACTA MECHANICA, Vol 69, pp. 139-165 (1987).

22. Hertzberg, Richard W., Deformation and Fracture Mechanics of Engineering Materials, John Wiley & Sons, N.Y., 1976.

23. Hicks, A.G., & Rosenberg, H.W., "Ti-15-3 Foil Properties and Applications," in Beta Titanium Alloys in the 1980's, Edited by R.R. Boyer & H.W. Rosenberg, AIME 1983, pp.231-238.

24. Imbrie, P.K., Haisler, W.E., & Allen, D.H., "Evaluation of the Numerical Stability of Material Parameter Variations for Several Unified Constitutive Models," Aerospace Engineering Department, Texas A&M University, College Station, TX, #MM 4998-85-6, May 1985.

25. Jaske, C.E., Mindlin, H., & Perrin, J.S., "Cyclic Stress-Strain Behavior of Two Alloys at High Temperature," ASTM STP 519, American Society for Testing and Materials, pp. 13-27 (1973).

26. Johnson, W.S., et al, "Mechanical Characterization of SCS6/Ti-15-3 Metal Matrix Composites at Room Temperature," NASP Technical Memorandum 1014, NASA Langley Research Center, Hampton, VA, April 1988.

27. Krempl, E., "Models of Viscoplasticity," ACTA MECHANICA, Vol 69, pp. 25-42 (1987).

28. Leach, A.E., "Formed Ti-15V-3Cr-3Sn-3Al Tankage," in Beta Titanium Alloys in the 1980's, Edited by R.R. Boyer & H.W. Rosenberg, AIME 1983, pp.331-348.

29. Merzer, A., & Bodner, S.R., "Analytical Formulation of a Rate and Temperature Dependent Stree-Strain Relation," ASME JRNL ENG MATLS AND TECH, Vol 101, July 1979, pp. 254-257.

30. Miller, A., "An Inelastic Constitutive Model for Monotonic, Cyclic, and Creep Deformation: Part I - Equations Development and Analytical Procedures," ASME JRNL ENG MATLS AND TECH, April 1976, pp. 97-105.

31. Miller, A., "An Inelastic Constitutive Model for Monotonic, Cyclic, and Creep Deformation: Part II - Application to Type 304 Stainless Steel," ASME JRNL ENG MATLS AND TECH, April 1976, pp. 106-113.

32. Milly, T.M., & Allen, D.H., "A Comparative Study of Nonlinear Rate-Dependent Mechanical Constitutive Theories for Crystalline Solids at Elevated Temperatures," M.S. Thesis, #VPI-E-82-5, VPI, Blacksburg, VA, March 1982.

33. Reed-Hill, Robert E., Physical Metallurgy Principles, Litton Educational Publishing, Inc., Brooks/Cole Engineering Division, Monterey, CA 1973.

34. Rogacki, J. and Tuttle, M., "Experimental Measurement of the Viscoplastic Behavior of SiC/Ti Metal Matrix Composites at Elevated Temperatures," Presented at the 1989 SEM Fall Conference, Nov 6-8, Kansas City, MO.

35. Rogacki, J. and Tuttle, M., "Thermoviscoplastic Behavior of SCS_6/Ti Metal Matrix Composites," Presented at the 1990 SEM Spring Conference, June 6-8, Albequerque, NM.

36. Rosenberg, H.W., "Property Scatter in Beta Titanium: Some Problems and Solutions," in Beta Titanium Alloys in the 1980's, Edited by R.R. Boyer & H.W. Rosenberg, AIME 1983, pp.145-160.

37. Rosenberg, H.W., "Ti-15-3 Property Data," in Beta Titanium Alloys in the 1980's, Edited by R.R. Boyer & H.W. Rosenberg, AIME 1983, pp.409-432.

38. Rosenberg, H.W., "Ti-15-3: A New Cold-Formable Sheet Titanium Alloy," JRNL OF METALS, Vol 35, No. 11, pp 30-34 (1986).

39. Sakaki, T., and Taya, M., "Analysis of Creep of Unidirectional Composite Materials," unpublished notes from seminar, Department of Mechanical Engineering, University of Washington, 15 June 1989.

40. Schwartz, M. M., Composite Materials Handbook, McGraw-Hill Book Co., New York, 1984.

41. Shames, A., Rosenblum, M., & Treple, W.B., "Cold Forming Titanium 15-3 Alloy," in Beta Titanium Alloys in the 1980's, Edited by R.R. Boyer & H.W. Rosenberg, AIME 1983, pp.307-330.

42. Stouffer, D.C., Papernik, L. & Bernstein, H.L., "Prediction of the Mechanical Response of A High Temperature Superally Rene 95," Tech Report #AFWAL-TR-80-4184, September 1980.

43. Stouffer, D.C., & Bodner, S.R., "A Relationship Between Theory and Experiment For a State Variable Constitutive Equation," Tech Report #AFWAL-TR-80-4194, January 1981.

44. Stouffer, D.C., "A Constitutive Representation for IN100," Tech Report #AFWAL-TR-81-4039, June 1981.

45. Tuttle, M. and Rogacki, J., "Thermoviscoplastic Response of Ti-15-3 Under Various Loading Conditions," NASA CR 187621, NASA Langley Research Center, Hampton, VA, Oct 1991

46. "Vu-Point II," Maxell Laboratories, Inc., WS-Cubed Division, La Jolla, CA, 1991.

47. Walker, K.P., "Research and Development Program for Nonlinear Structural Modeling With Advanced Time-Temperature Dependent Constitutive Relationships," NASA Tech Report #CR-165533, NASA Lewis Research Center, Cleveland, OH, 1981.

48. Yen, C.-F., & Eisenberg, M.A., "The Role of a Loading Surface in Viscoplasticity Theory," ACTA MECHANICA, Vol 69, pp. 77-96 (1987).

49. Young, C.M., & Sherby, O.D., "Subgrain Formation and Subgrain Boundary Strengthening in Iron-Based Materials," JRNL IRON & STEEL INST, Sep 1973, pp. 640-647.

APPENDIX A

MEASURED VISCOPLASTIC RESPONSE OF UNIDIRECTIONAL SCS_6/Ti-15-3 MMC'S

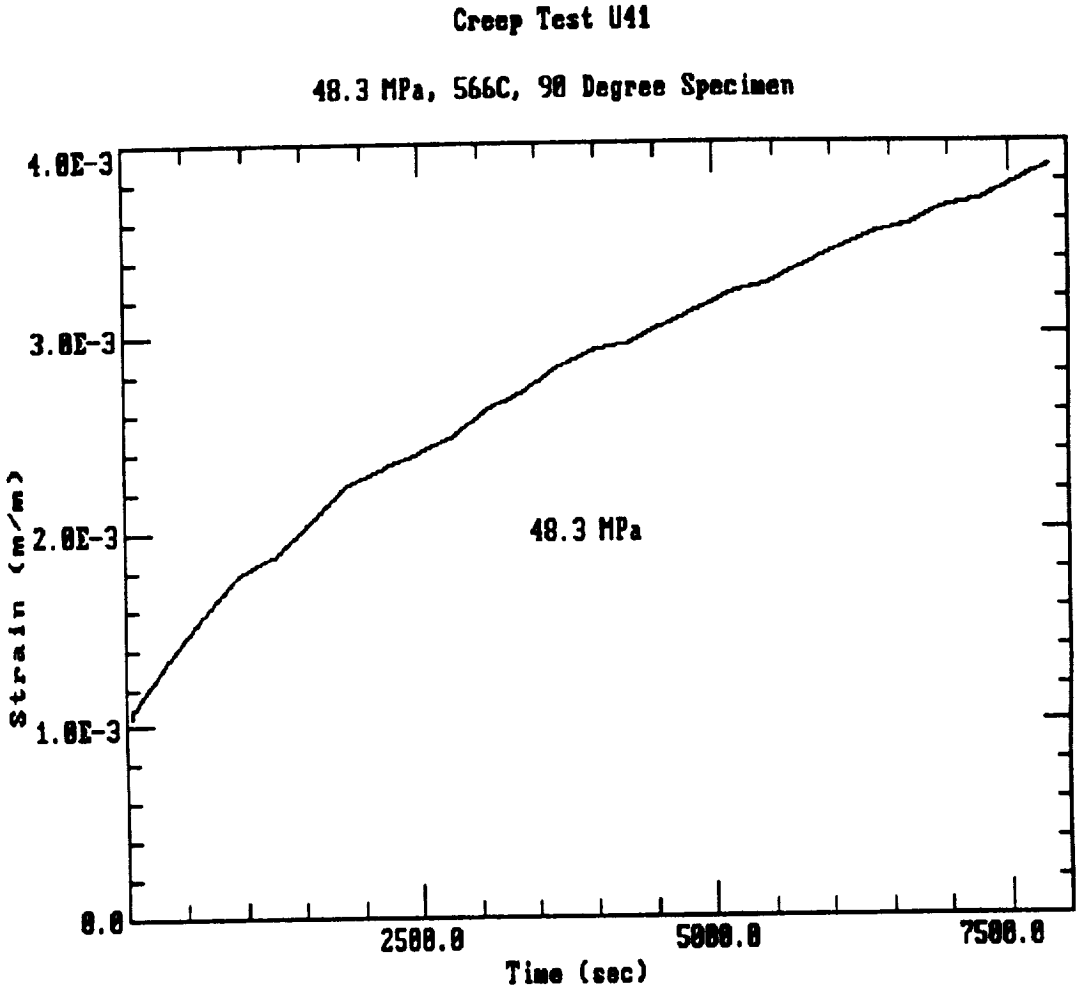

Figure A.1 Experimental creep test results of a .29 V_f 90 laminate at 566 C and 48.3 MPa

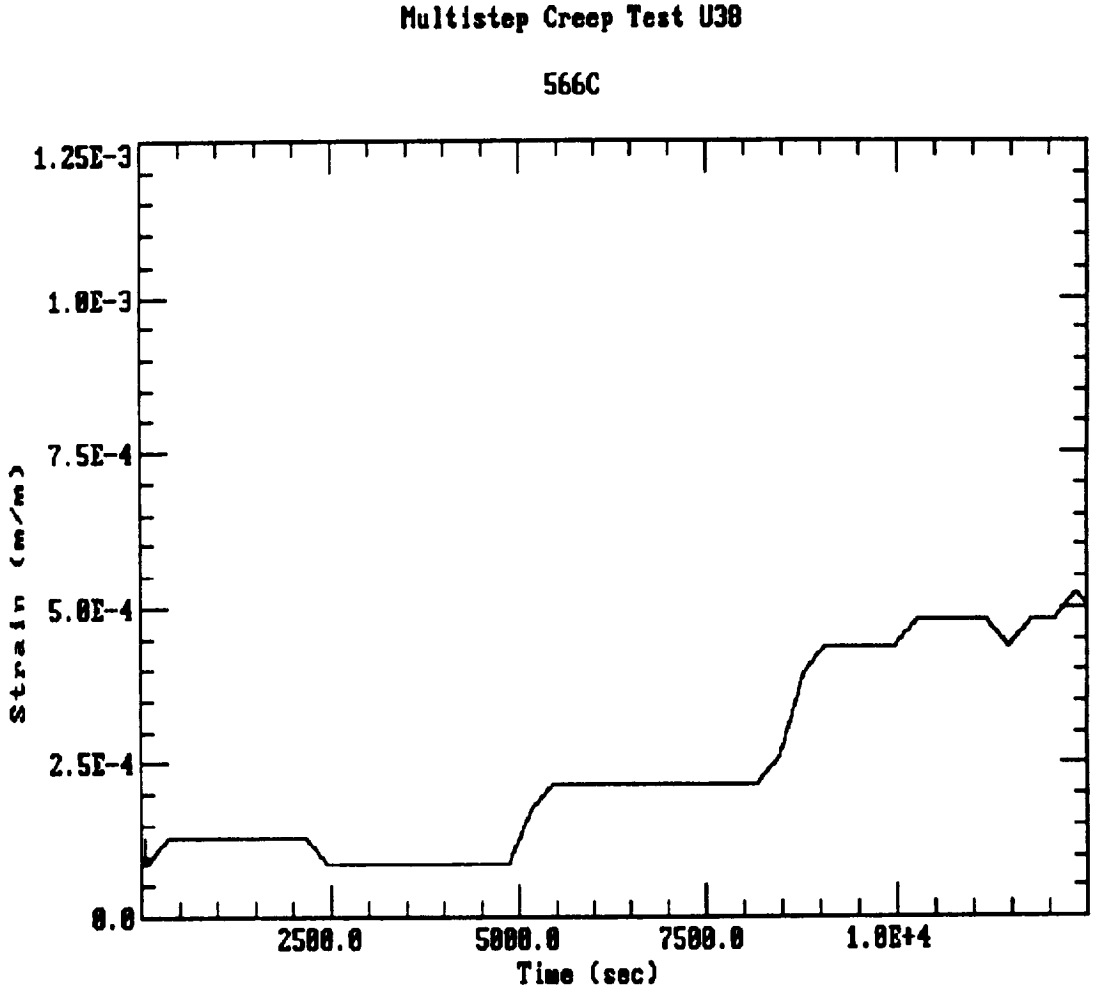

Figure A.2 Experimental creep test results of a .29 V_f 0 laminate at 566 C and various creep stresses.

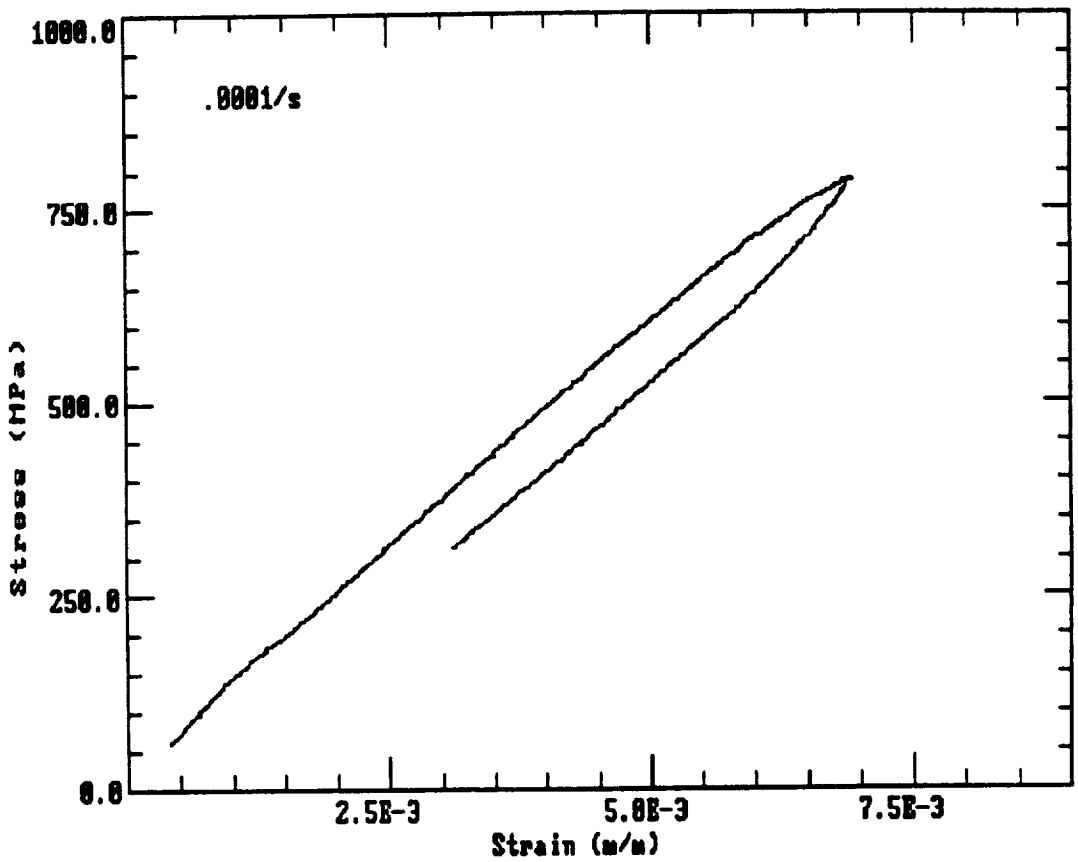

Figure A.3: Experimental CSR results for a 0 laminate at 649 C and .0001 m/m/sec.

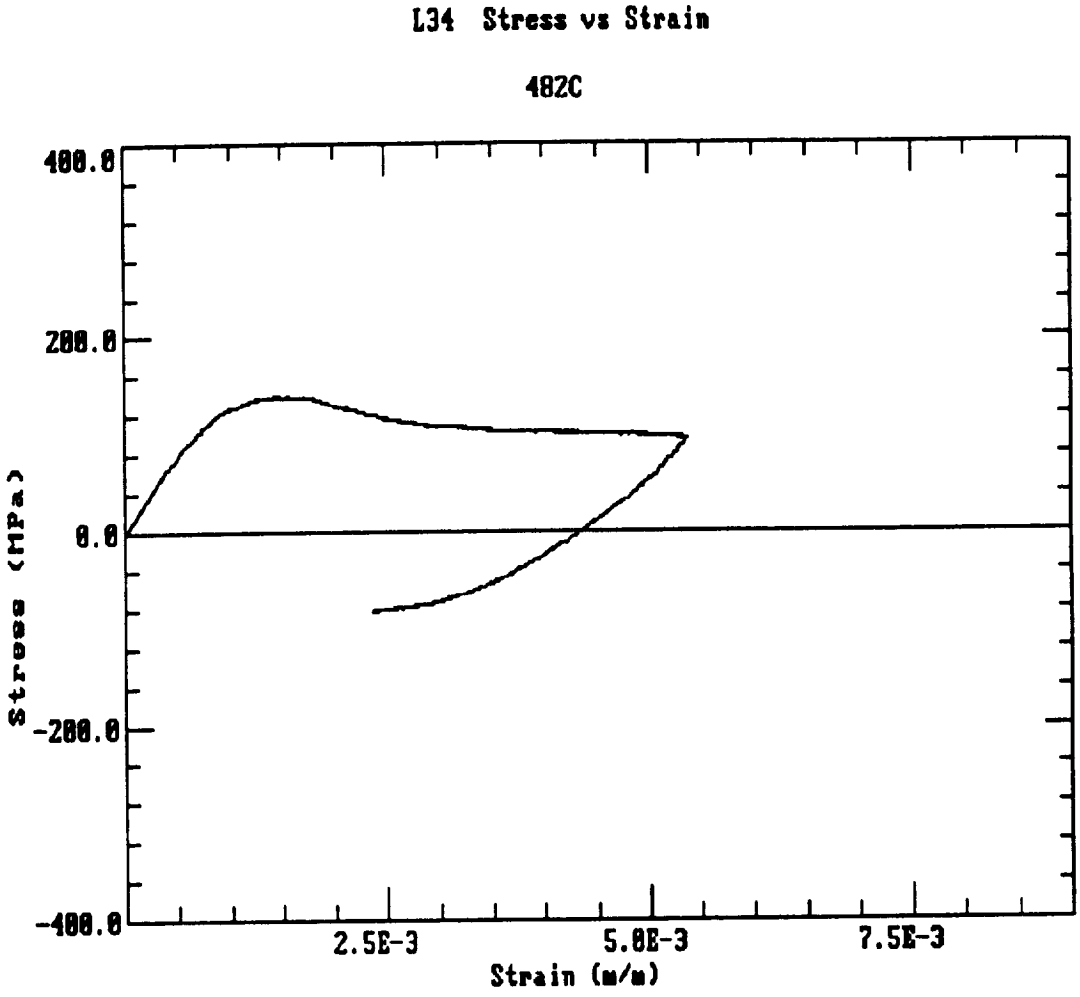

Figure A. 4 Experimental CSR results for a 90 laminate at 482 C and .0001 m/m/sec.

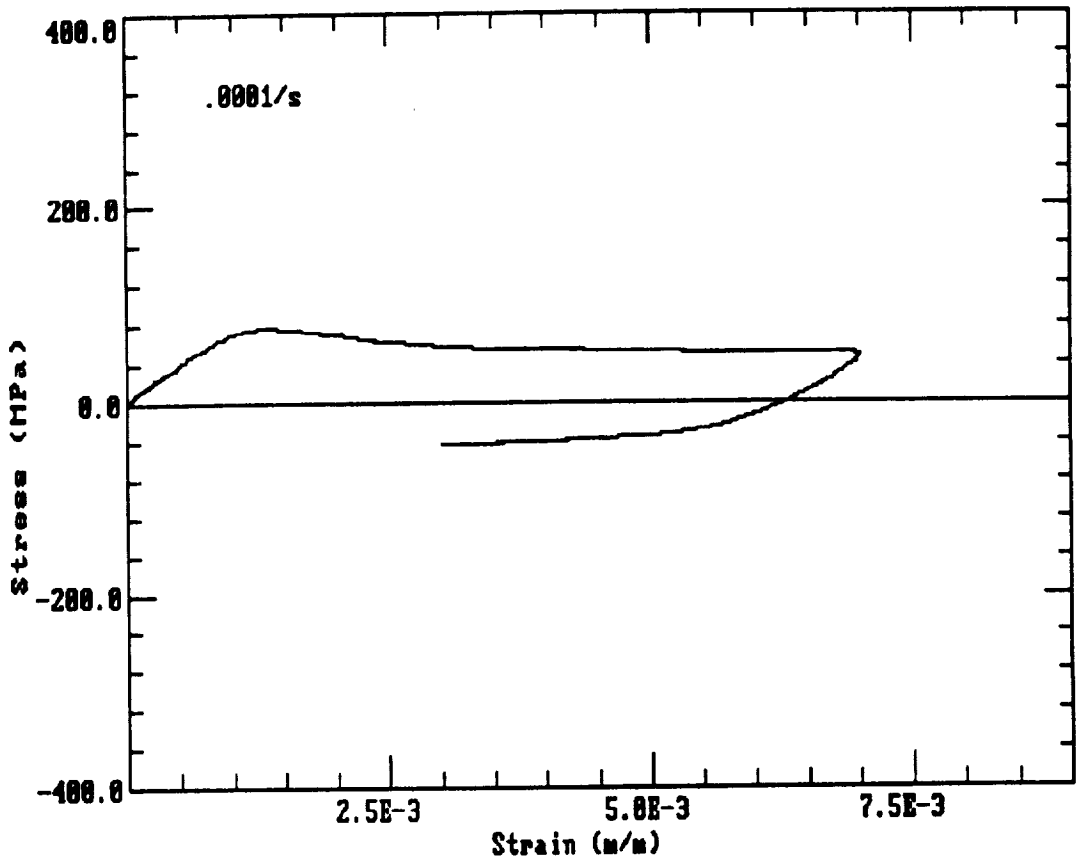

Figure A. 5 Experimental CSR results for a 90 laminate at 566 C and .0001 m/m/sec.

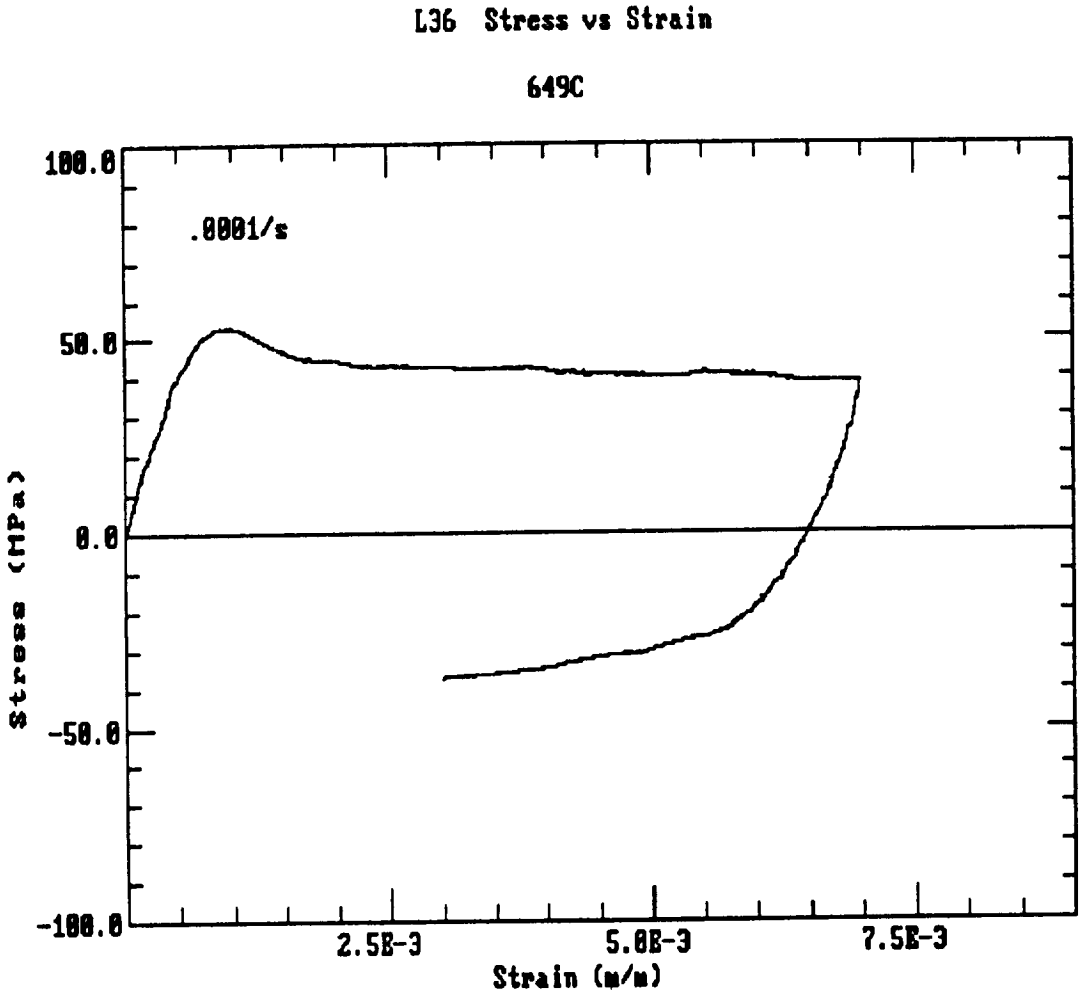

Figure A.6 Experimental CSR results for a 90 laminate at 566 C and .0001 m/m/sec.

APPENDIX B

COMPARISON OF PREDICTED AND MEASURED BEHAVIOR

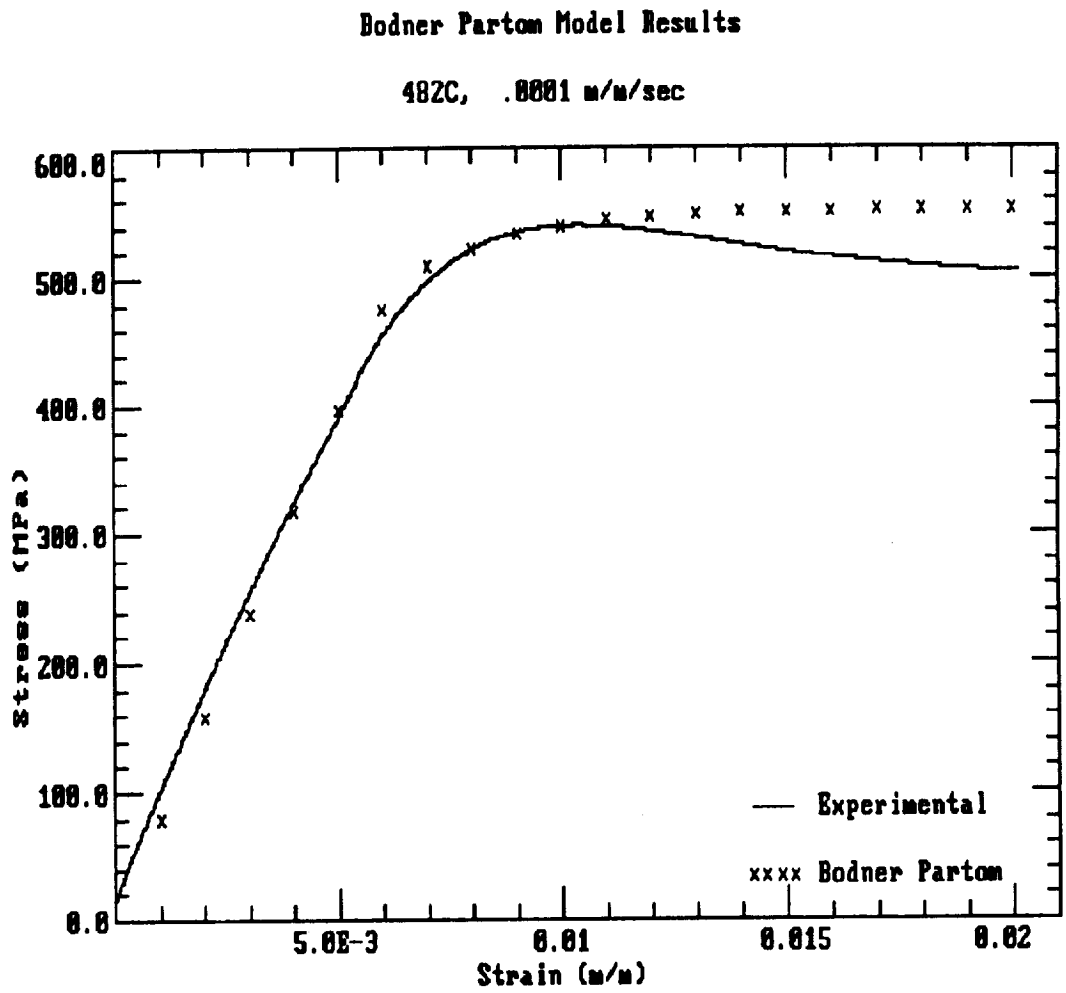

Figure B.1 Bodner-Partom model prediction vs experimental results for Ti-15-3, CSR test at 482 C, .0001 m/m/sec.

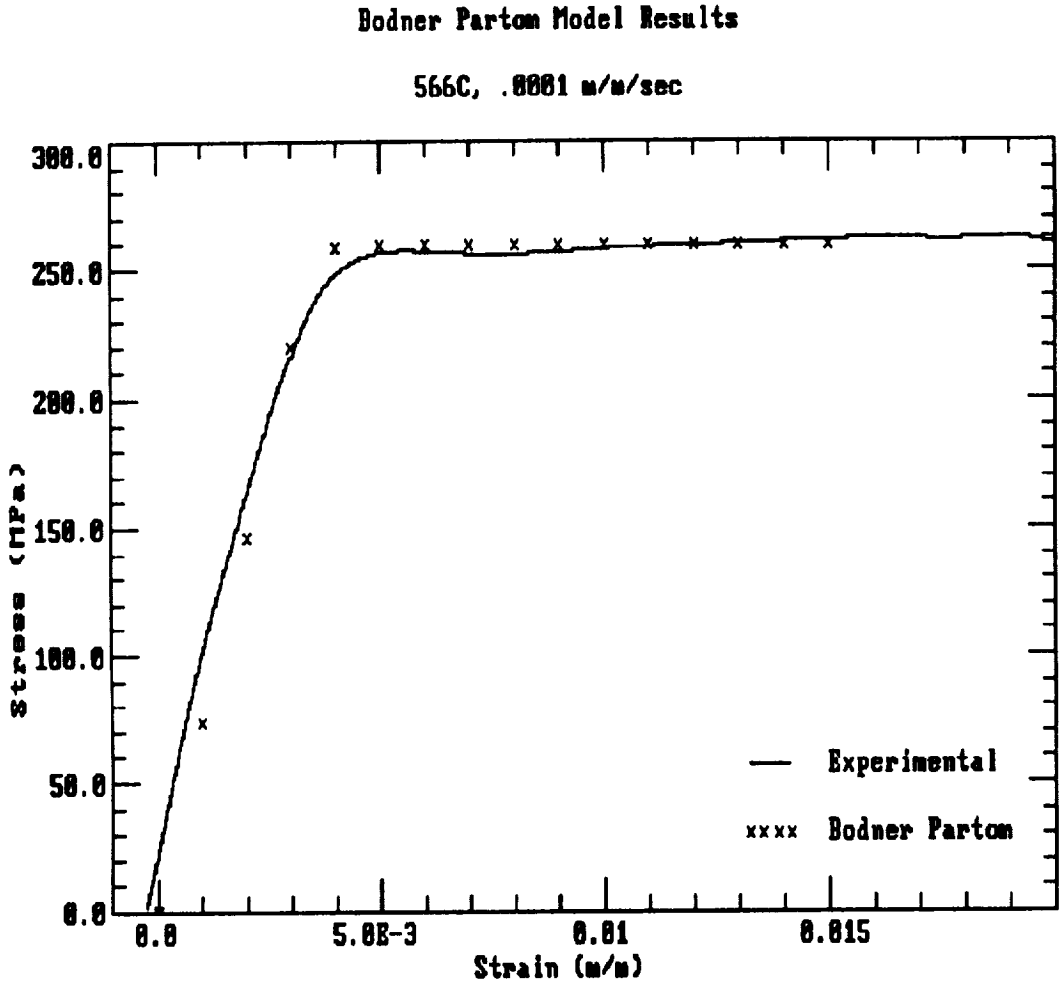

Figure B.2 Bodner-Partom model prediction vs experimental results for Ti-15-3, CSR test at 566 C, .0001 m/m/sec.

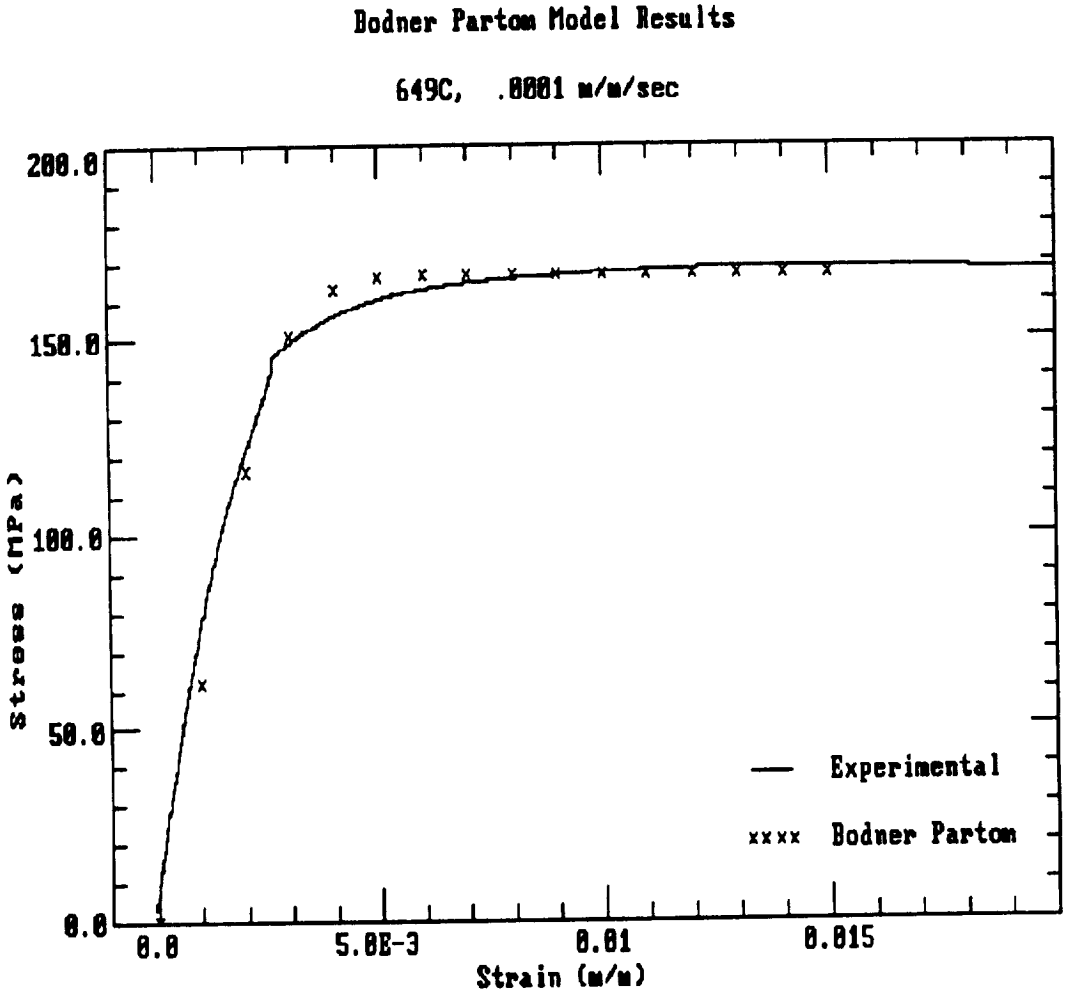

Figure B.3 Bodner-Partom model prediction vs experimental results for Ti-15-3, CSR test at 649 C, .0001 m/m/sec.

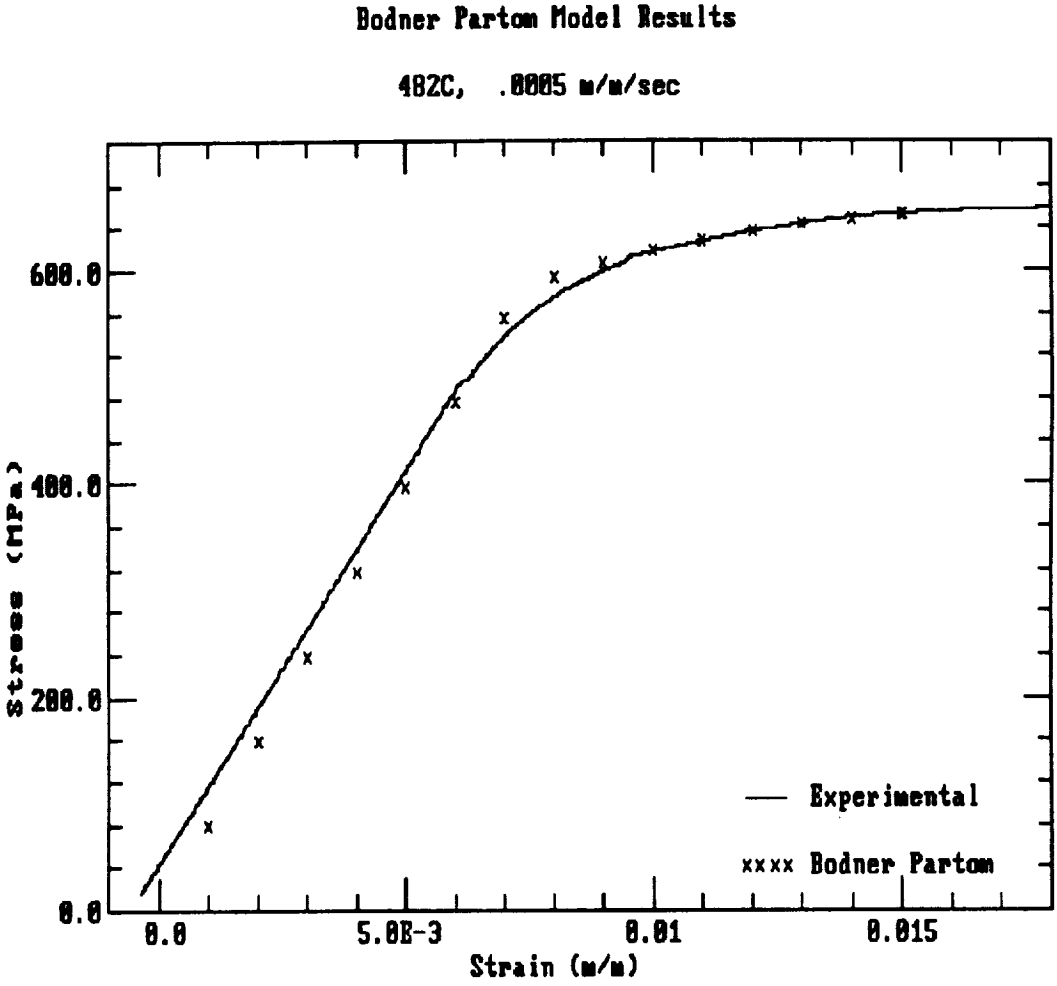

Figure B.4 Bodner-Partom model prediction vs experimental results for Ti-15-3, CSR test at 482 C, .0005 m/m/sec.

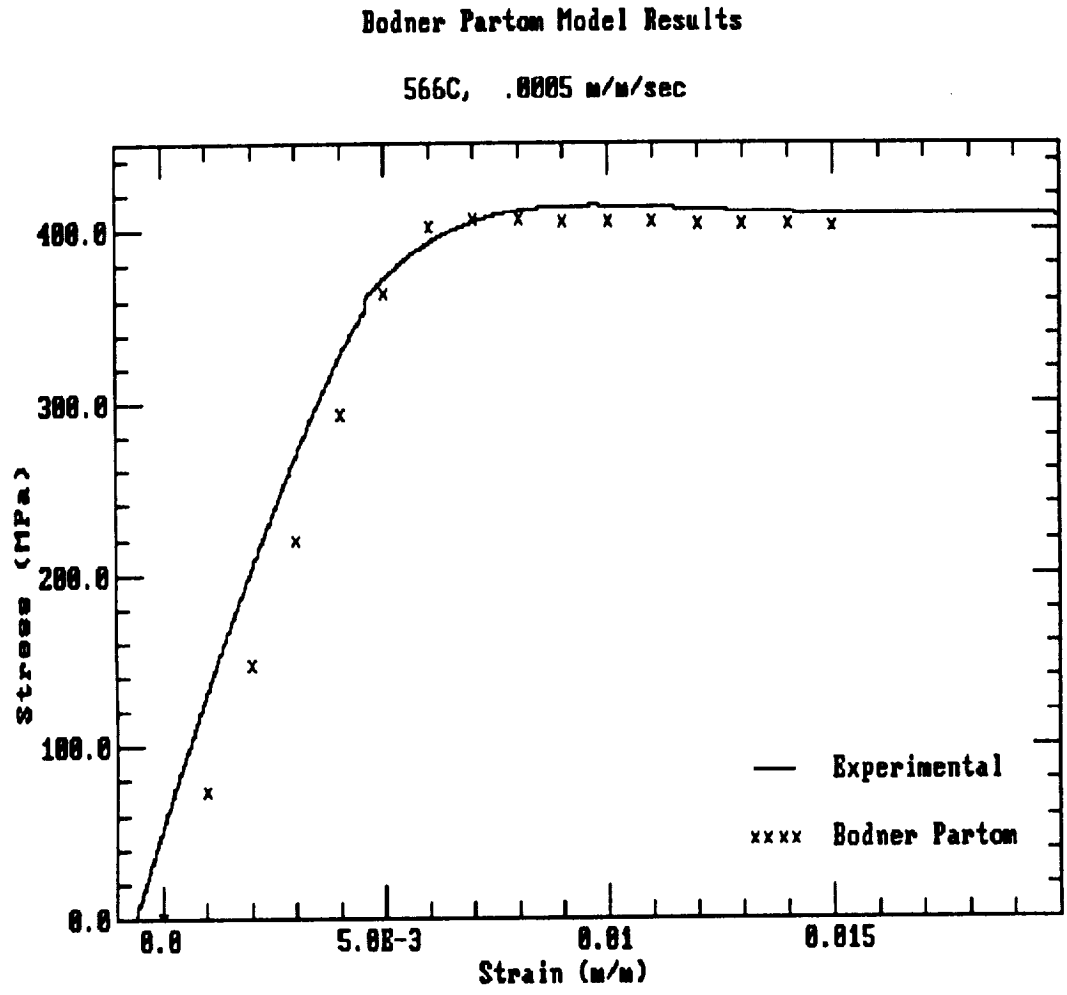

Figure B.5 Bodner-Partom model prediction vs experimental results for Ti-15-3, CSR test at 566 C, .0005 m/m/sec.

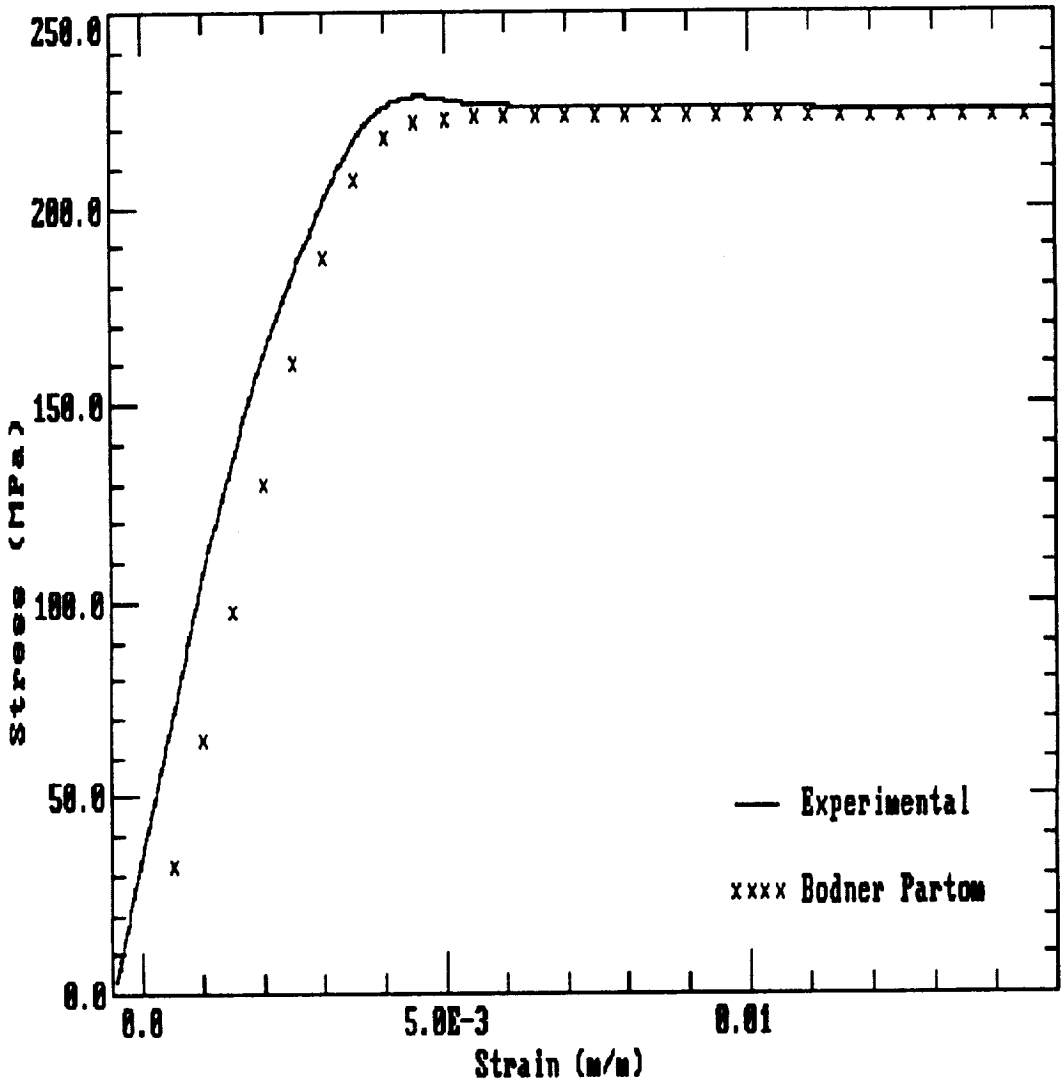

Figure B.6 Bodner-Partom model prediction vs experimental results for Ti-15-3, CSR test at 649 C, .0005 m/m/sec.

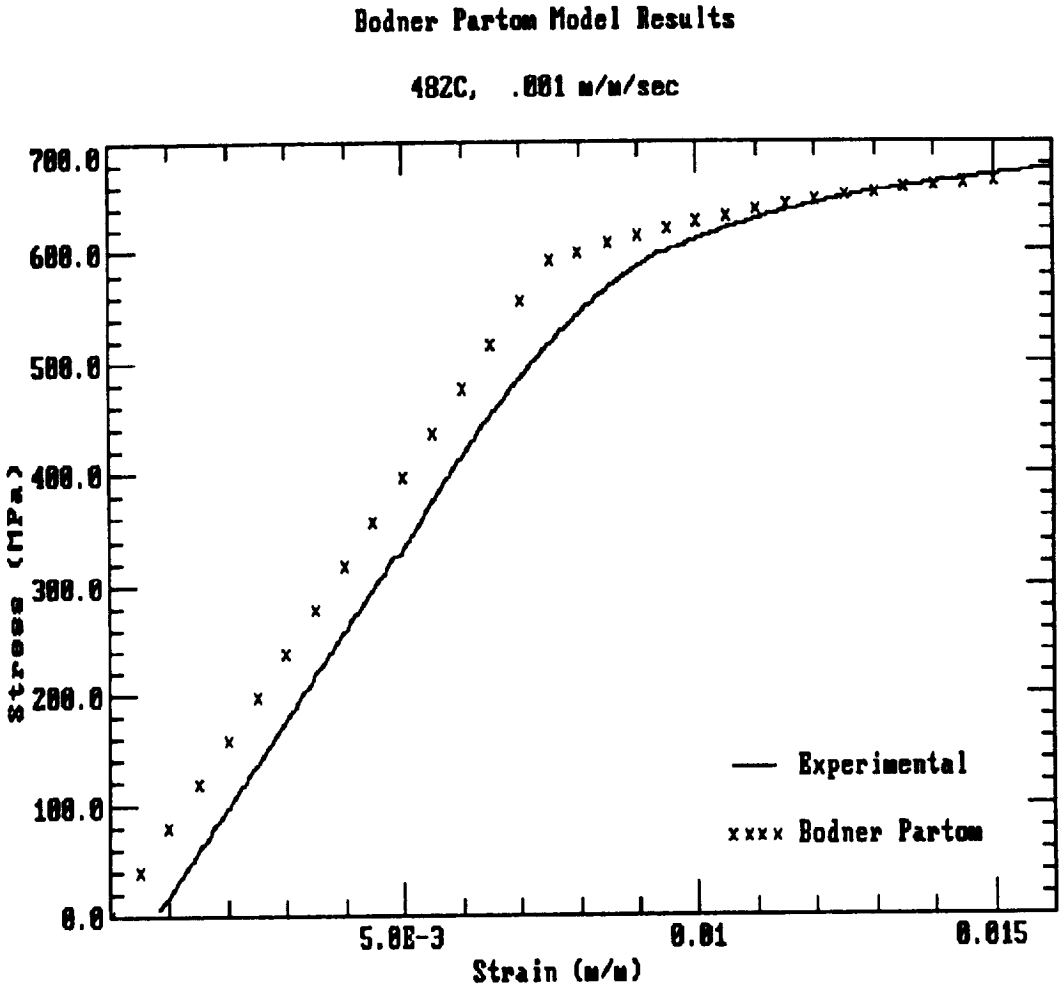

Figure B.7 Bodner-Partom model prediction vs experimental results for Ti-15-3, CSR test at 482 C, .001 m/m/sec.

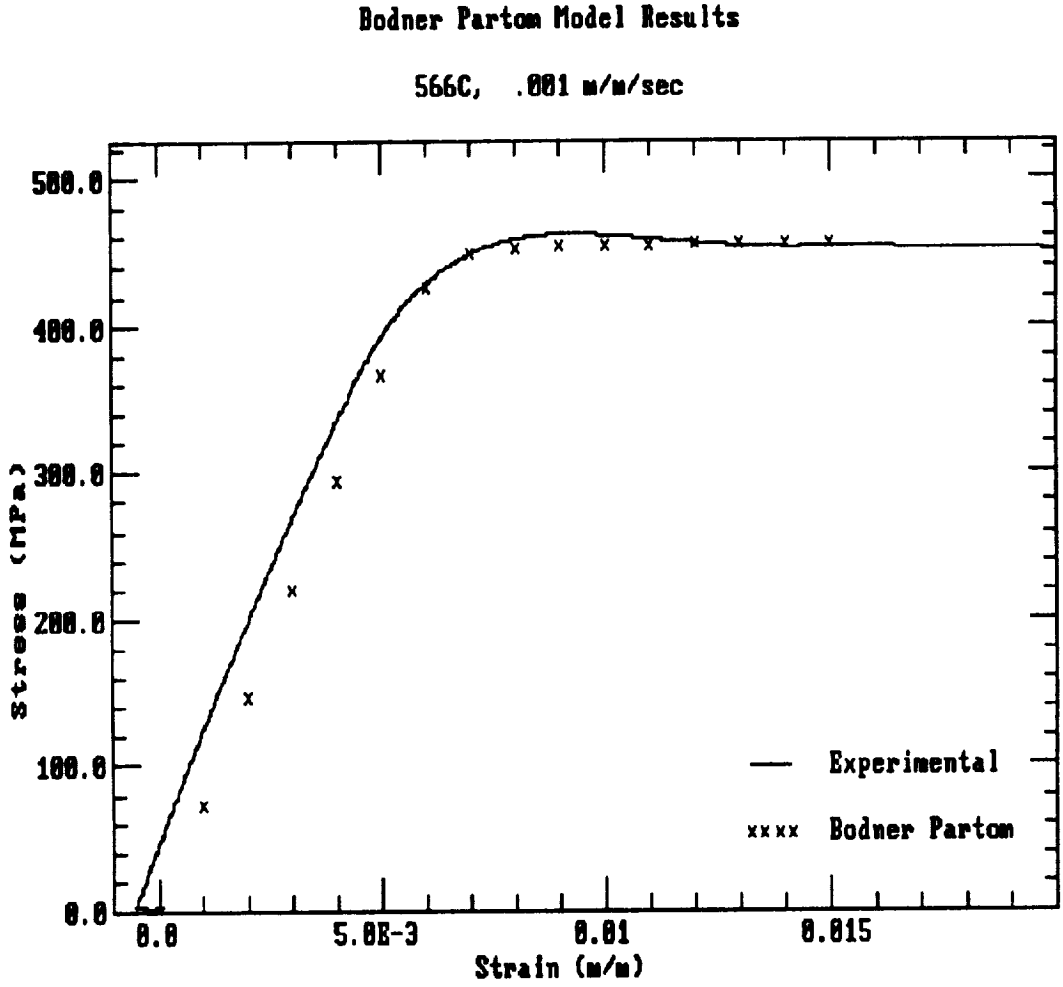

Figure B.8 Bodner-Partom model prediction vs experimental results for Ti-15-3, CSR test at 566 C, .001 m/m/sec.

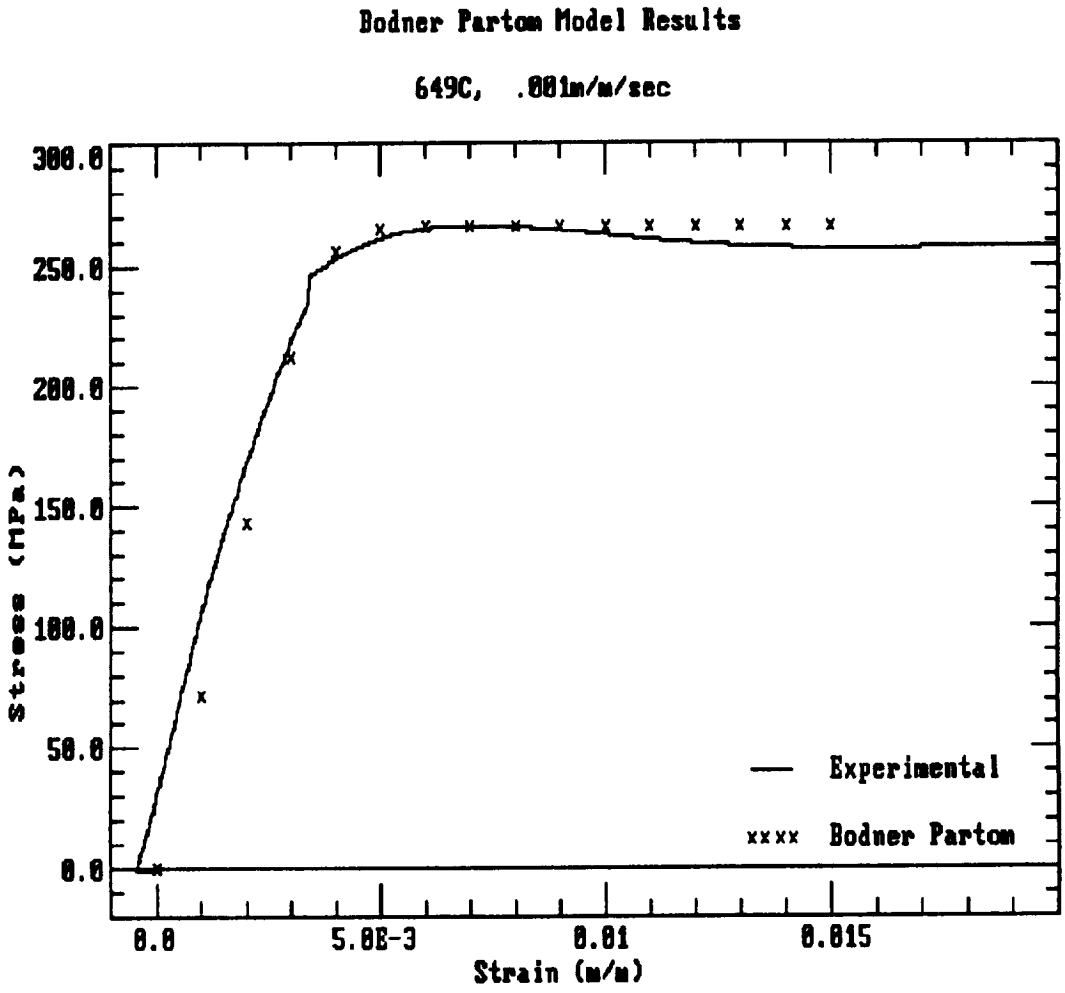

Figure B.9 Bodner-Partom model prediction vs experimental results for Ti-15-3, CSR test at 649 C, .001 m/m/sec.

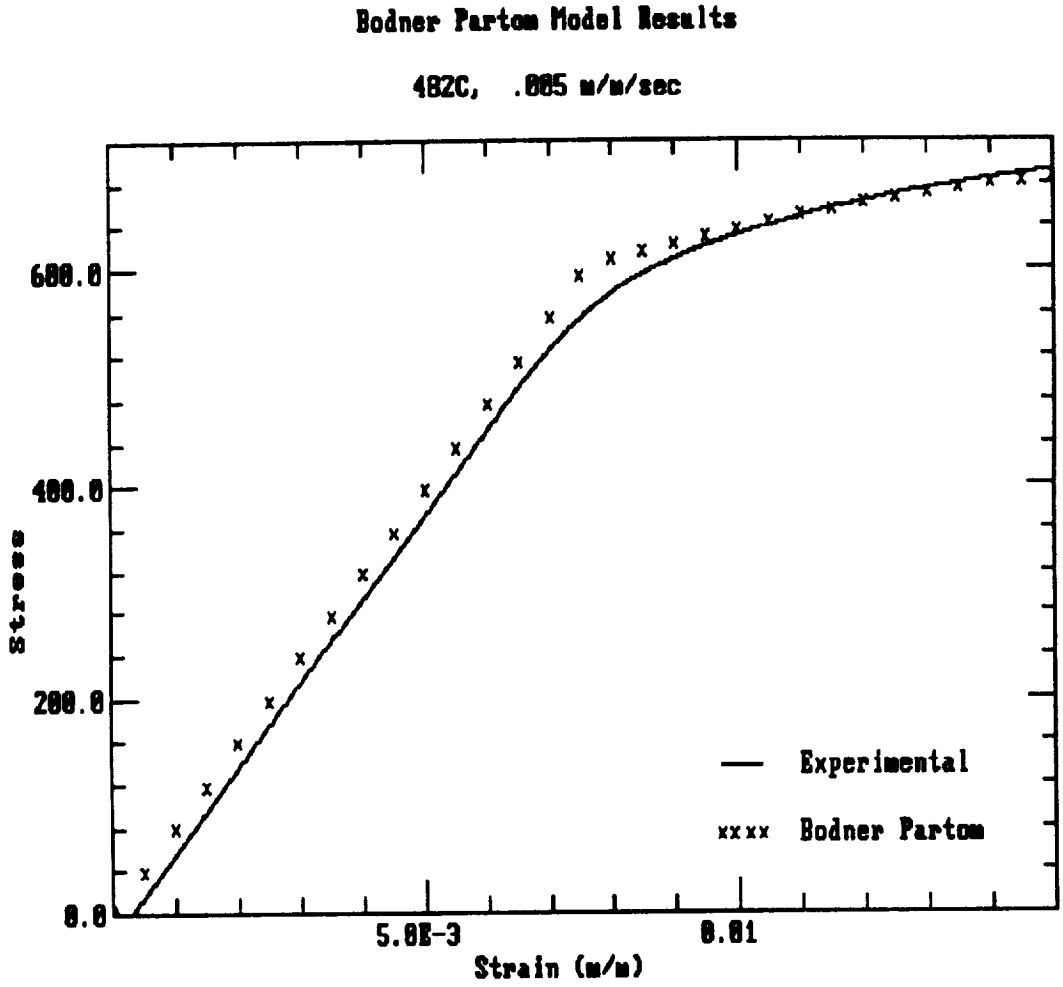

Figure B.10 Bodner-Partom model prediction vs experimental results for Ti-15-3, CSR test at 482 C, .005 m/m/sec.

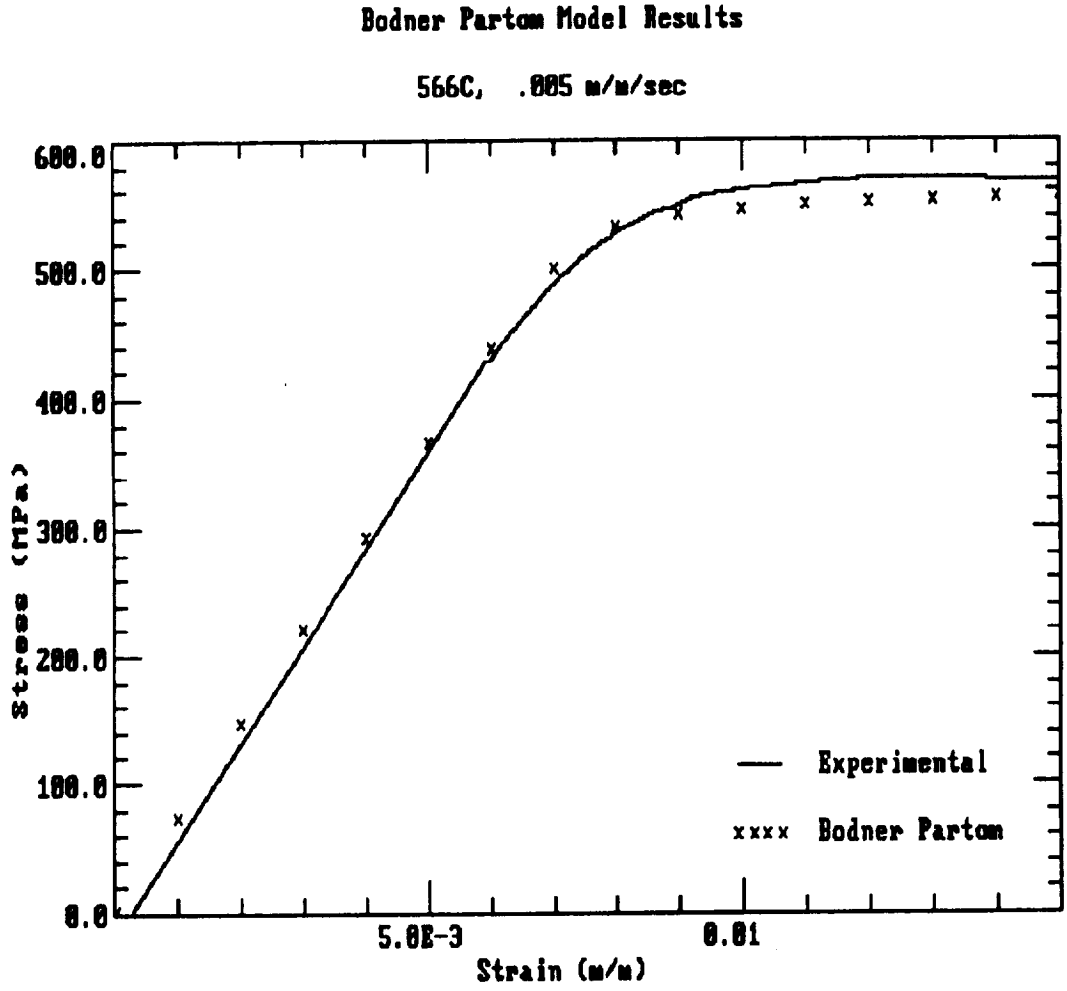

Figure B.11 Bodner-Partom model prediction vs experimental results for Ti-15-3, CSR test at 566 C, .005 m/m/sec.

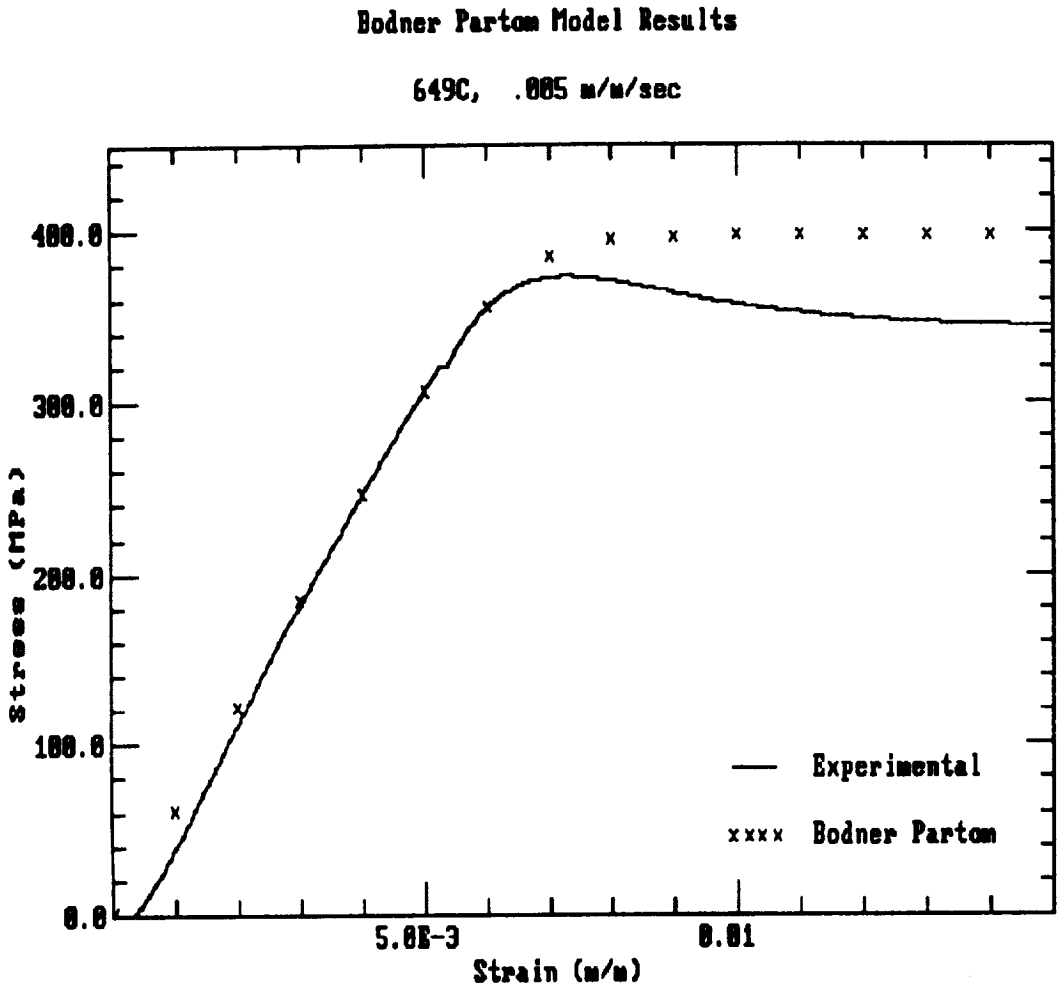

Figure B.12 Bodner-Partom model prediction vs experimental results for Ti-15-3, CSR test at 649 C, .005 m/m/sec.

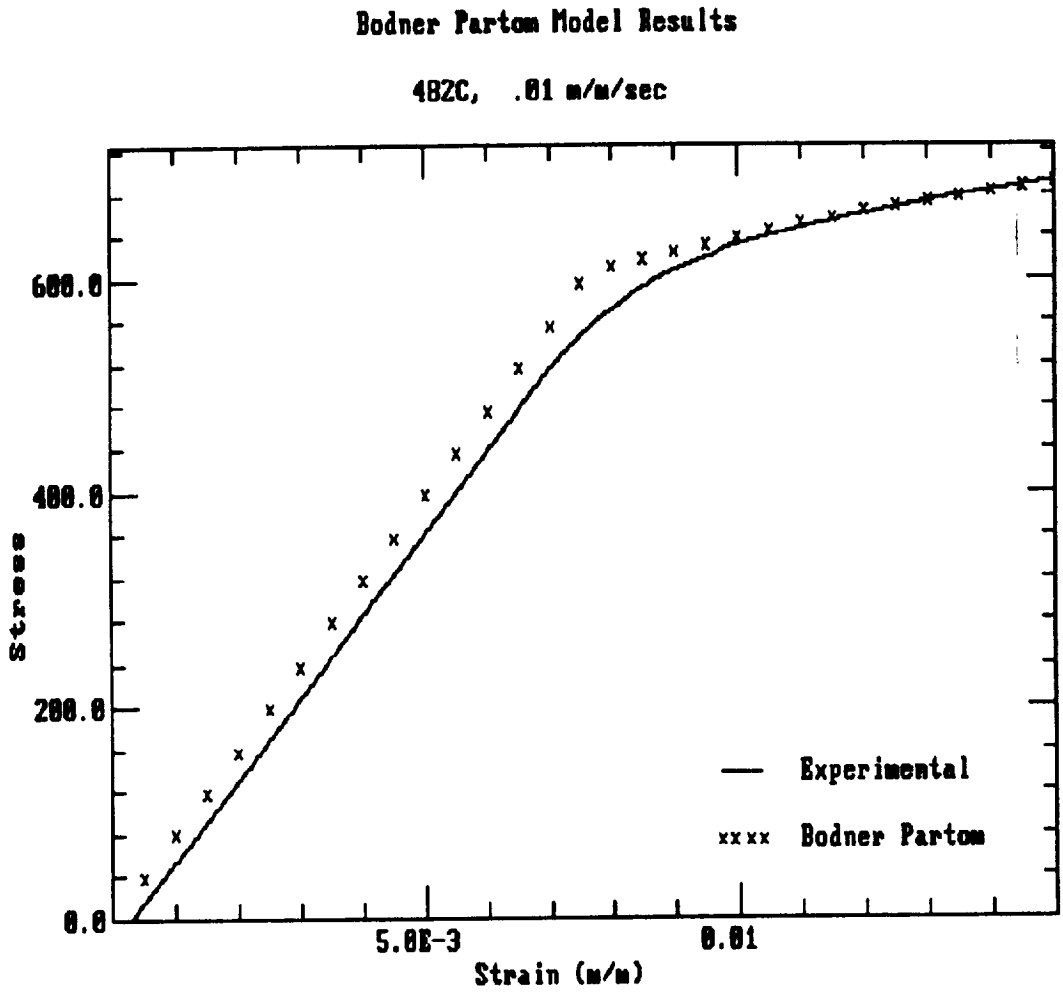

Figure B.13 Bodner-Partom model prediction vs experimental results for Ti-15-3, CSR test at 482 C, .01 m/m/sec.

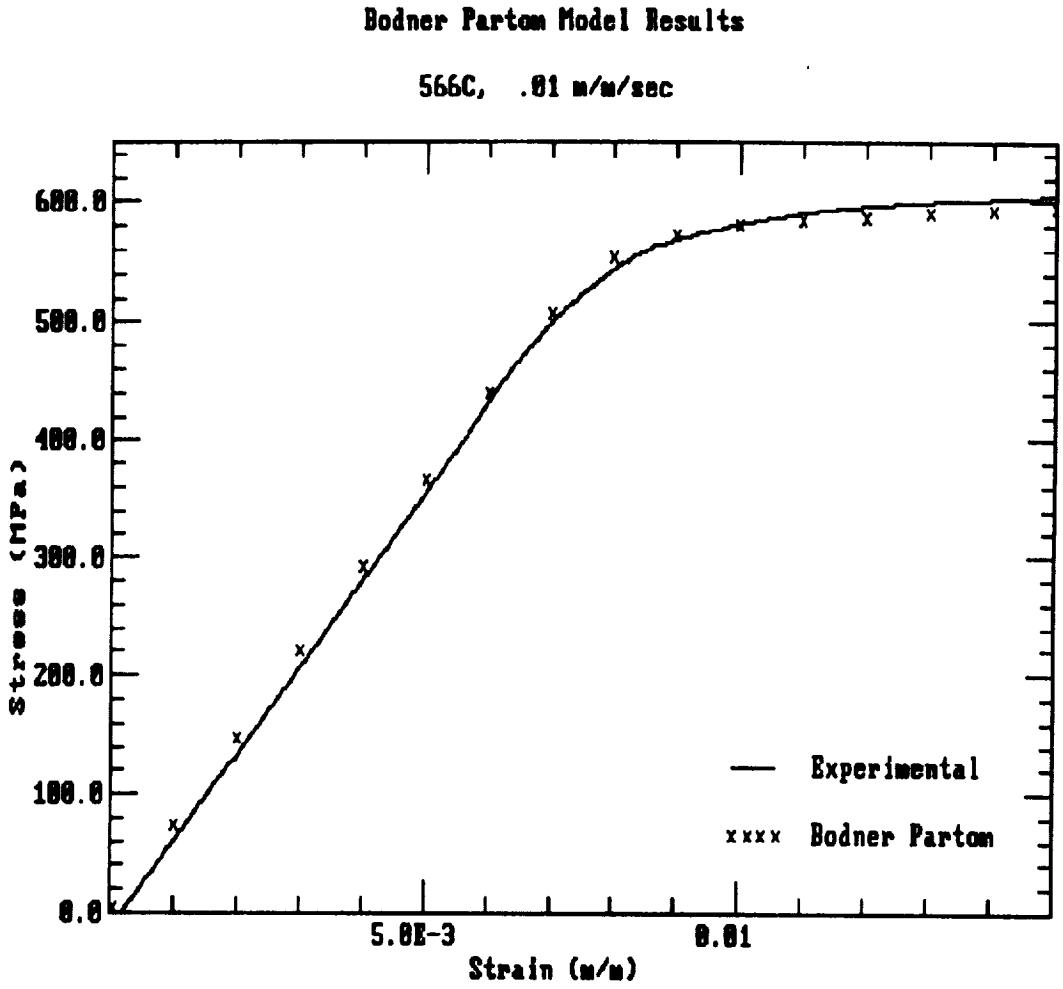

Figure B.14 Bodner-Partom model prediction vs experimental results for Ti-15-3, CSR test at 566 C, .01 m/m/sec.

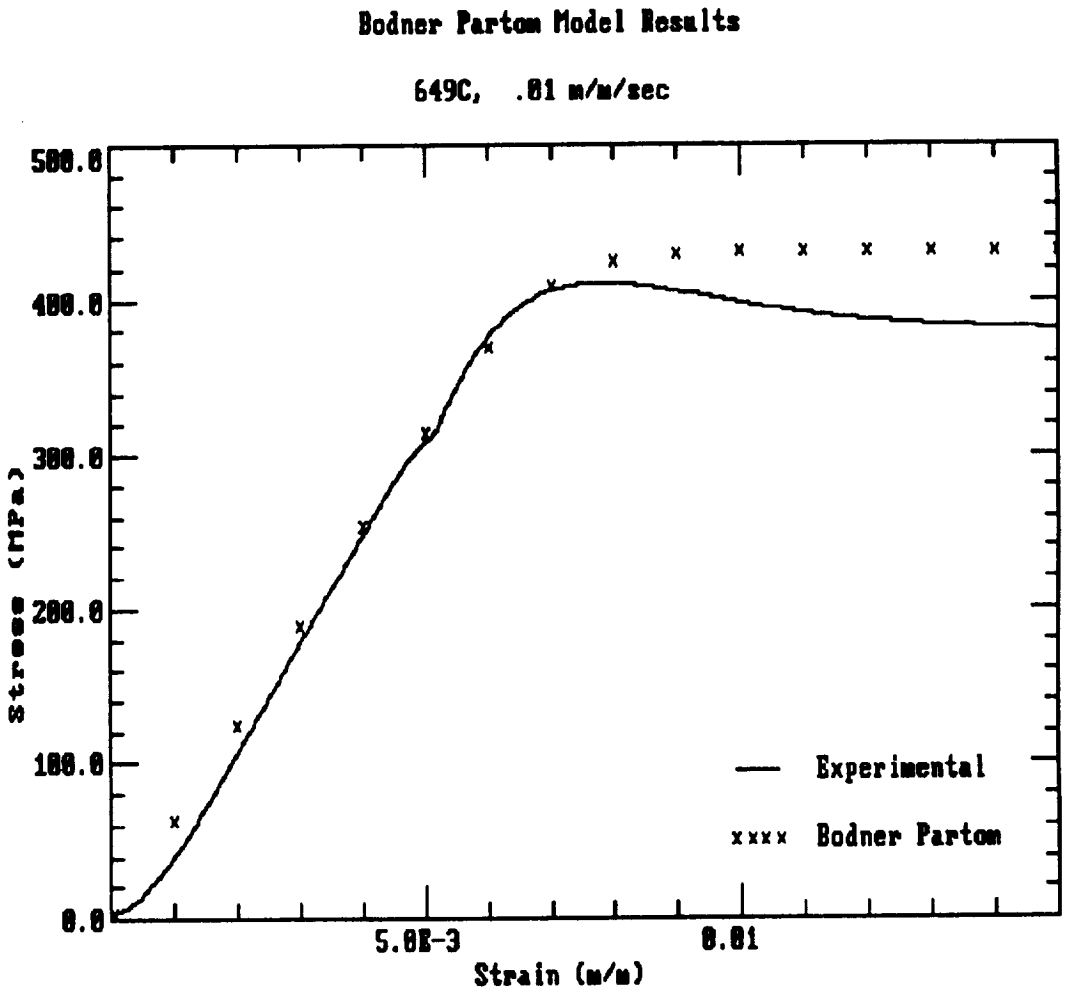

Figure B.15 Bodner-Partom model prediction vs experimental results for Ti-15-3, CSR test at 649 C, .01 m/m/sec.

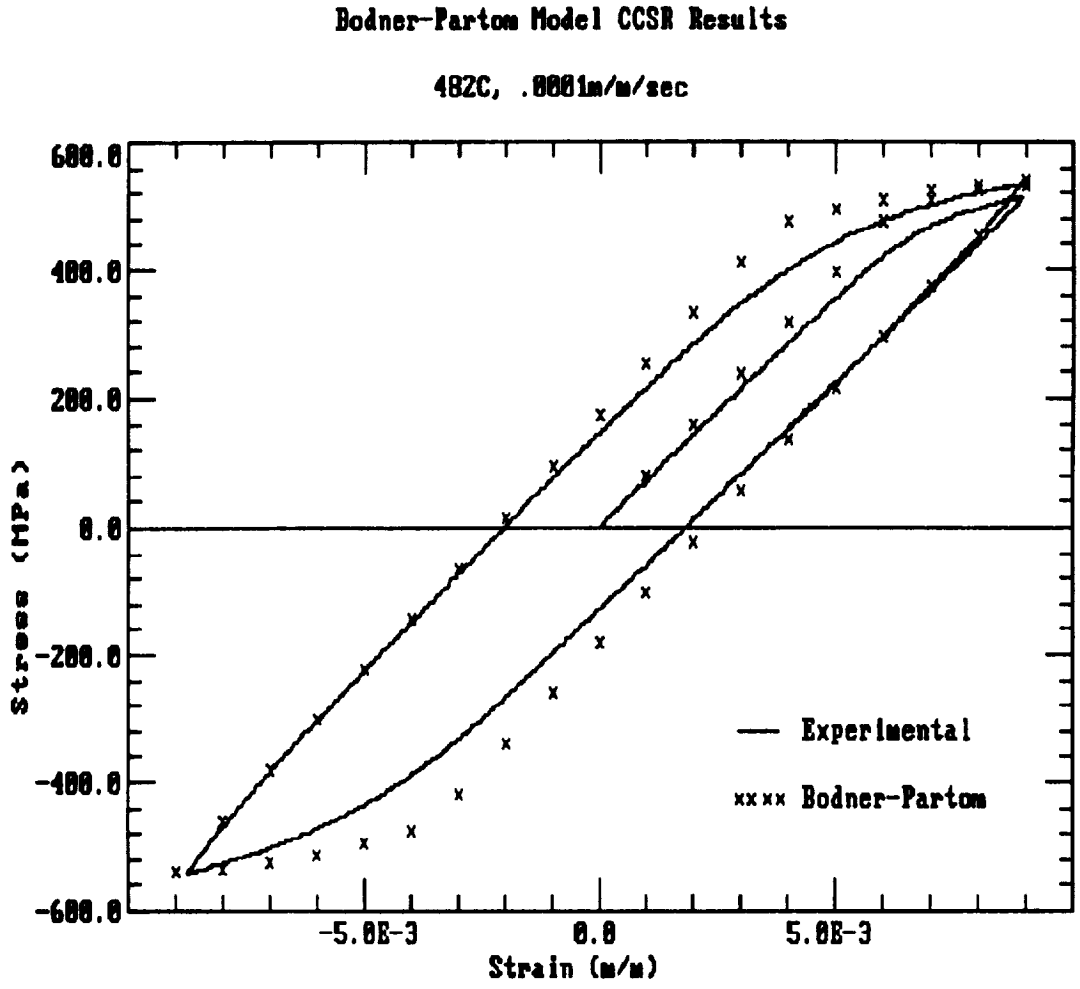

Figure B.16 Bodner-Partom model prediction vs experimental results for Ti-15-3, CCSR test at 482 C, .0001 m/m/sec.

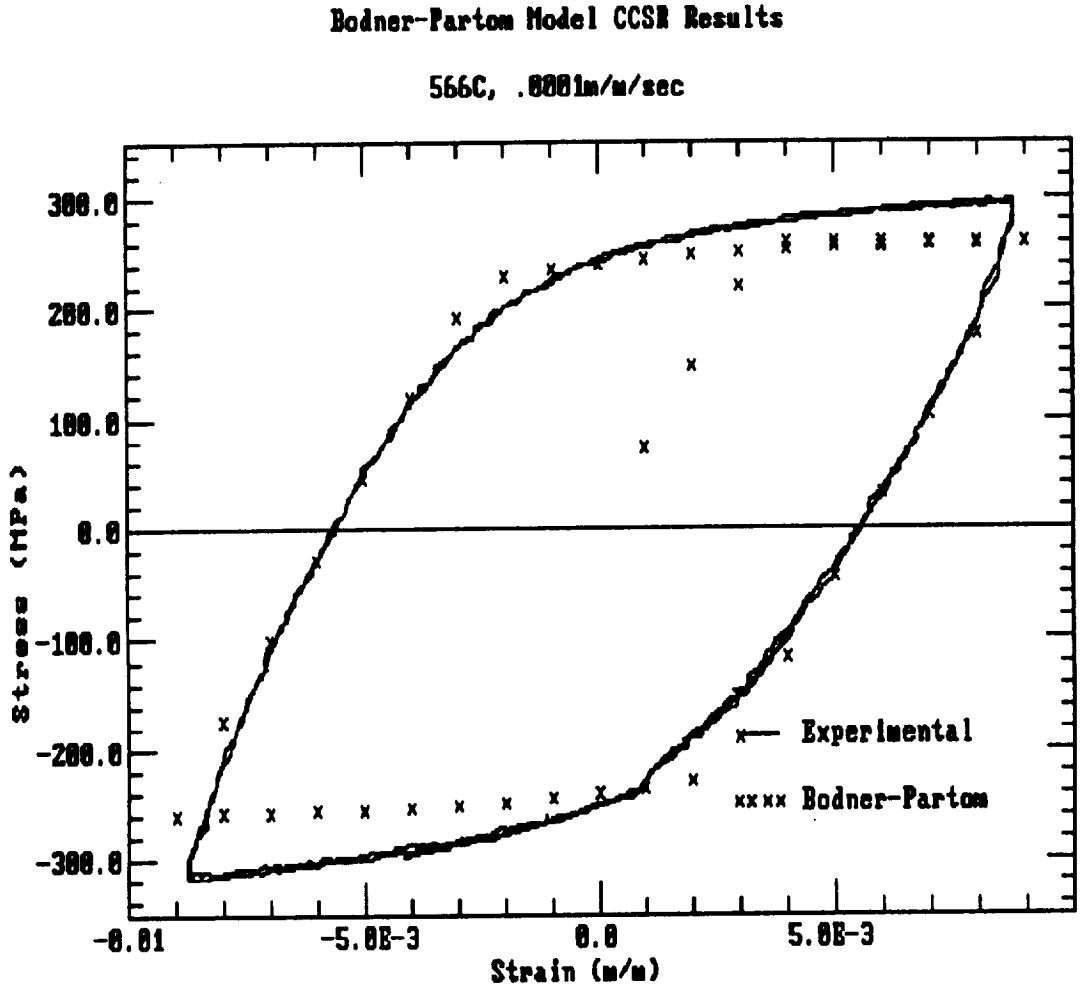

Figure B.17 Bodner-Partom model prediction vs experimental results for Ti-15-3, CCSR test at 566 C, .0001 m/m/sec.

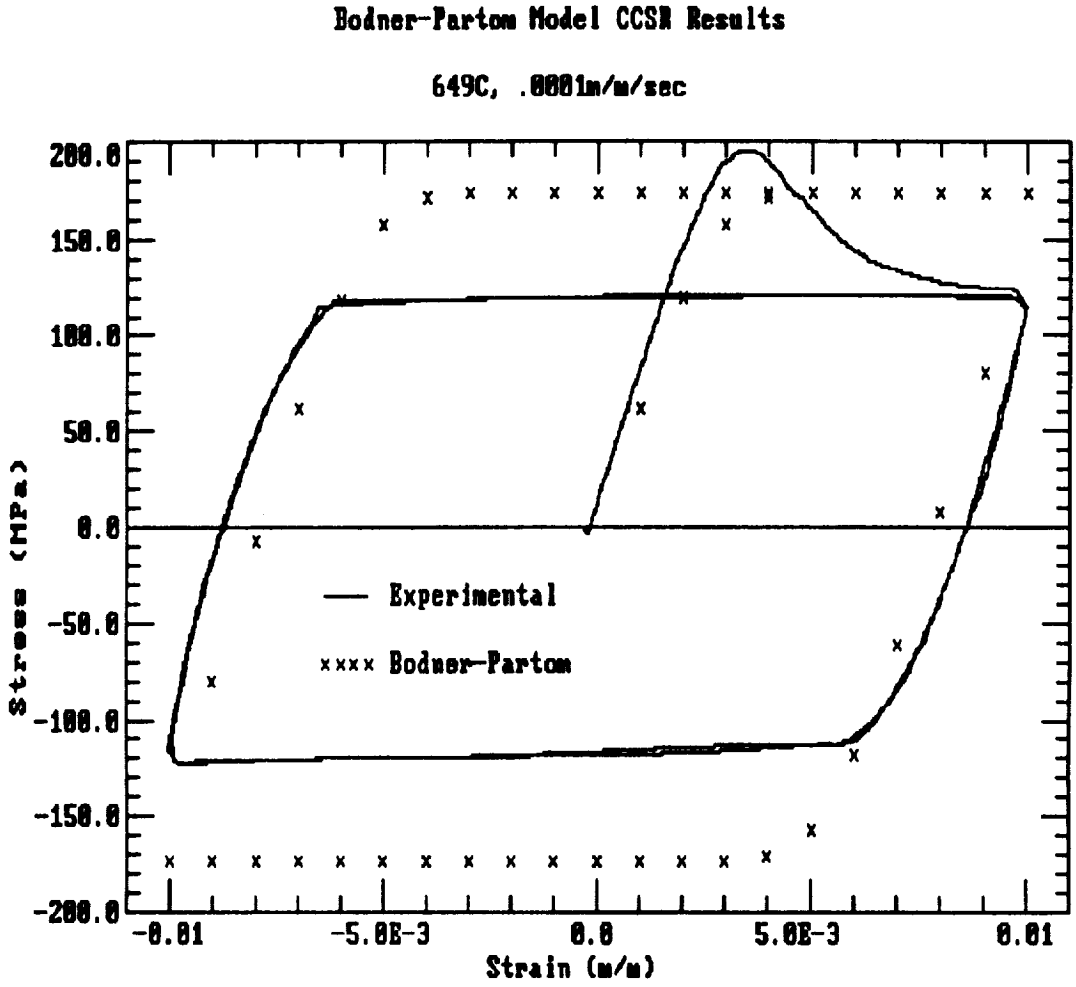

Figure B.18 Bodner-Partom model prediction vs experimental results for Ti-15-3, CCSR test at 649 C, .0001 m/m/sec.

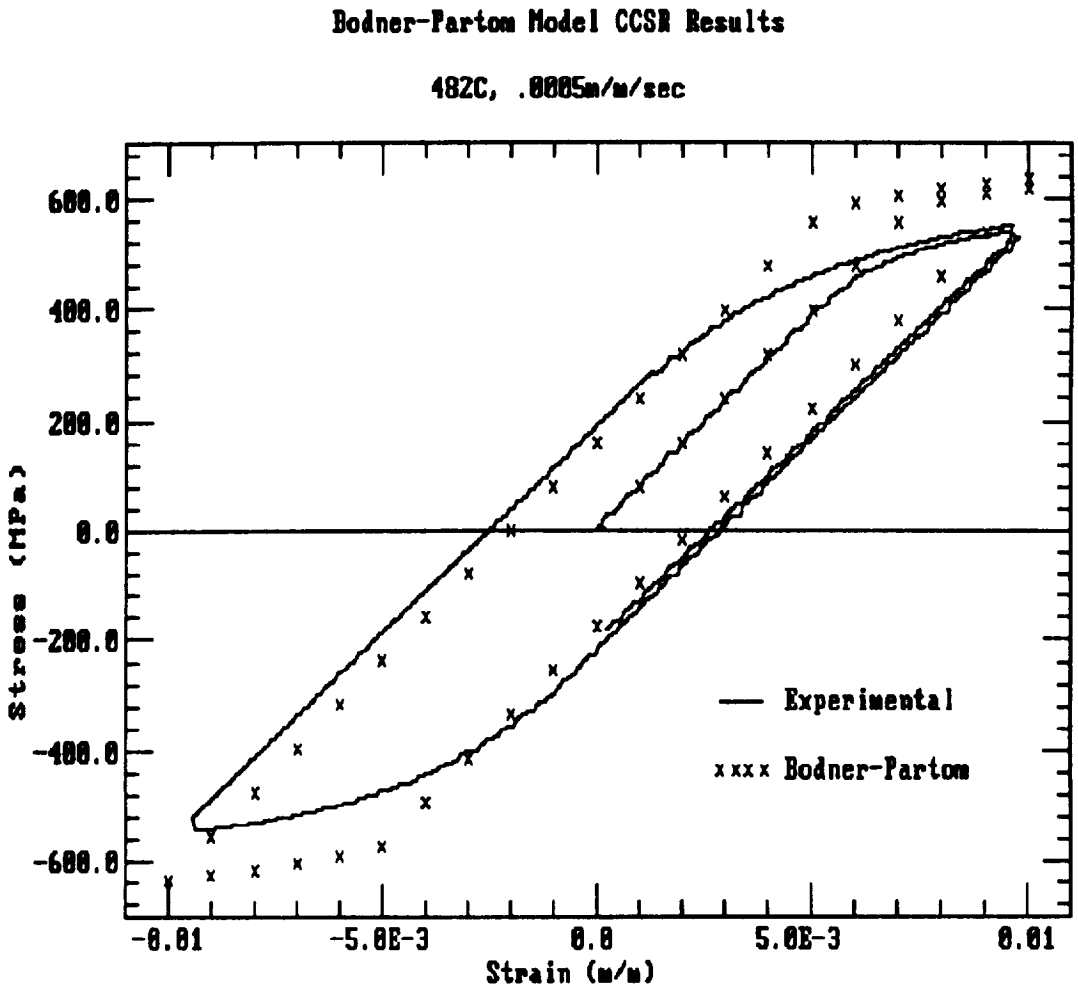

Figure B.19 Bodner-Partom model prediction vs experimental results for Ti-15-3, CCSR test at 482 C, .0005 m/m/sec.

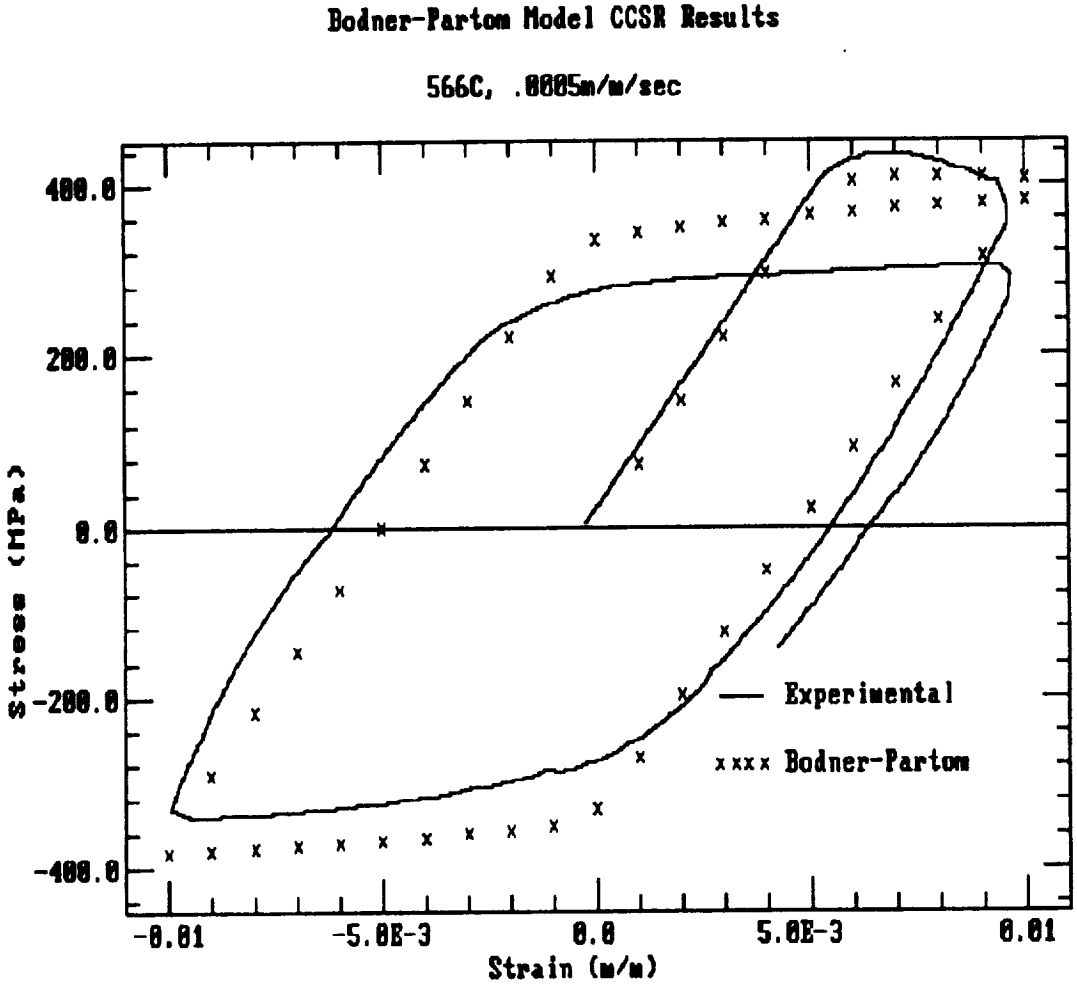

Figure B.20 Bodner-Partom model prediction vs experimental results for Ti-15-3, CCSR test at 566 C, .0005 m/m/sec.

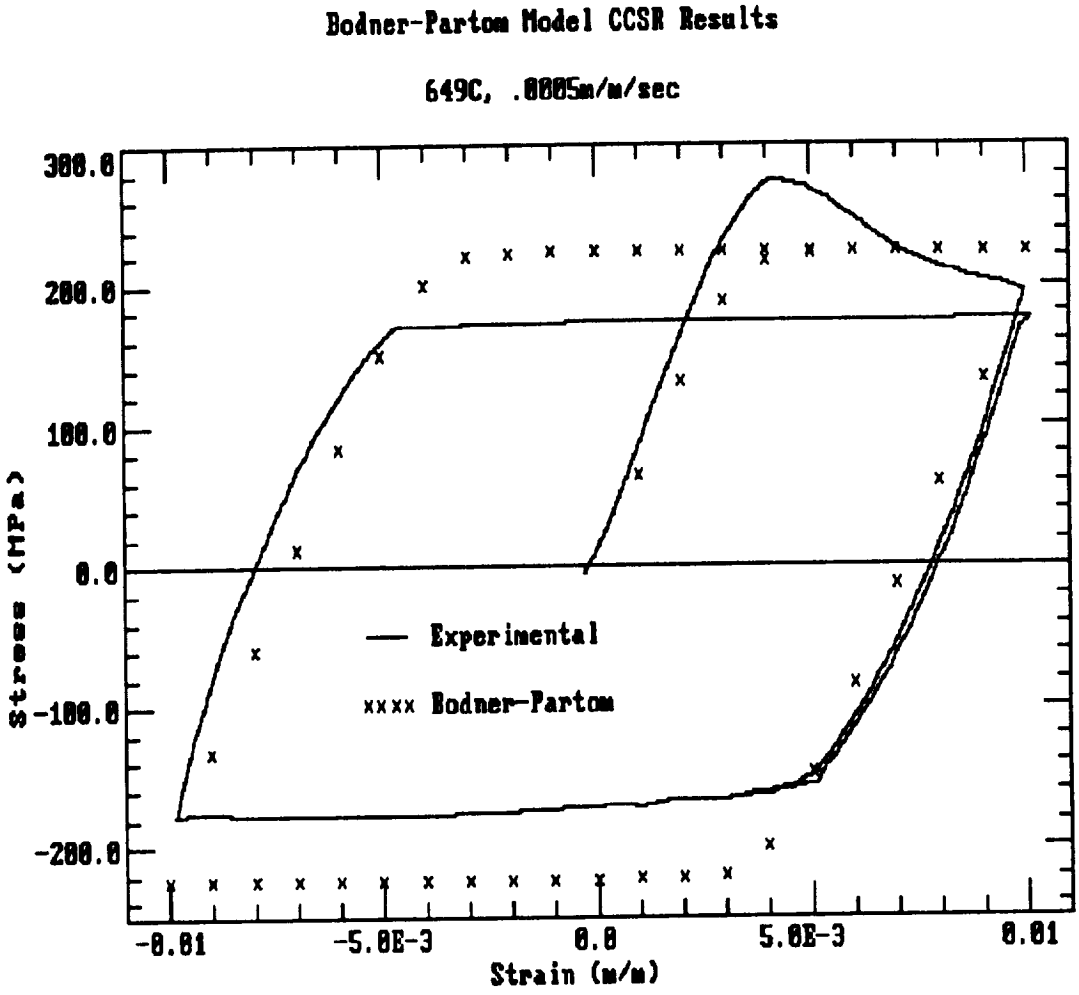

Figure B.21 Bodner-Partom model prediction vs experimental results for Ti-15-3, CCSR test at 649 C, .0005 m/m/sec.

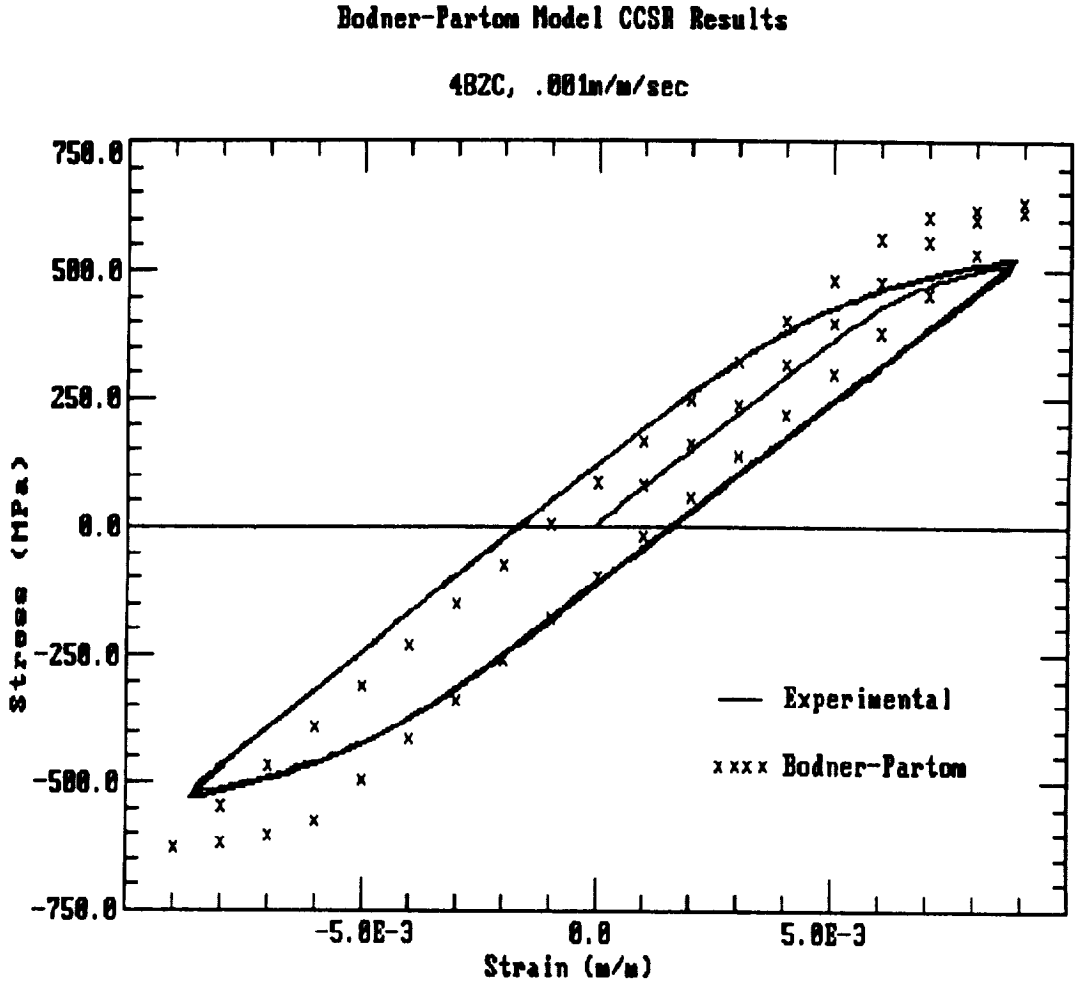

Figure B.22 Bodner-Partom model prediction vs experimental results for Ti-15-3, CCSR test at 482 C, .001 m/m/sec.

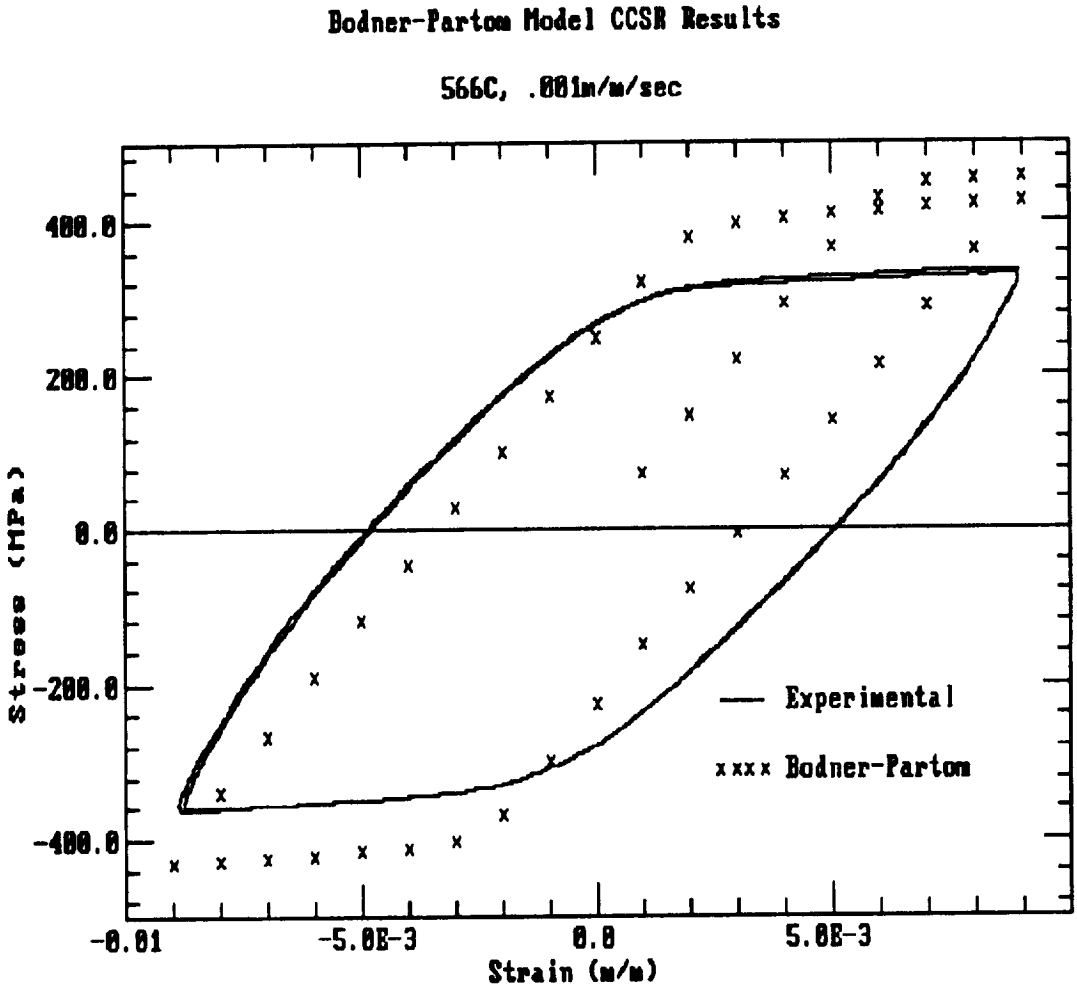

Figure B.23 Bodner-Partom model prediction vs experimental results for Ti-15-3, CCSR test at 566 C, .001 m/m/sec.

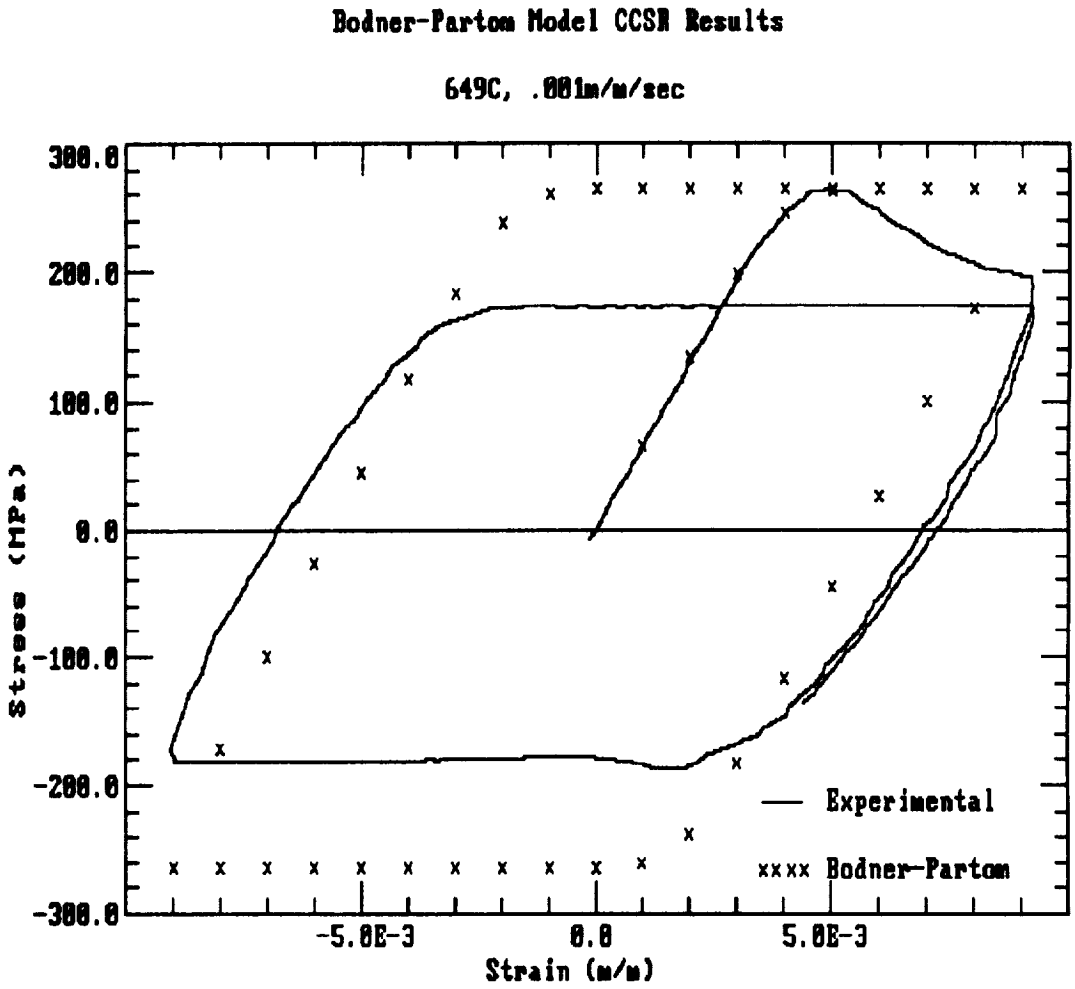

Figure B.24 Bodner-Partom model prediction vs experimental results for Ti-15-3, CCSR test at 649 C, .001 m/m/sec.

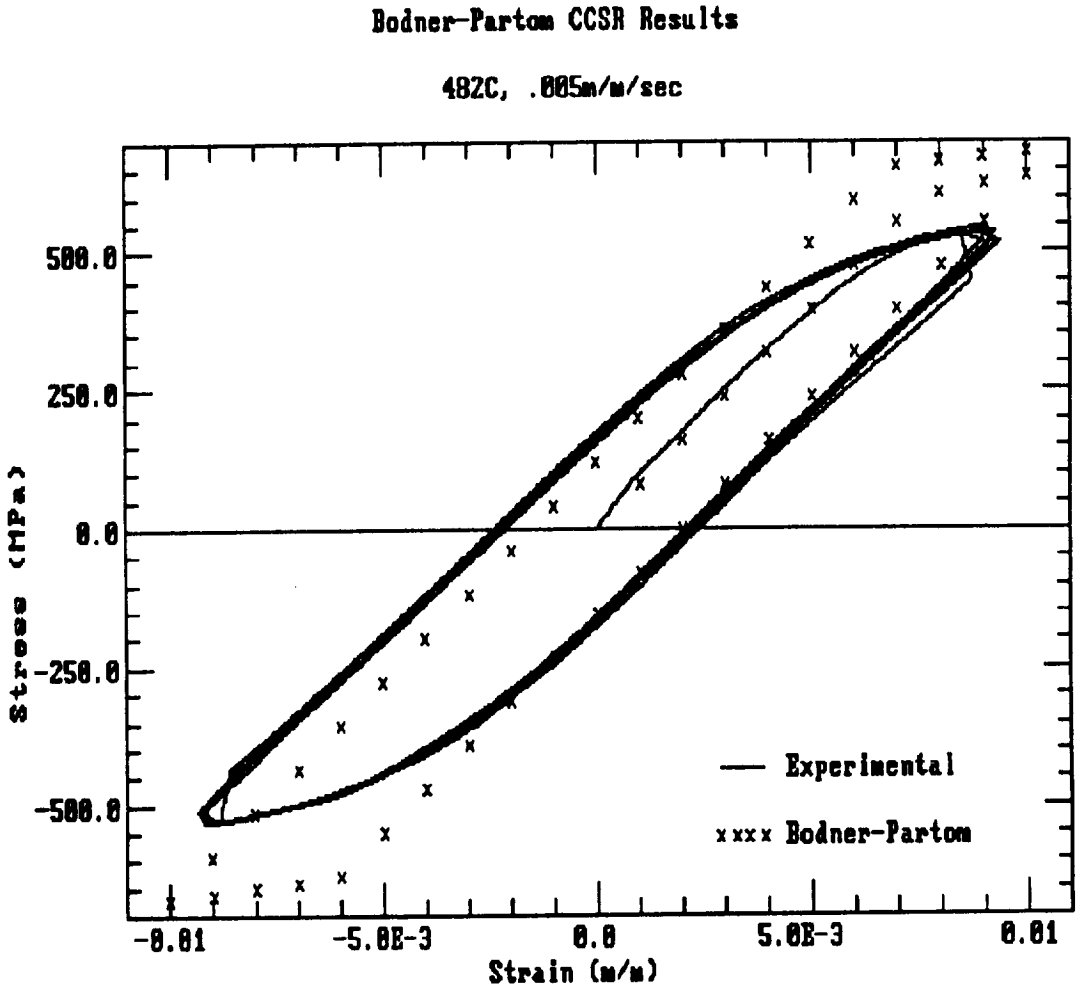

Figure B.25 Bodner-Partom model prediction vs experimental results for Ti-15-3, CCSR test at 482 C, .005 m/m/sec.

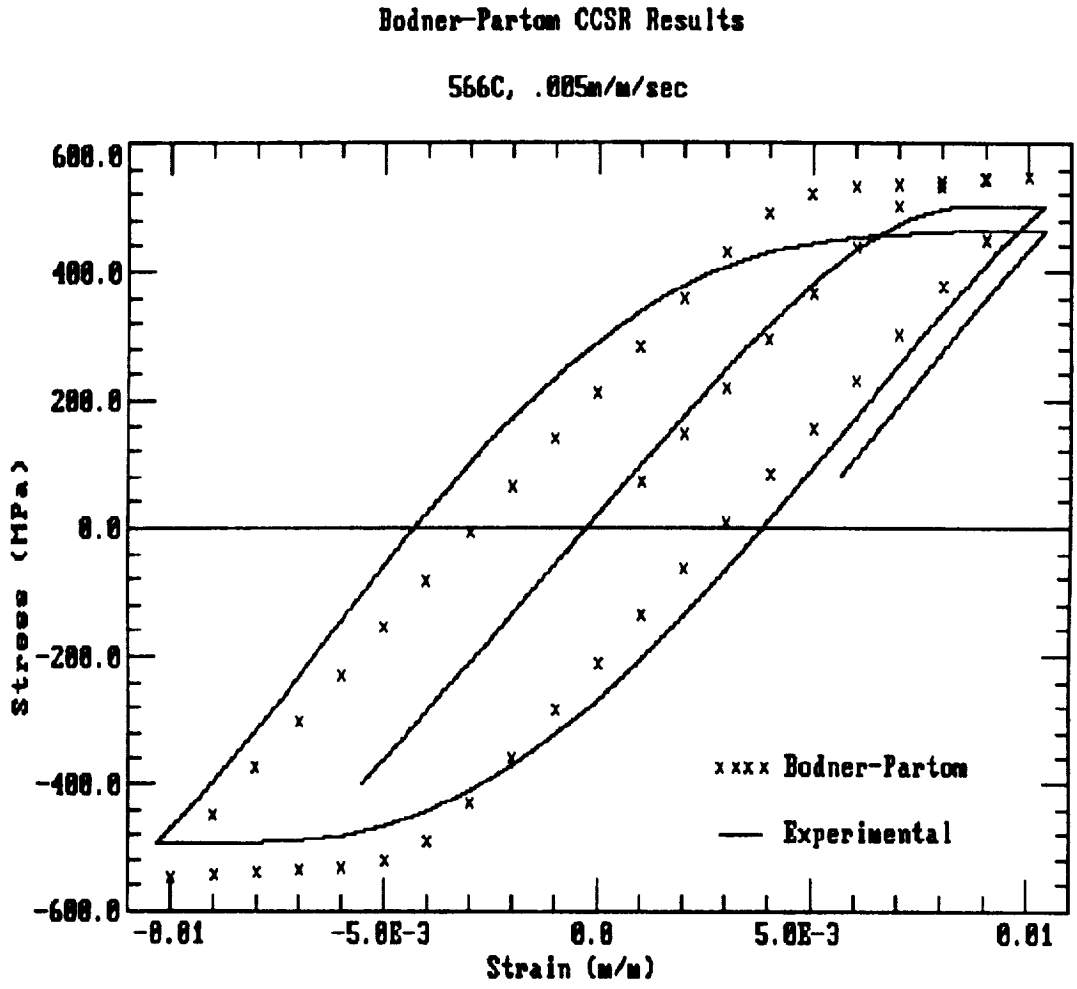

Figure B.26 Bodner-Partom model prediction vs experimental results for Ti-15-3, CCSR test at 566 C, .005 m/m/sec.

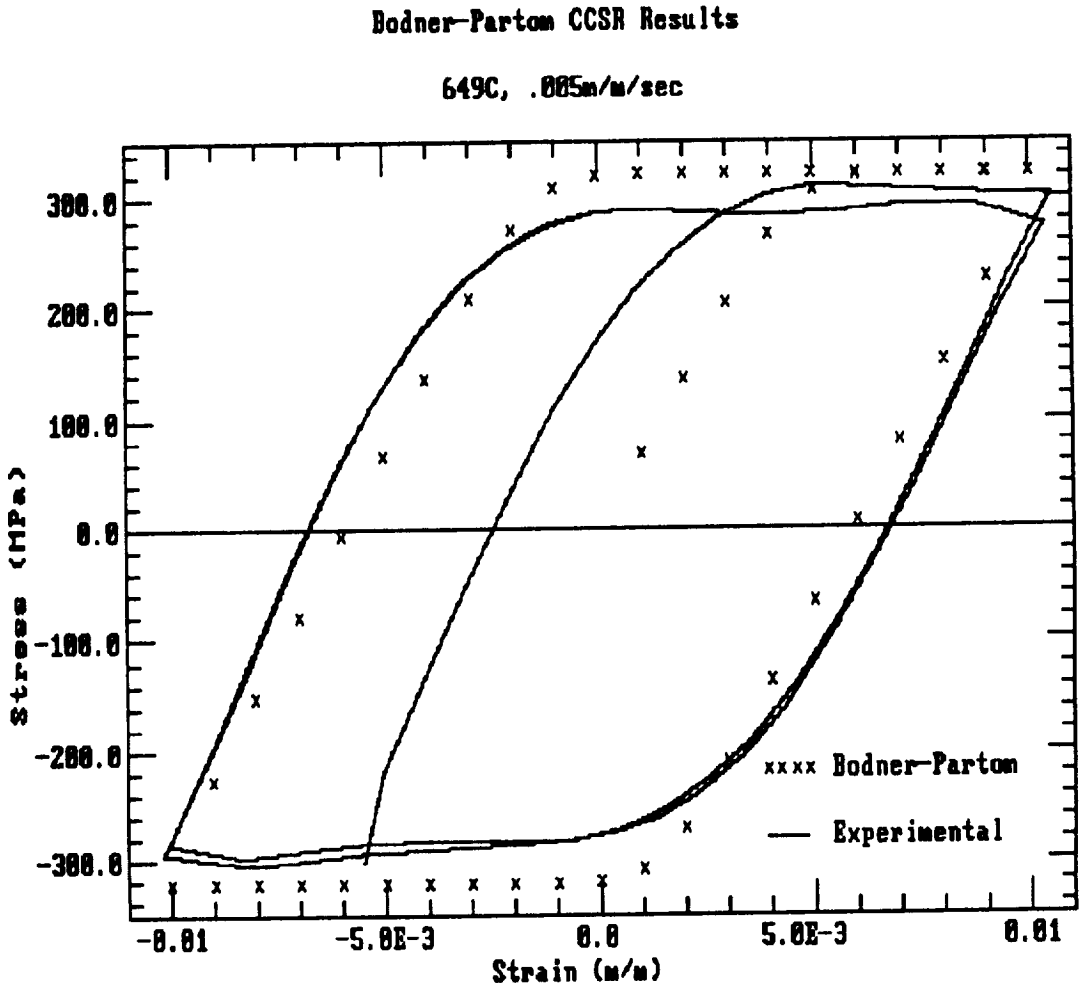

Figure B.27 Bodner-Partom model prediction vs experimental results for Ti-15-3, CCSR test at 649 C, .005 m/m/sec.

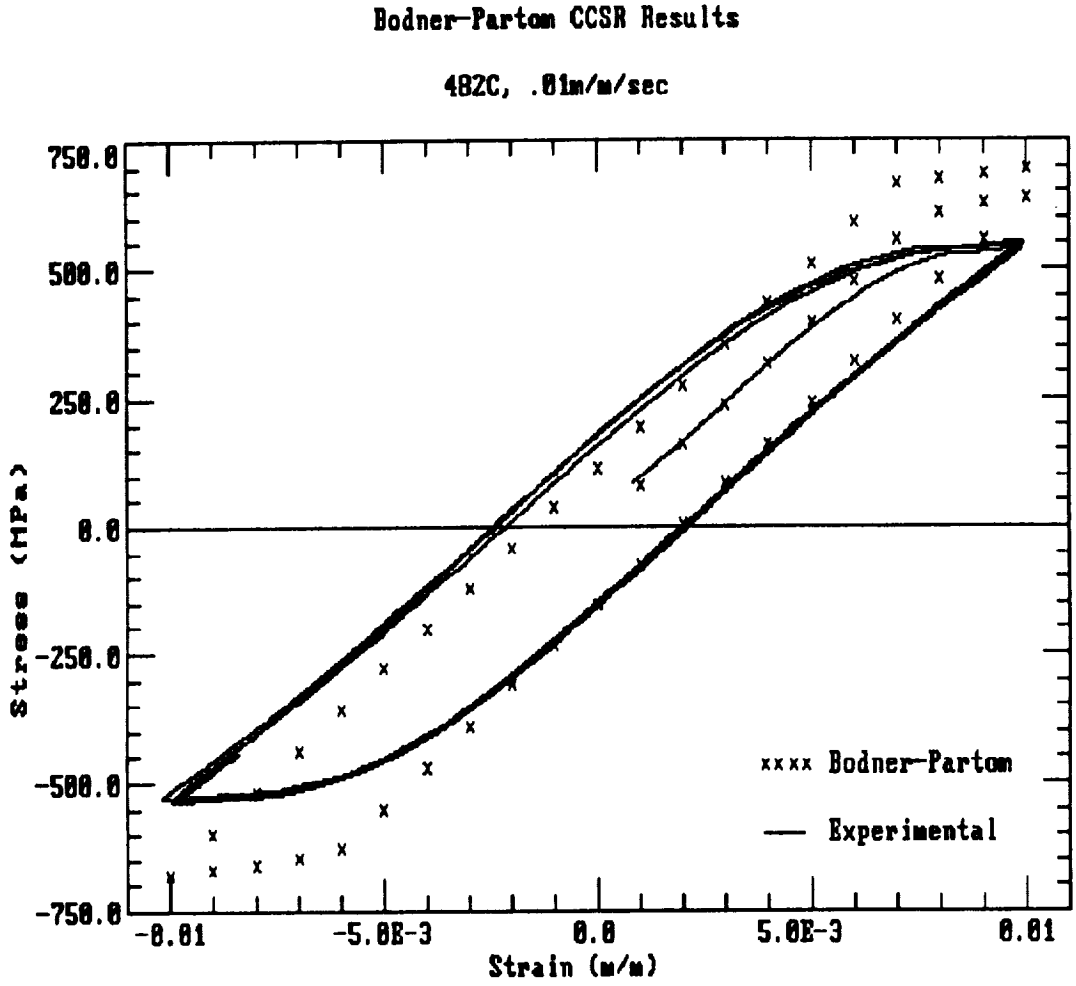

Figure B.28 Bodner-Partom model prediction vs experimental results for Ti-15-3, CCSR test at 482 C, .01 m/m/sec.

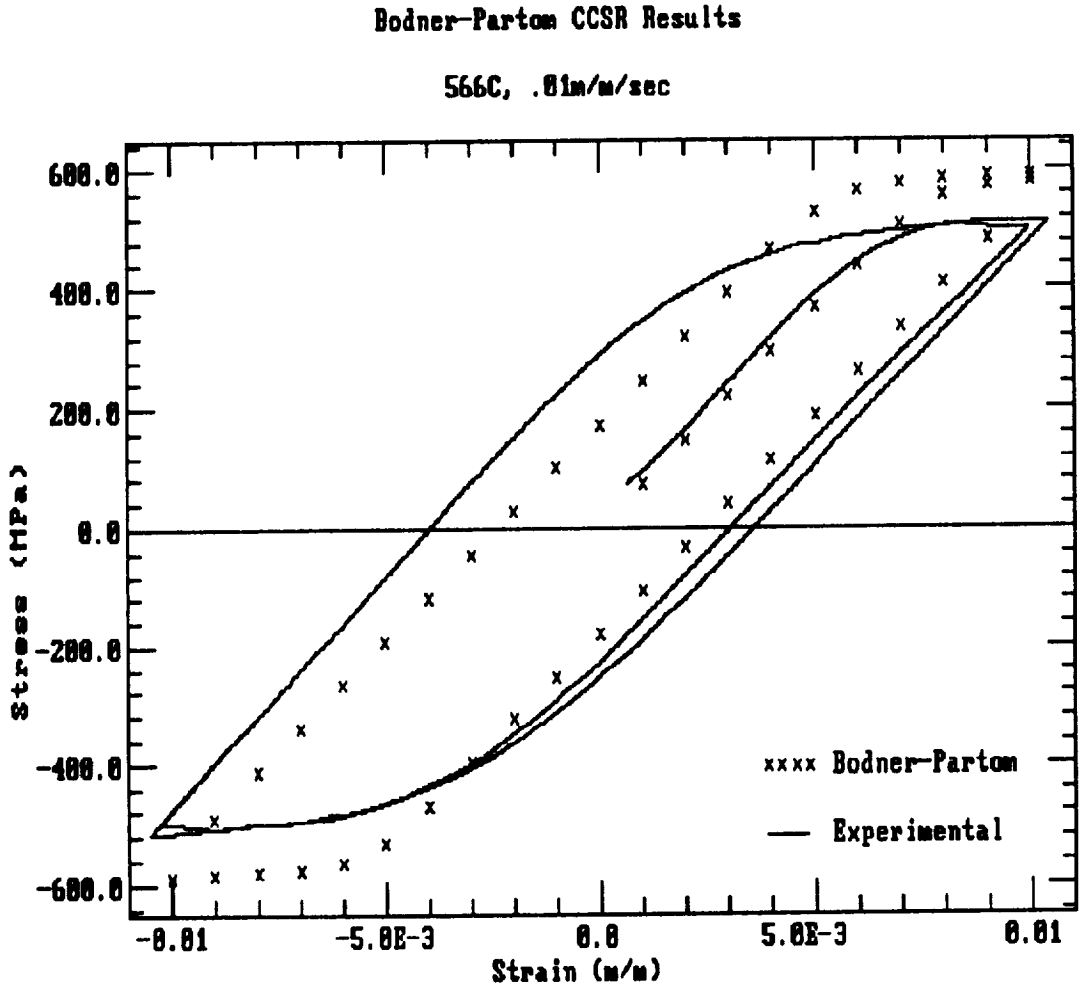

Figure B.29 Bodner-Partom model prediction vs experimental results for Ti-15-3, CCSR test at 566 C, .01 m/m/sec.

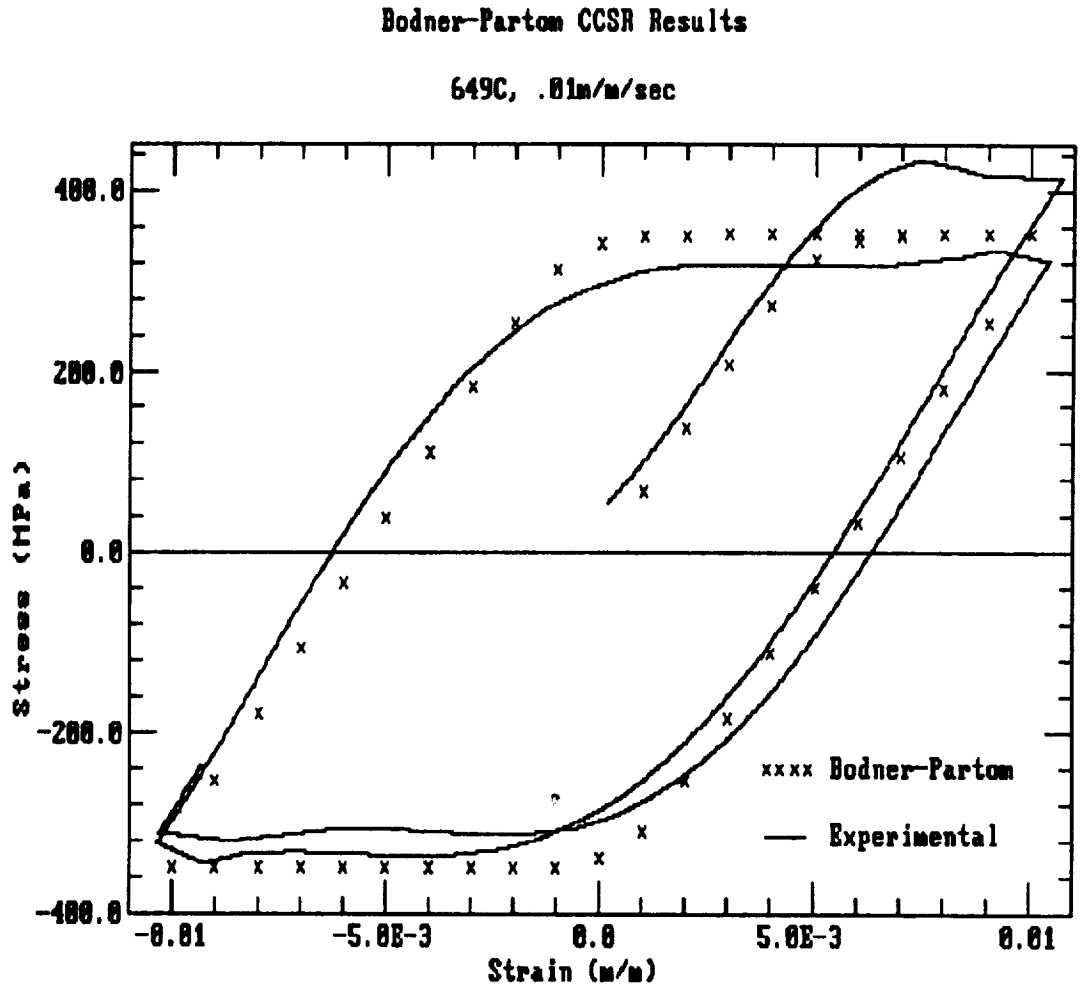

Figure B.30 Bodner-Partom model prediction vs experimental results for Ti-15-3, CCSR test at 649 C, .01 m/m/sec.

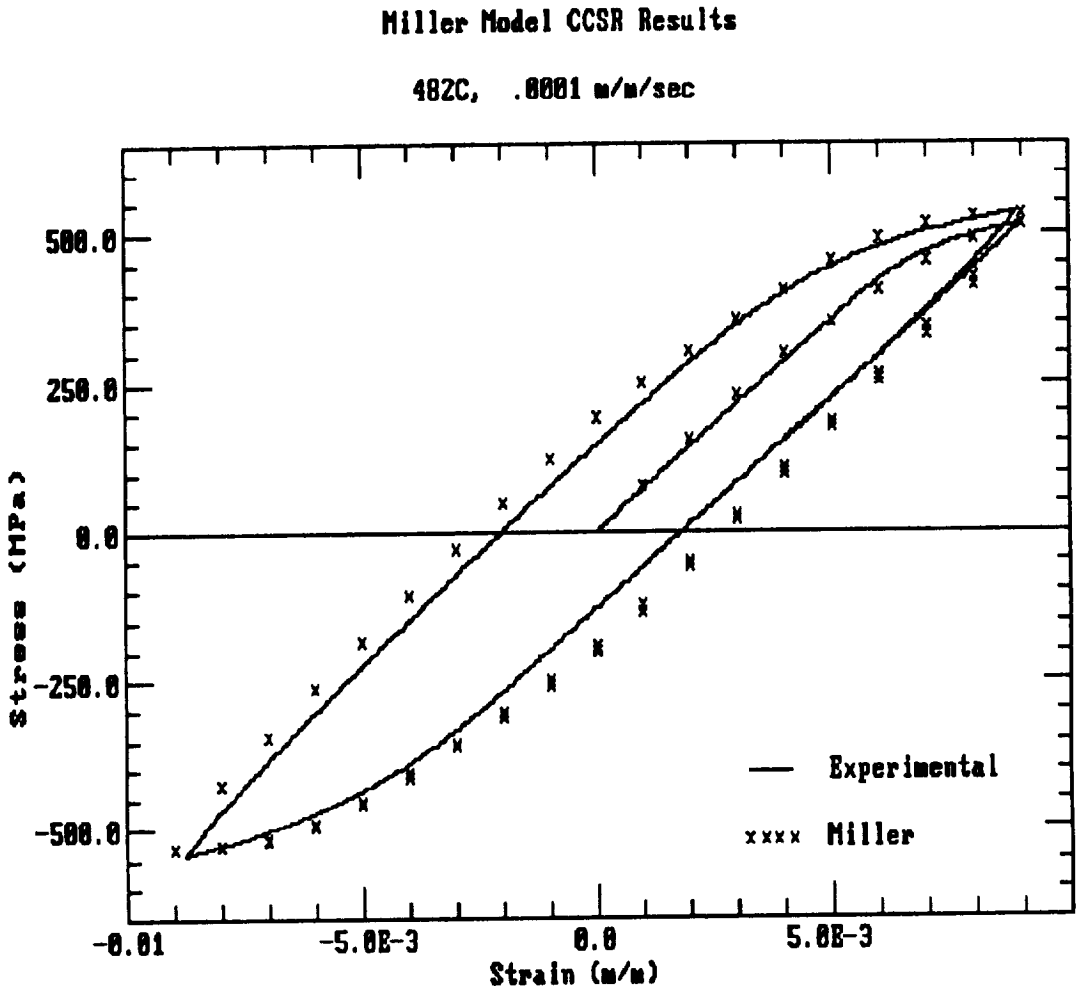

Figure B.31 Miller model prediction vs experimental results for Ti-15-3, CCSR test at 482 C, .0001 m/m/sec.

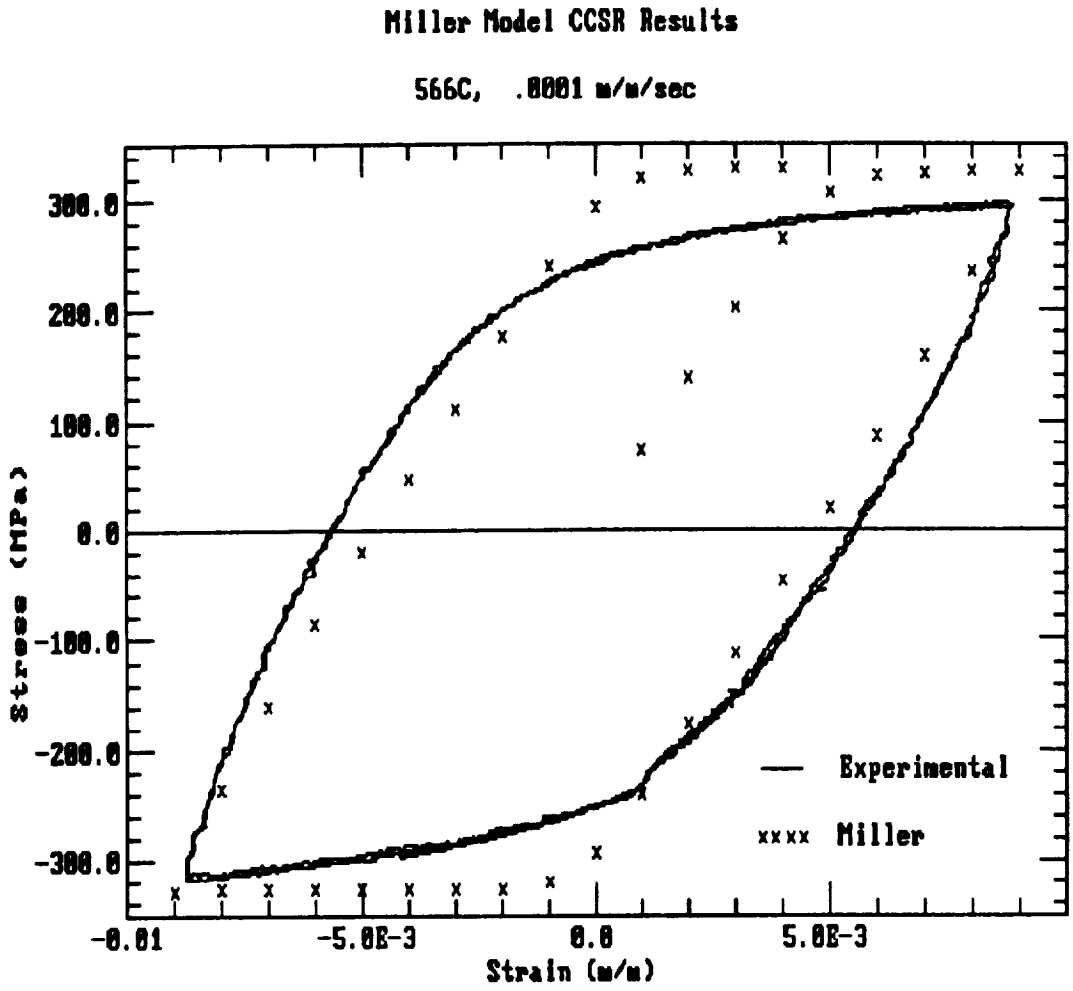

Figure B.32 Miller model prediction vs experimental results for Ti-15-3, CCSR test at 566 C, .0001 m/m/sec.

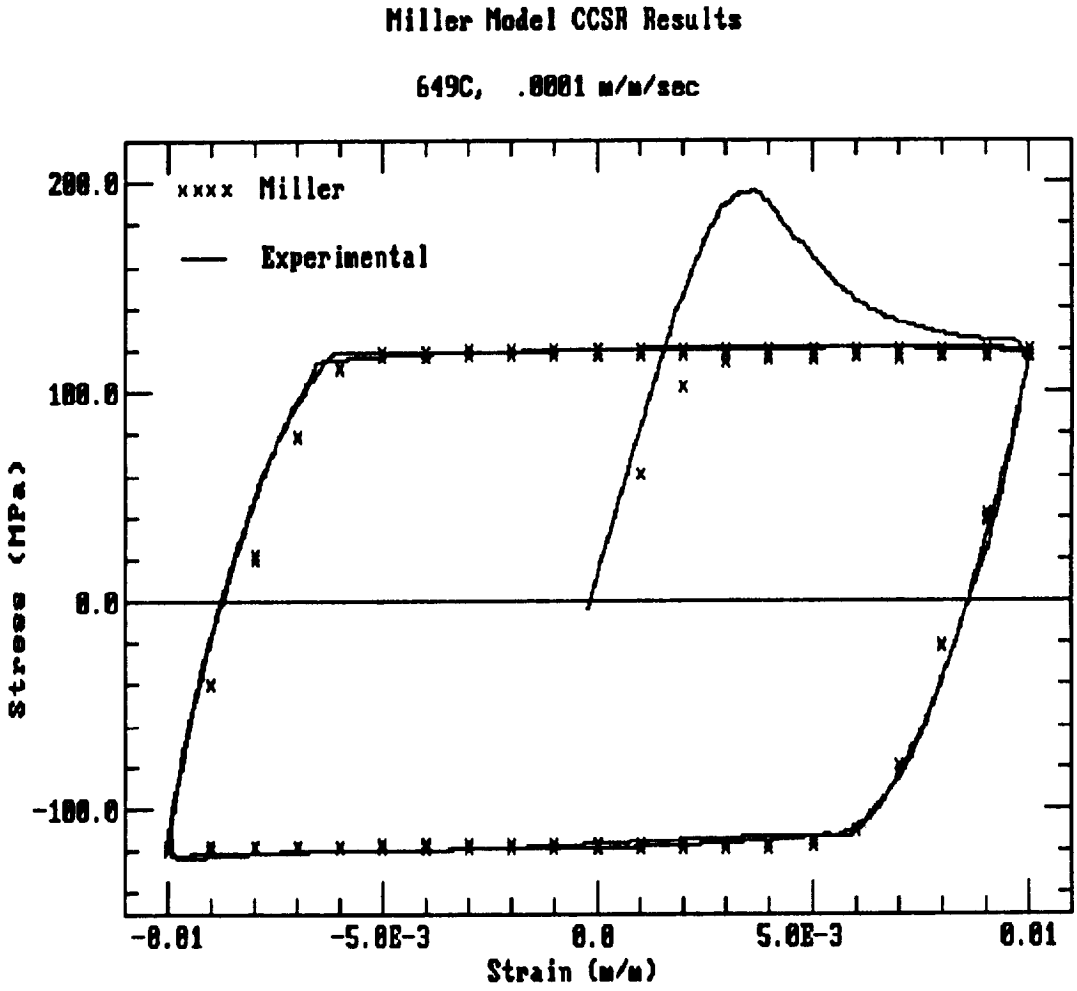

Figure B.33 Miller model prediction vs experimental results for Ti-15-3, CCSR test at 649 C, .0001 m/m/sec.

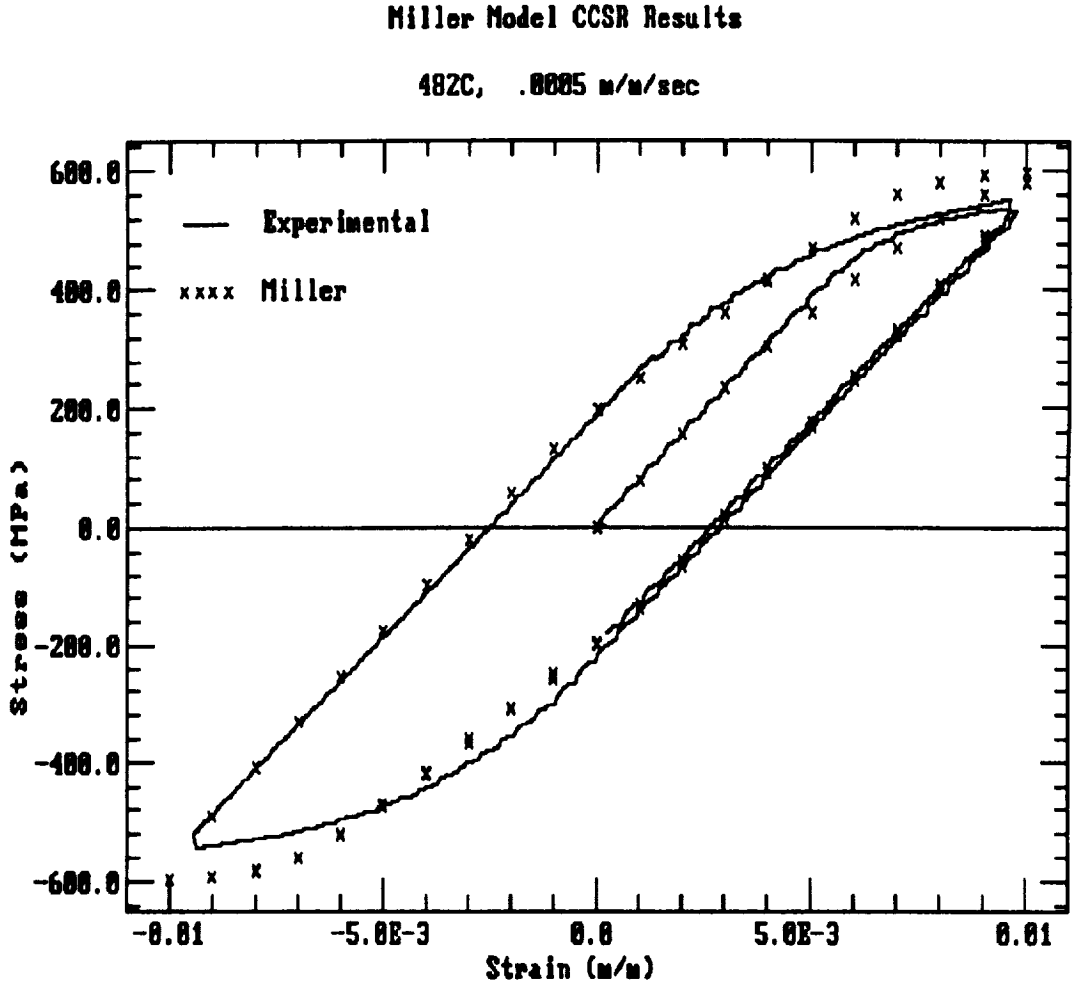

Figure B.34 Miller model prediction vs experimental results for Ti-15-3, CCSR test at 482 C, .0005 m/m/sec.

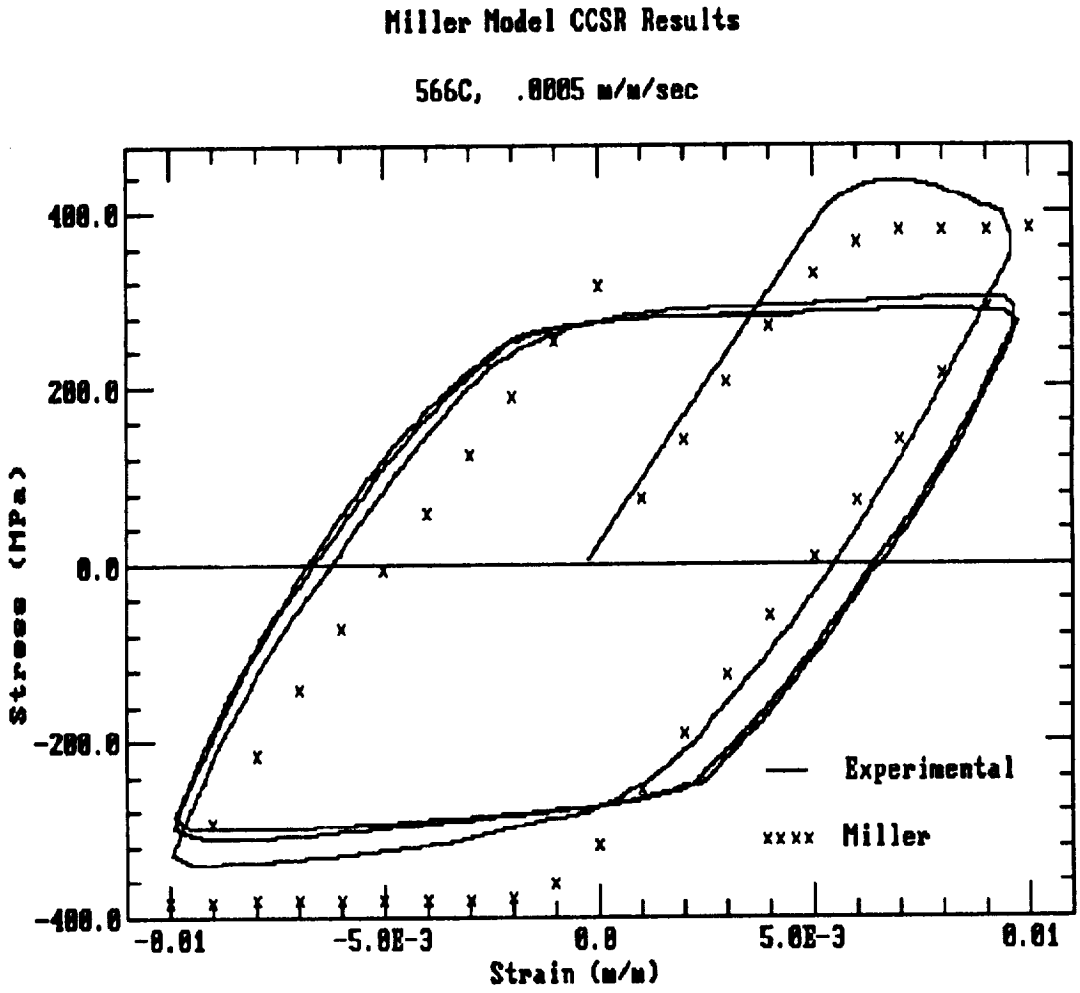

Figure B.35 Miller model prediction vs experimental results for Ti-15-3, CCSR test at 566 C, .0005 m/m/sec.

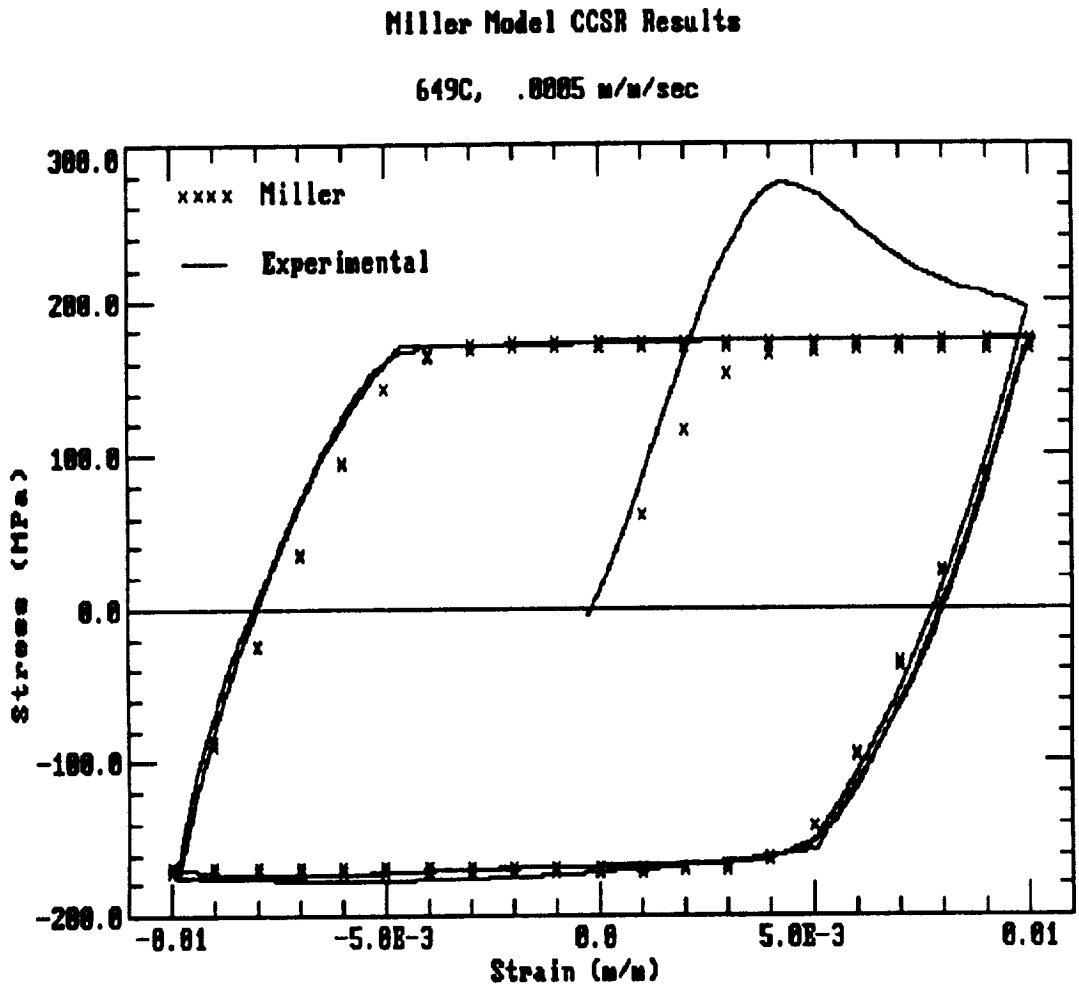

Figure B.36 Miller model prediction vs experimental results for Ti-15-3, CCSR test at 649 C, .0005 m/m/sec.

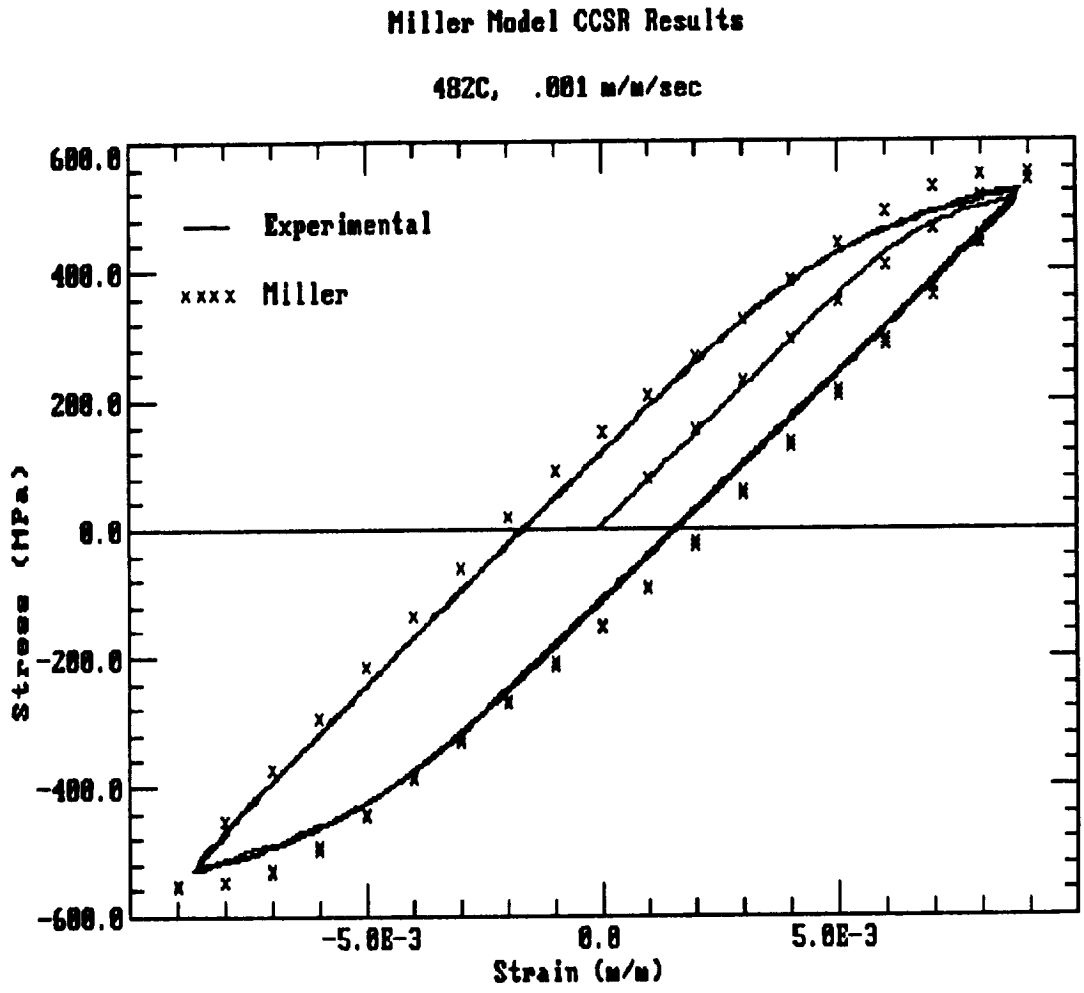

Figure B.37 Miller model prediction vs experimental results for Ti-15-3, CCSR test at 482 C, .001 m/m/sec.

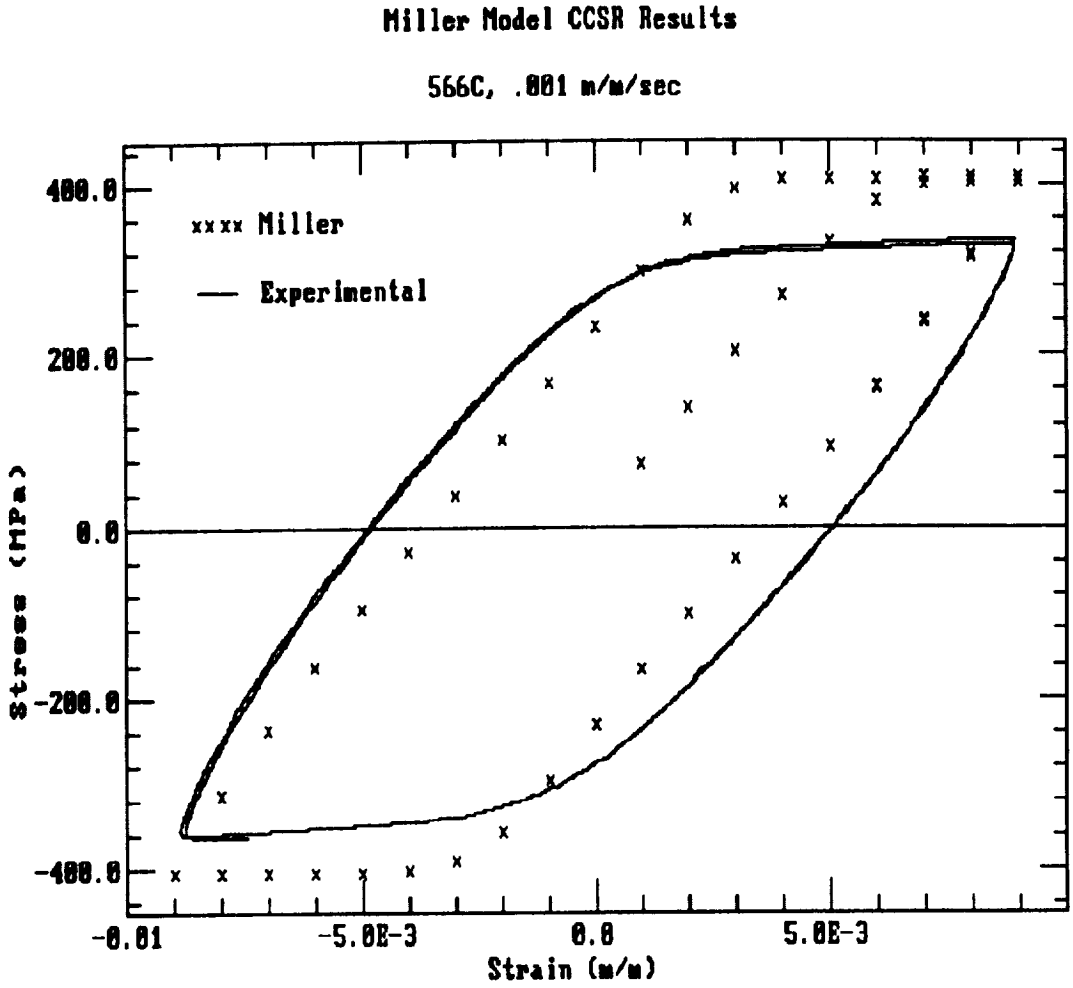

Figure B.38 Miller model prediction vs experimental results for Ti-15-3, CCSR test at 566 C, .001 m/m/sec.

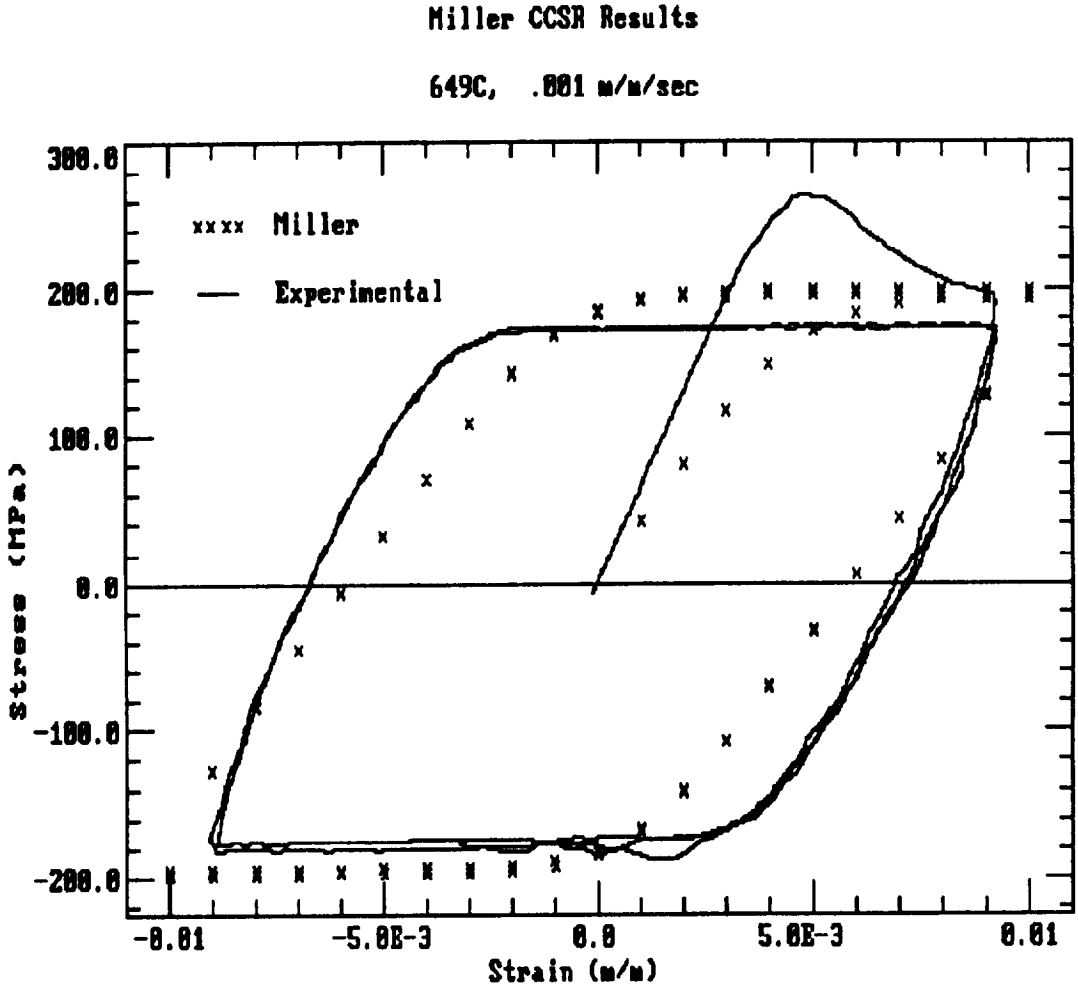

Figure B.39 Miller model prediction vs experimental results for Ti-15-3, CCSR test at 649 C, .001 m/m/sec.

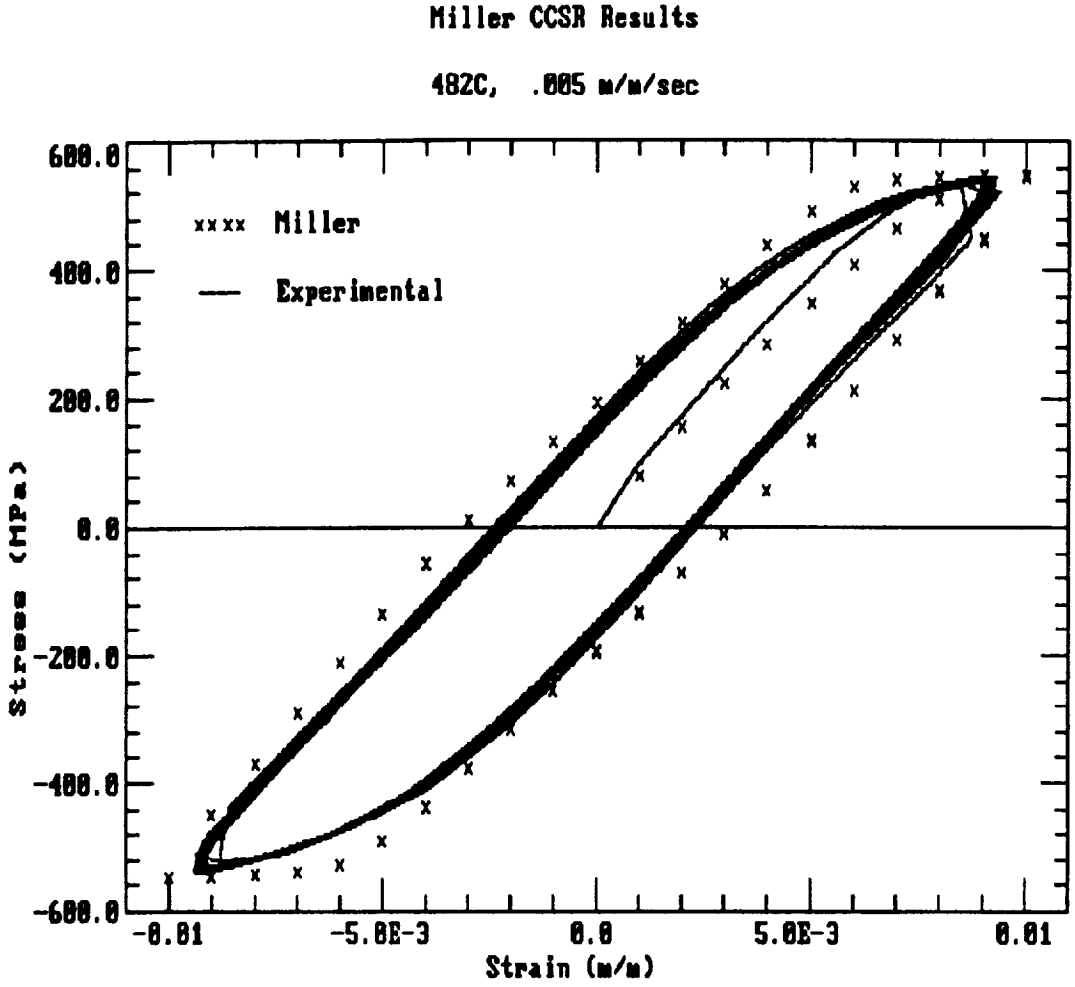

Figure B.40 Miller model prediction vs experimental results for Ti-15-3, CCSR test at 482 C, .005 m/m/sec.

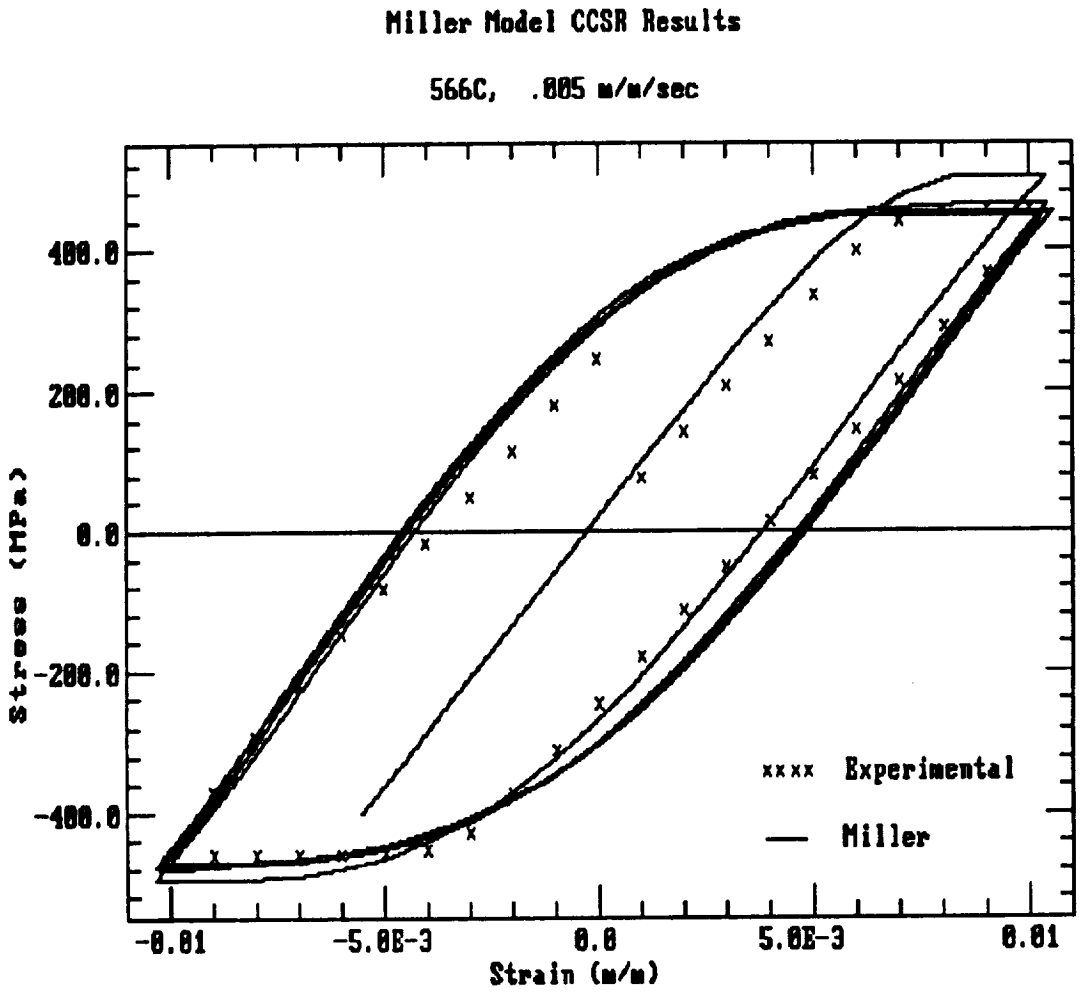

Figure B.41 Miller model prediction vs experimental results for Ti-15-3, CCSR test at 566 C, .005 m/m/sec.

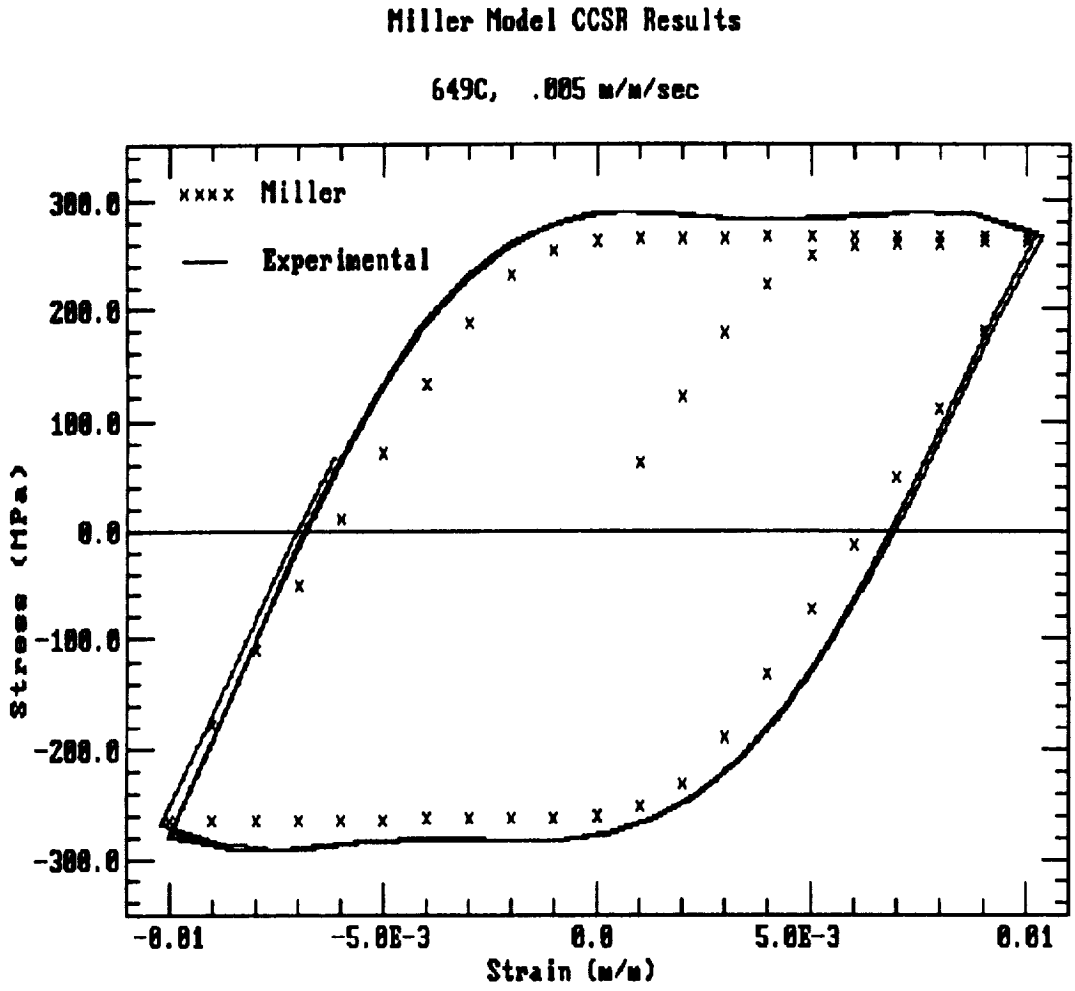

Figure B.42 Miller model prediction vs experimental results for Ti-15-3, CCSR test at 649 C, .005 m/m/sec.

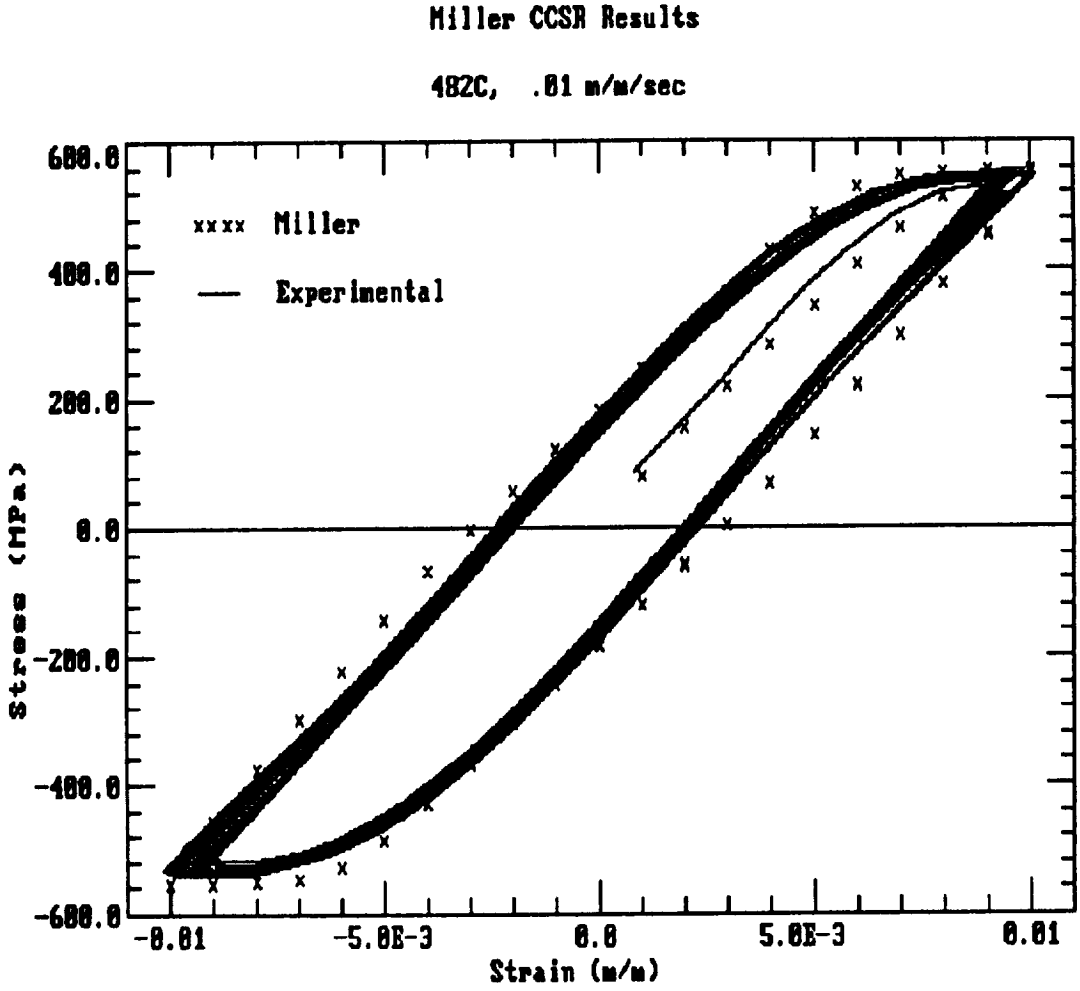

Figure B.43 Miller model prediction vs experimental results for Ti-15-3, CCSR test at 482 C, .01 m/m/sec.

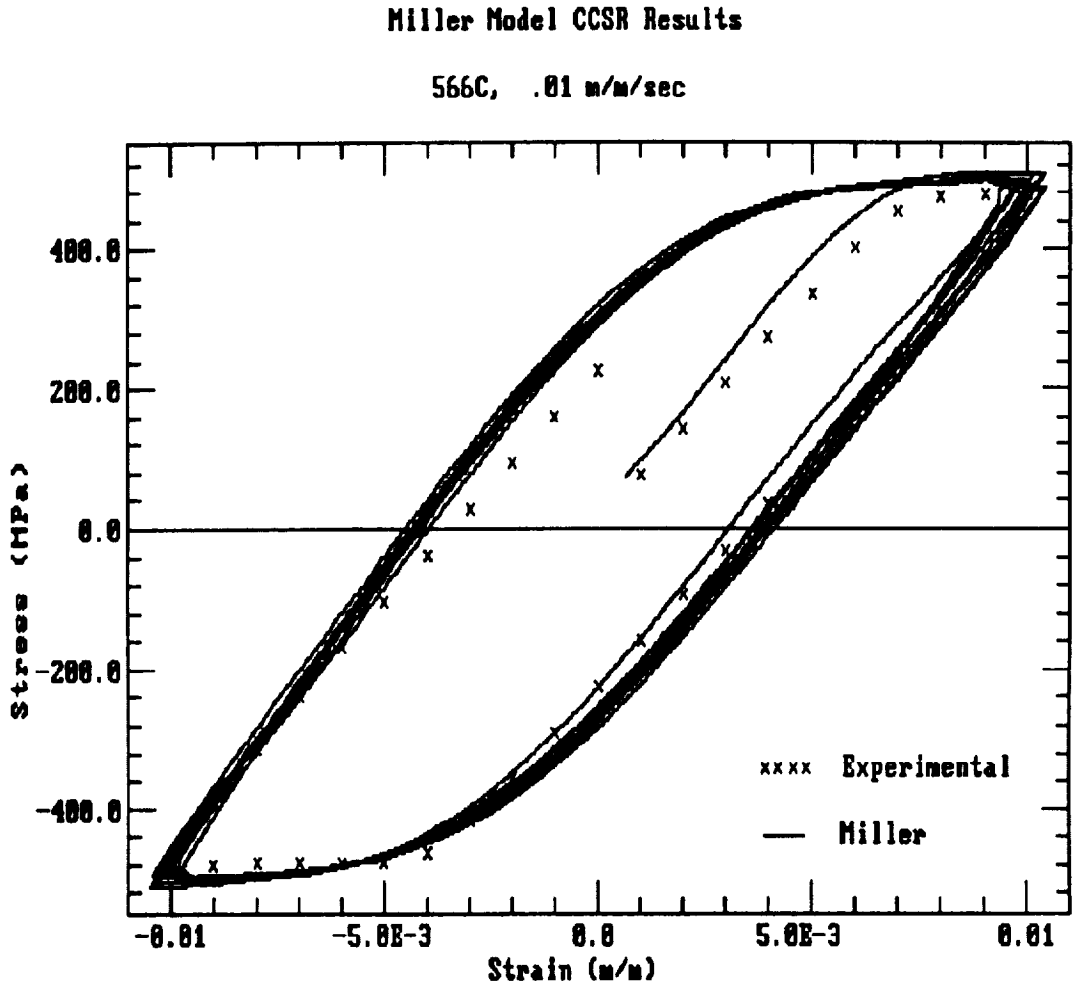

Figure B.44 Miller model prediction vs experimental results for Ti-15-3, CCSR test at 566 C, .01 m/m/sec.

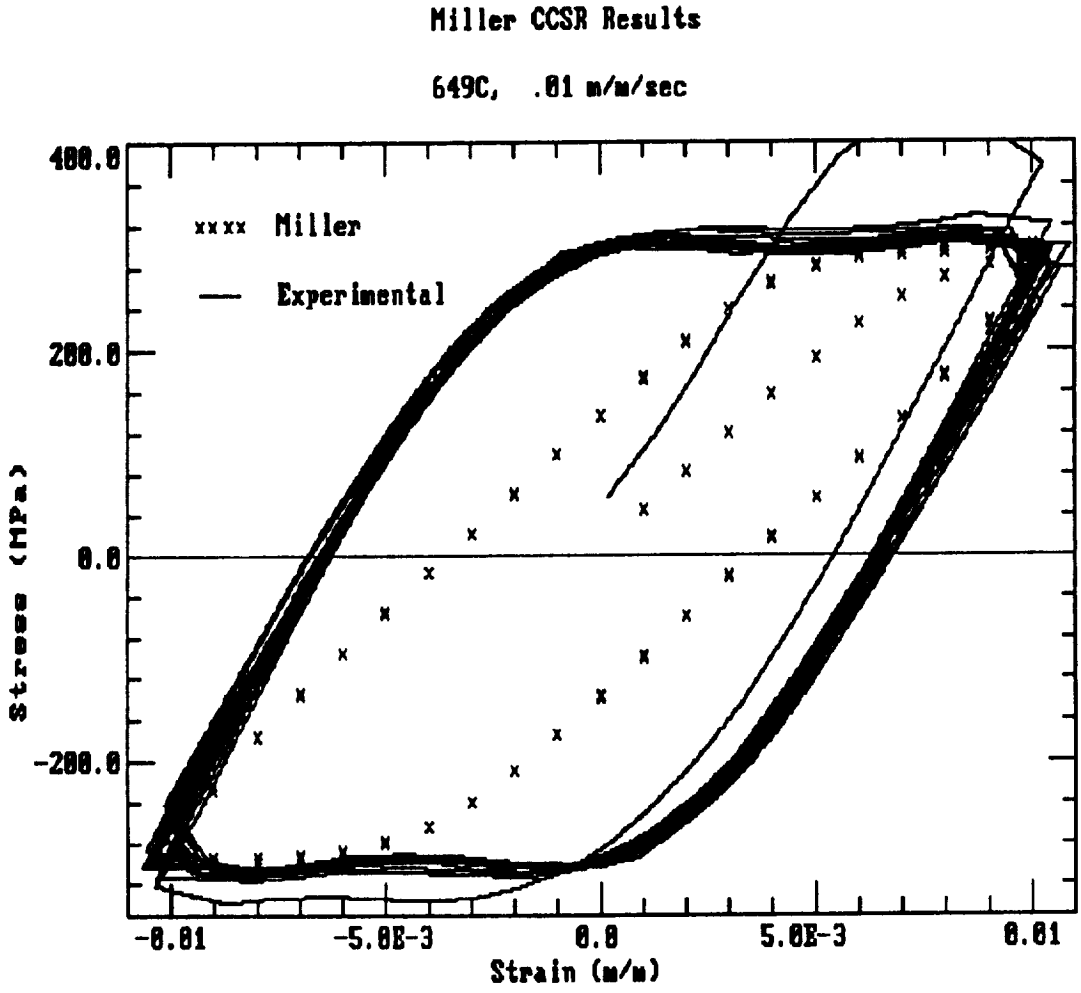

Figure B.45 Miller model prediction vs experimental results for Ti-15-3, CCSR test at 649 C, .01 m/m/sec.

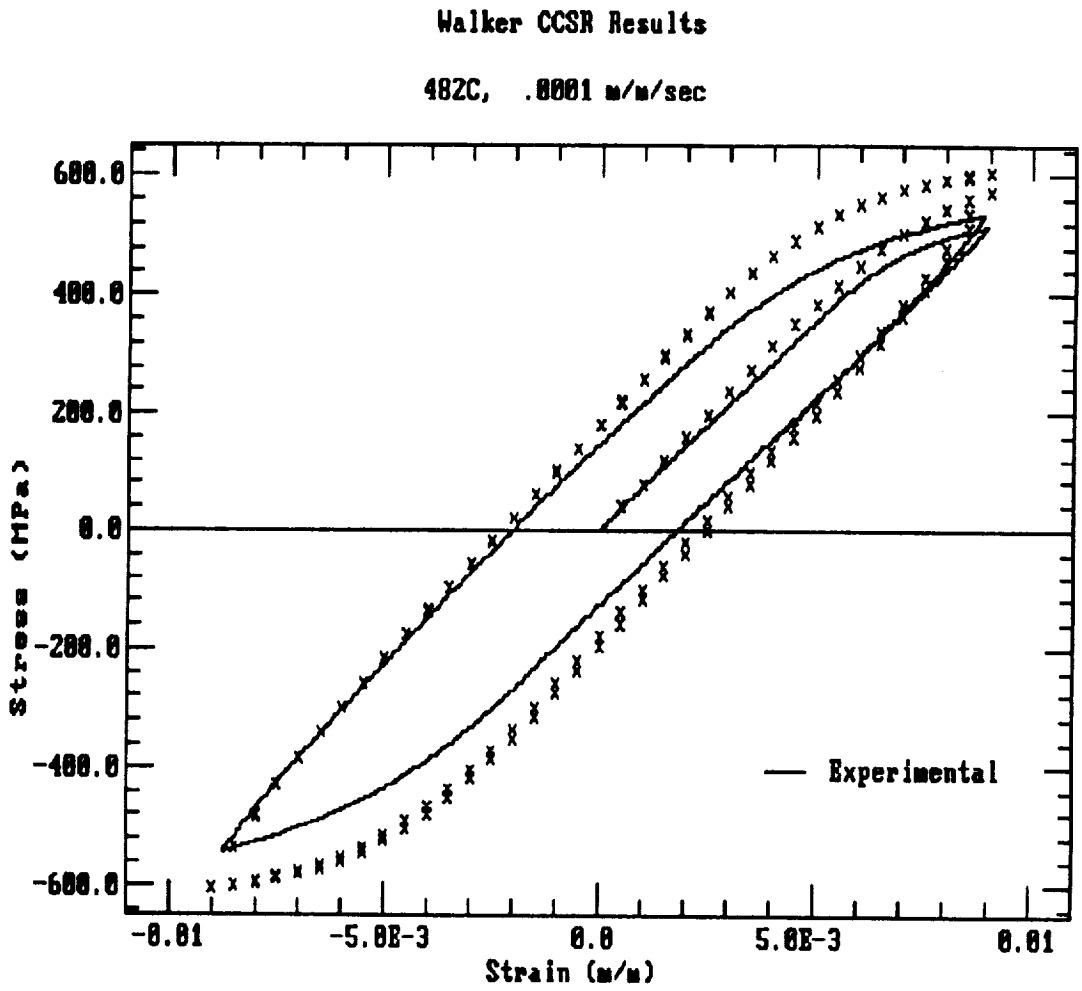

Figure B.46 Walker model prediction vs experimental results for Ti-15-3, CCSR test at 482 C, .0001 m/m/sec.

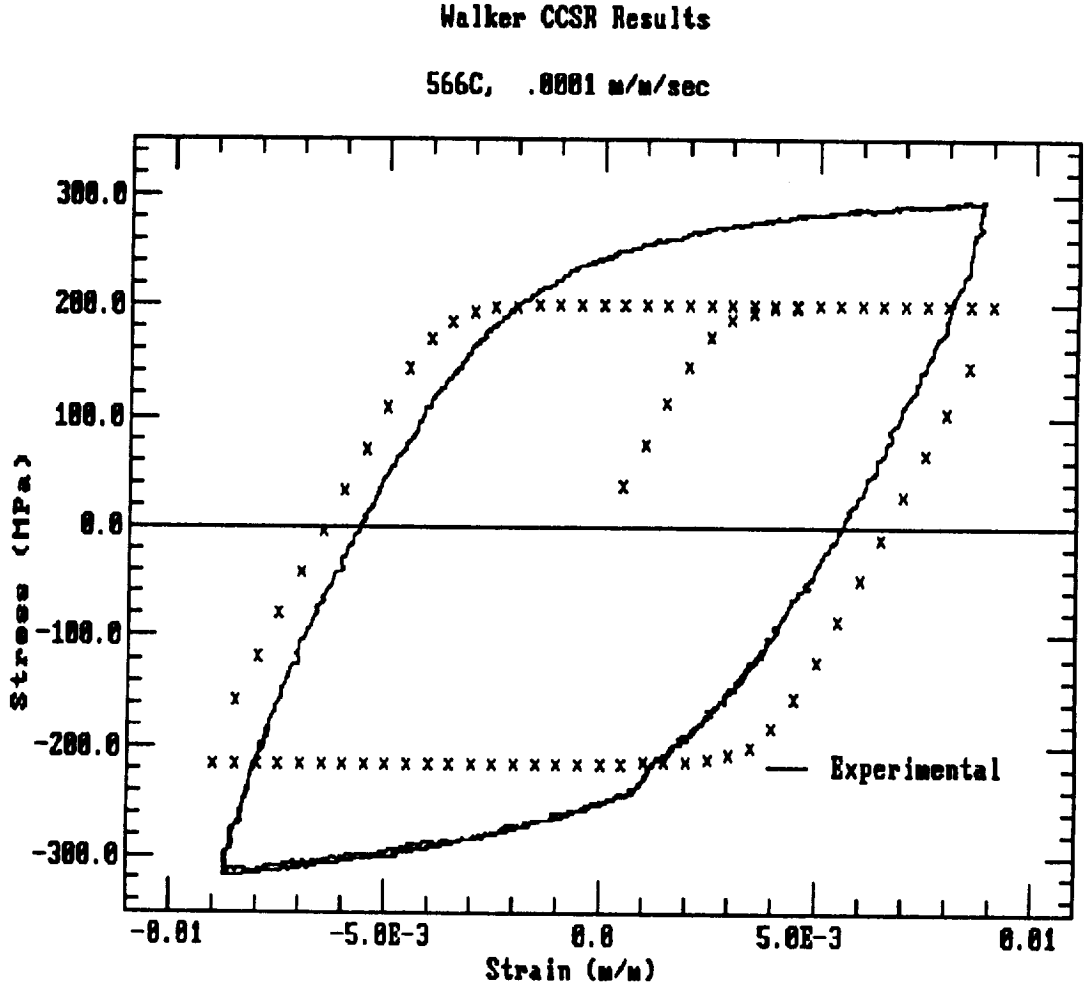

Figure B.47 Walker model prediction vs experimental results for Ti-15-3, CCSR test at 566 C, .0001 m/m/sec.

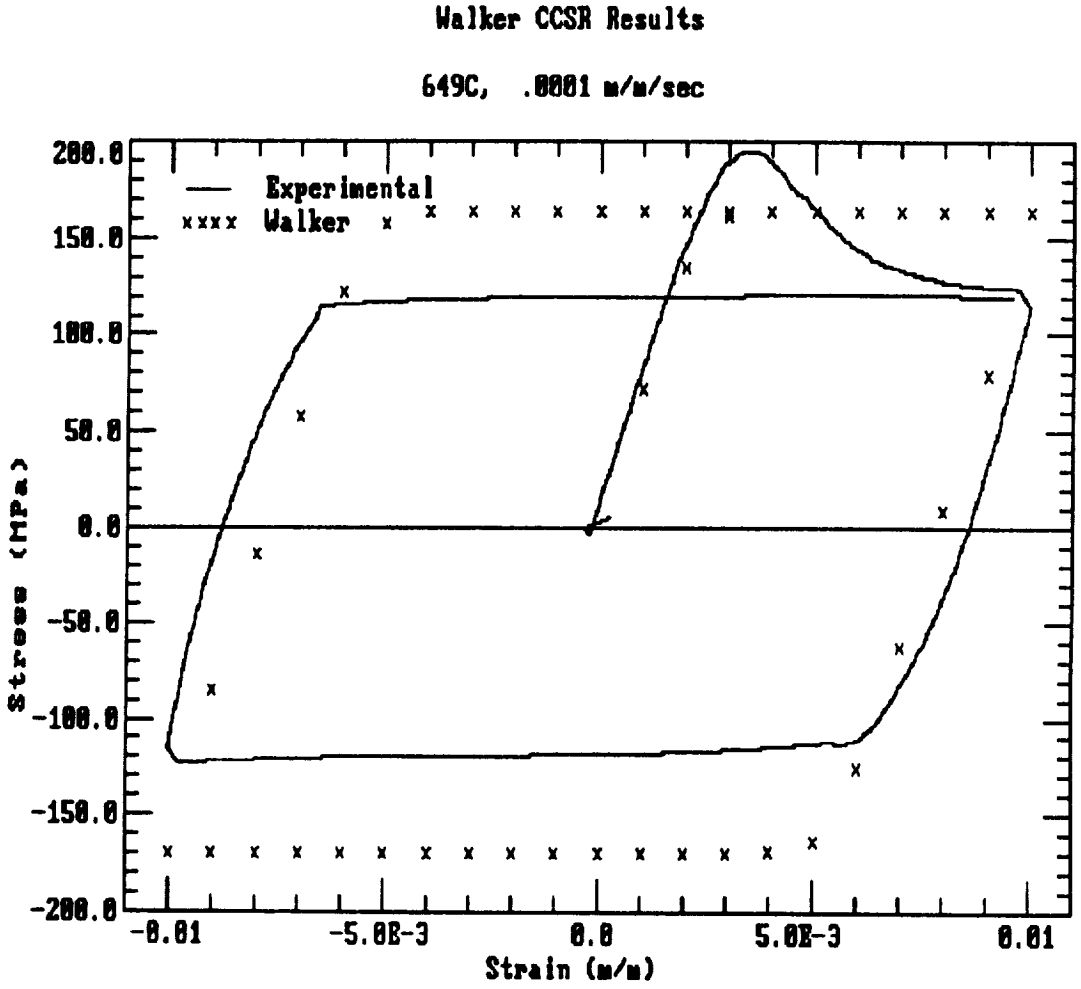

Figure B.48 Walker model prediction vs experimental results for Ti-15-3, CCSR test at 649 C, .0001 m/m/sec.

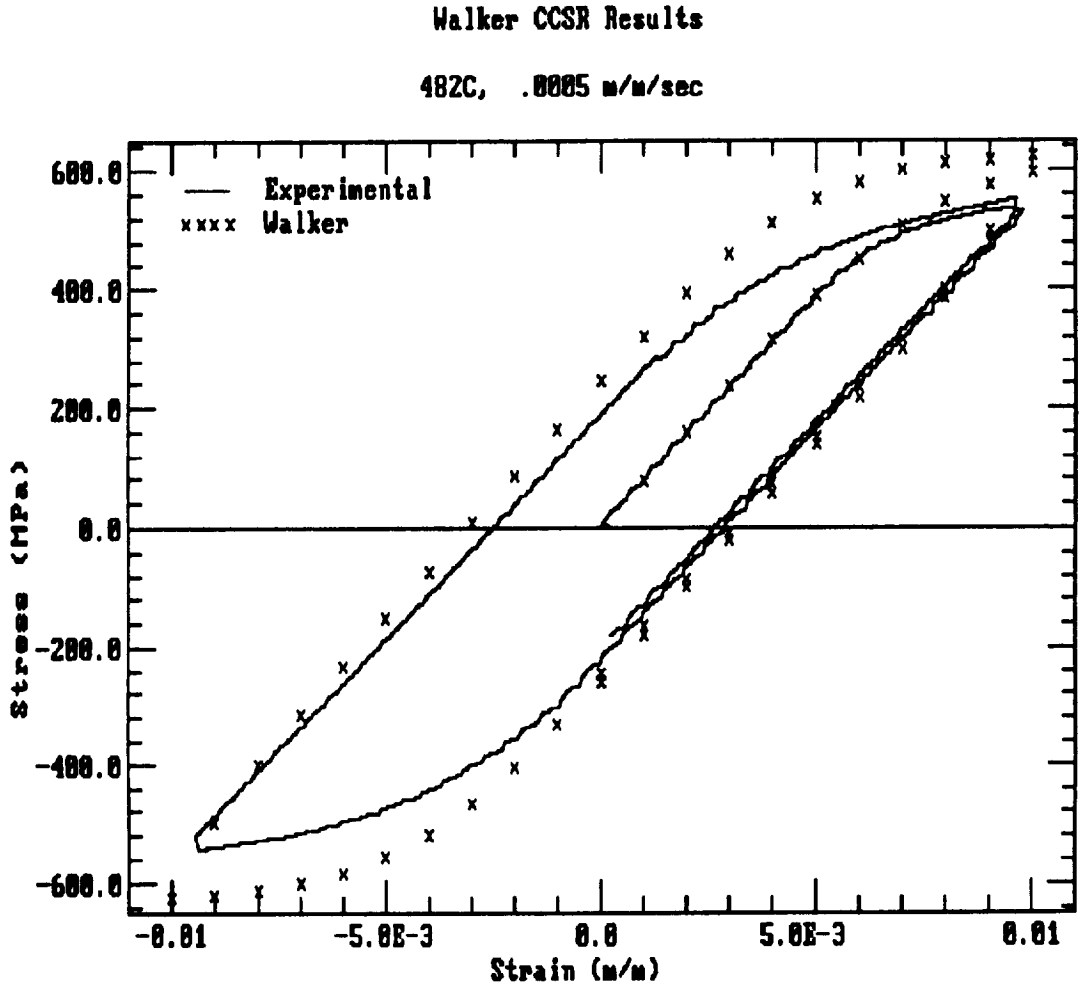

Figure B.49 Walker model prediction vs experimental results for Ti-15-3, CCSR test at 482 C, .0005 m/m/sec.

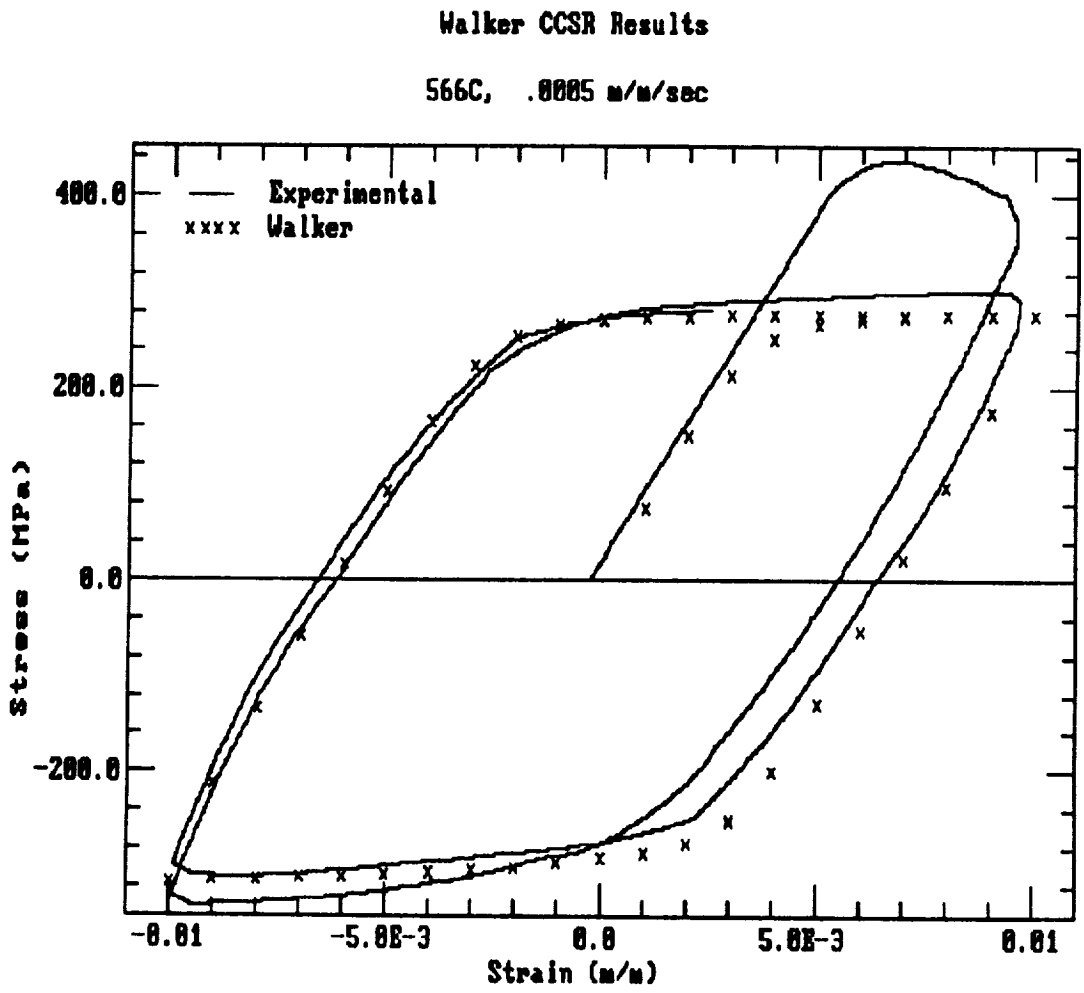

Figure B.50 Walker model prediction vs experimental results for Ti-15-3, CCSR test at 566 C, .0005 m/m/sec.

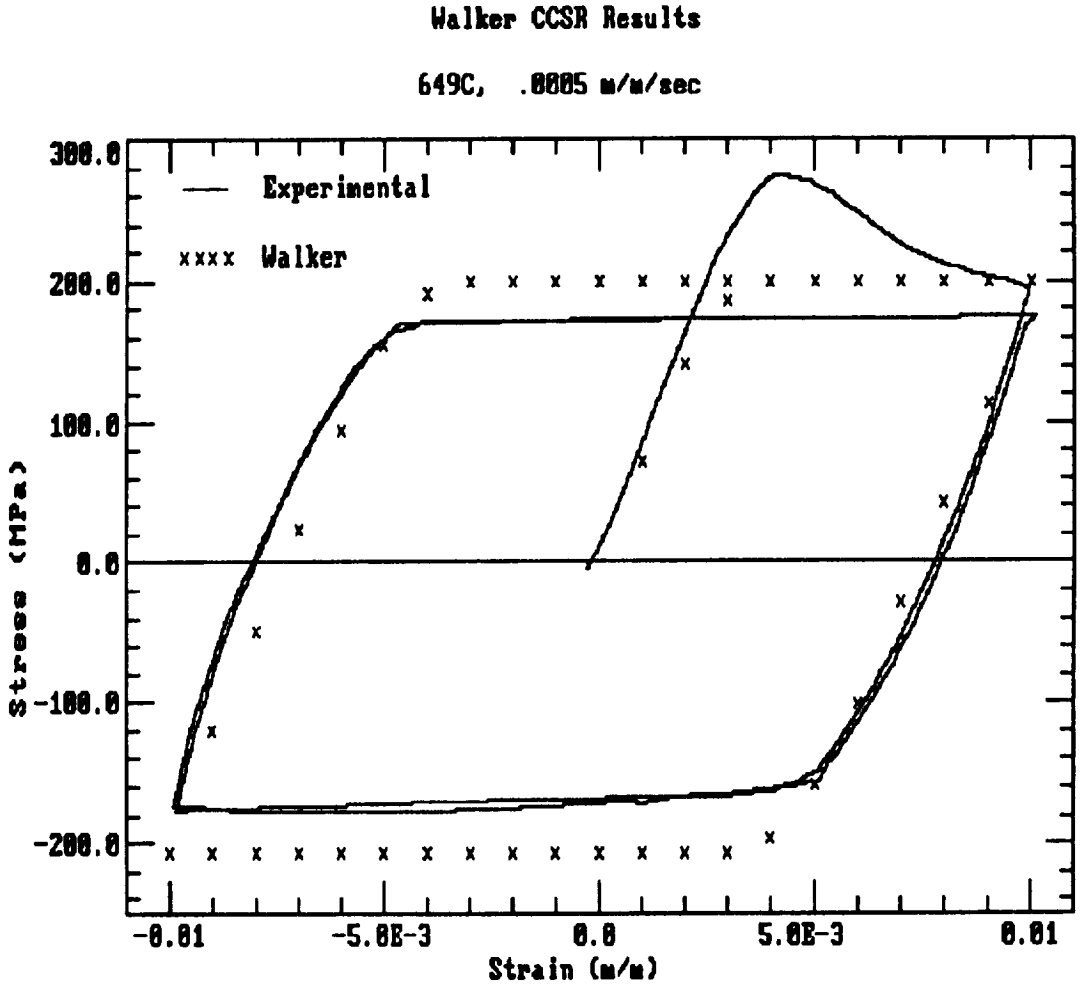

Figure B.51 Walker model prediction vs experimental results for Ti-15-3, CCSR test at 649 C, .0005 m/m/sec.

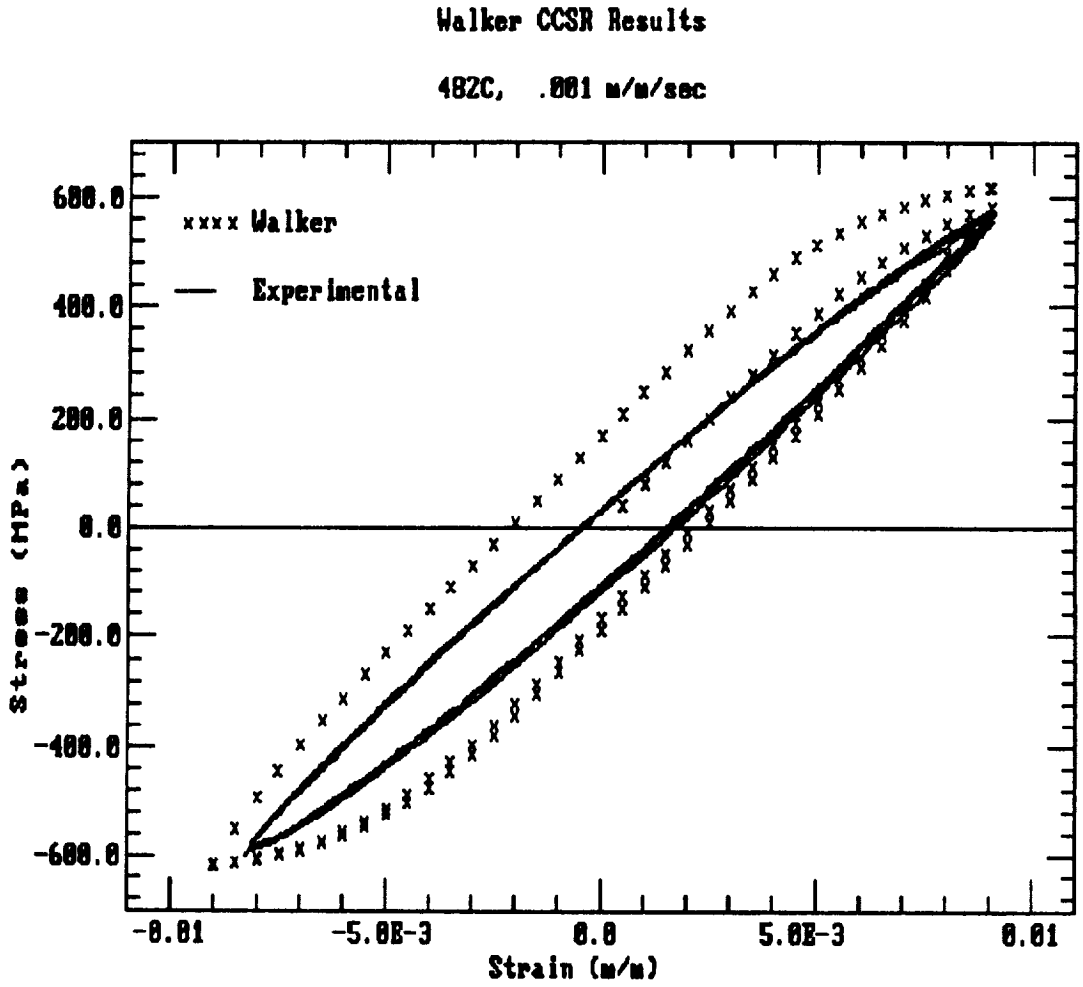

Figure B.52 Walker model prediction vs experimental results for Ti-15-3, CCSR test at 482 C, .001 m/m/sec.

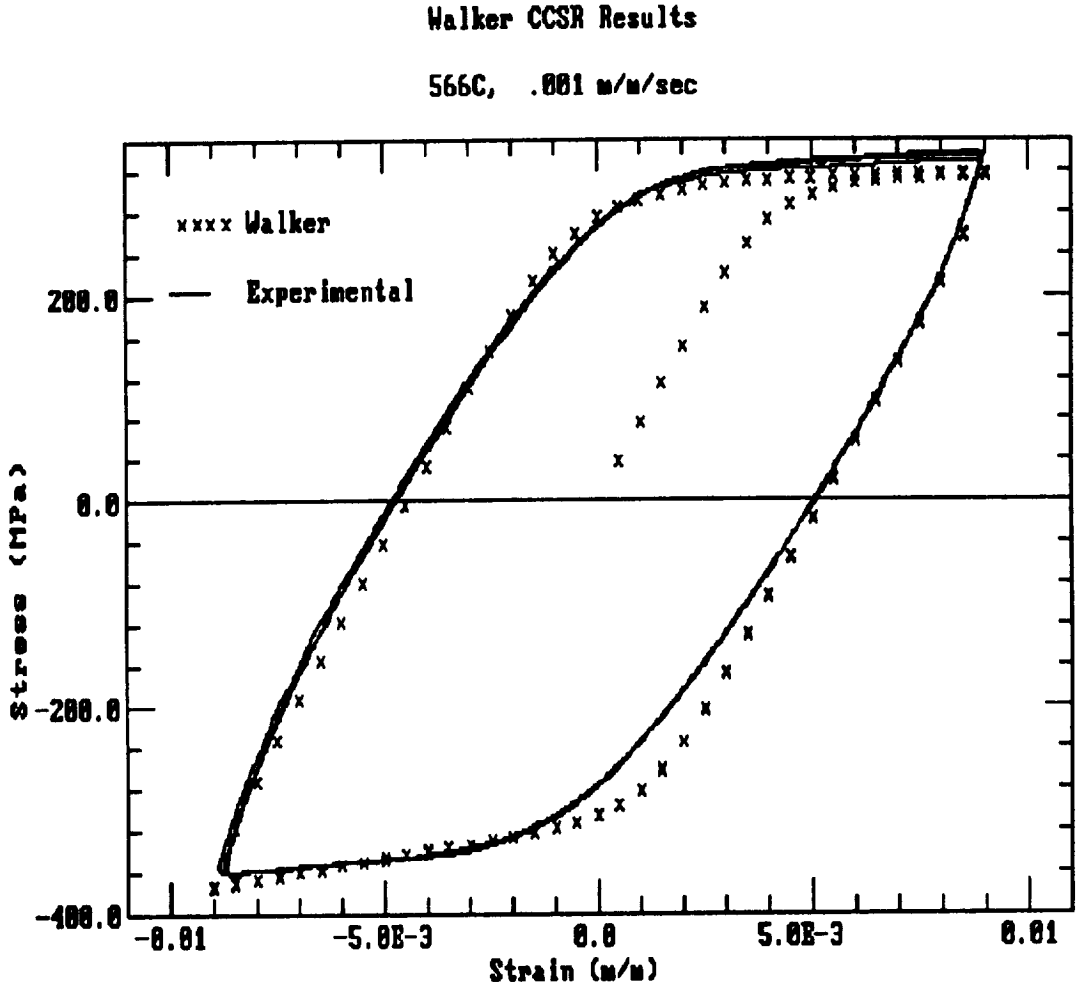

Figure B.53 Walker model prediction vs experimental results for Ti-15-3, CCSR test at 566 C, .001 m/m/sec.

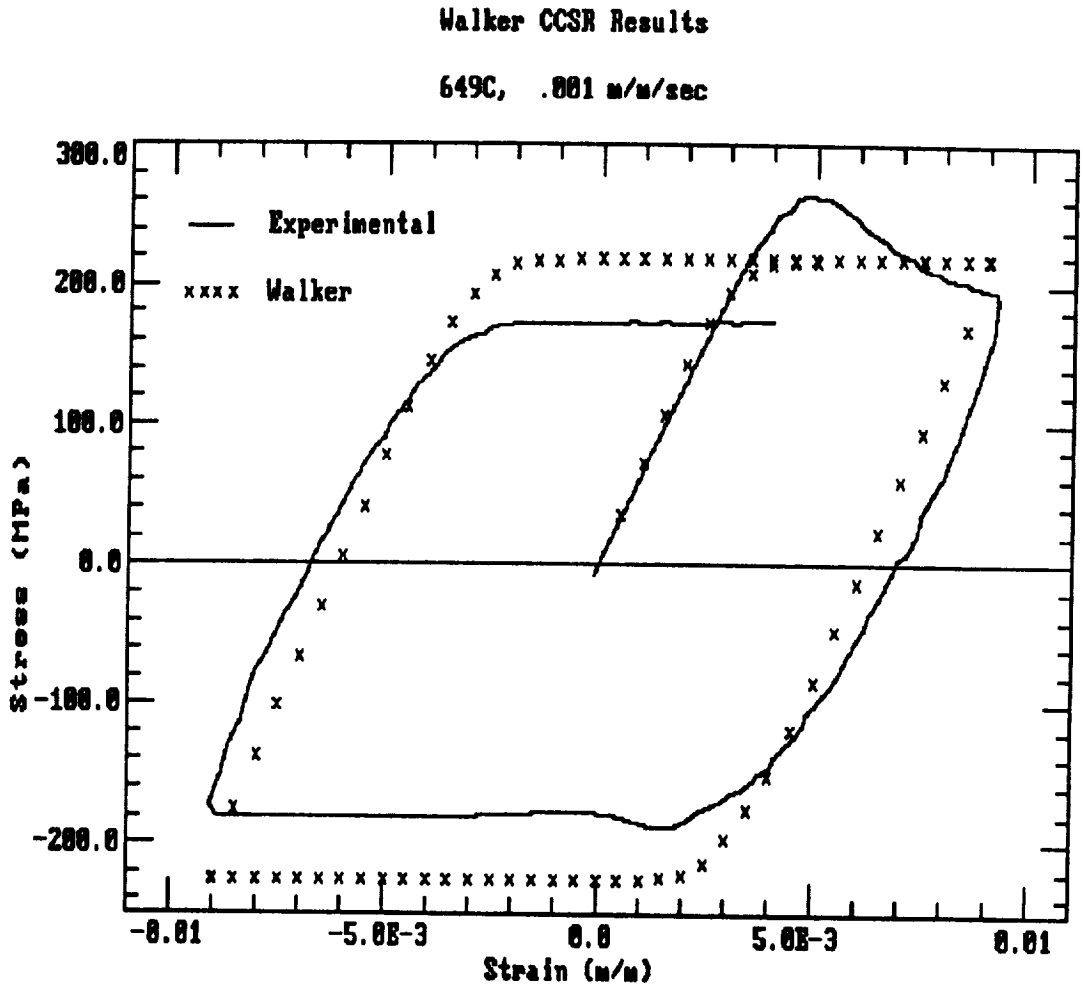

Figure B.54 Walker model prediction vs experimental results for Ti-15-3, CCSR test at 649 C, .001 m/m/sec.

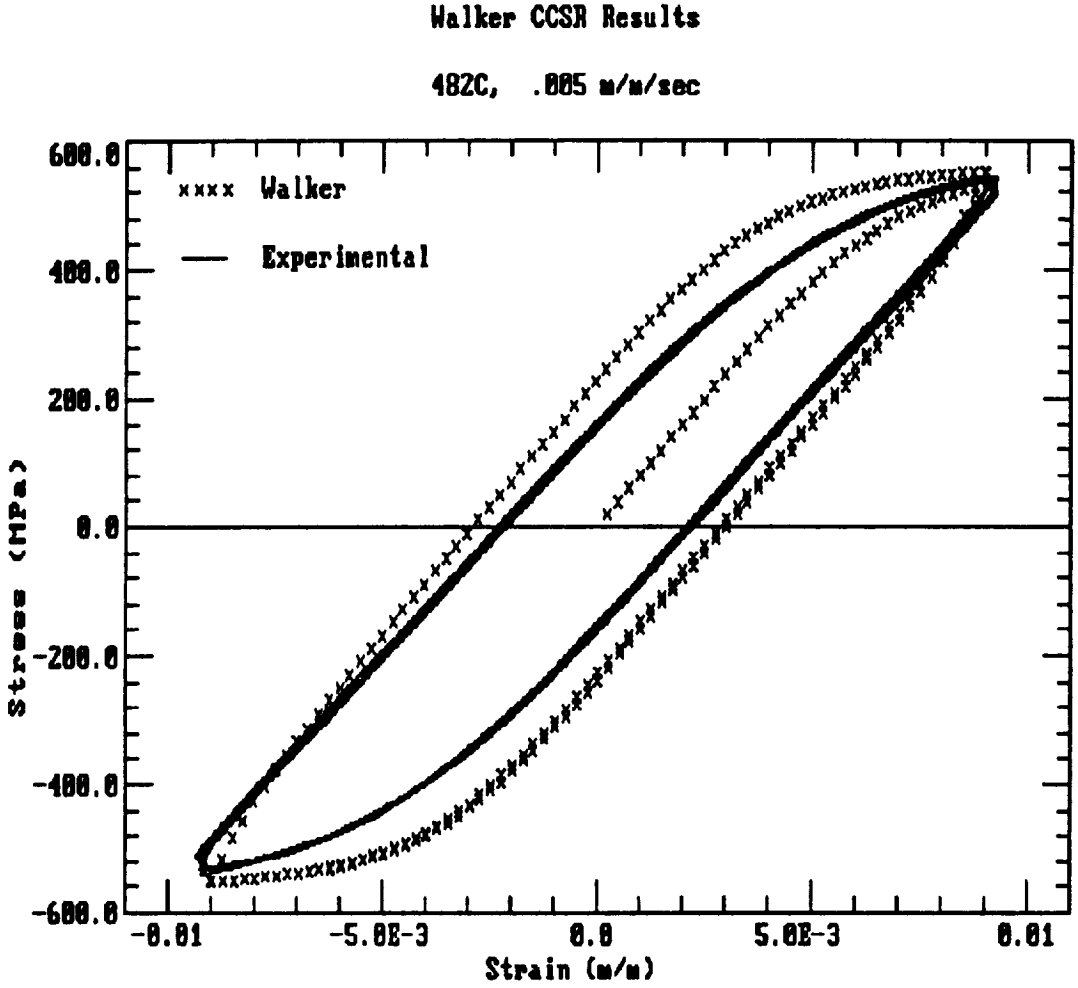

Figure B.55 Walker model prediction vs experimental results for Ti-15-3, CCSR test at 482 C, .005 m/m/sec.

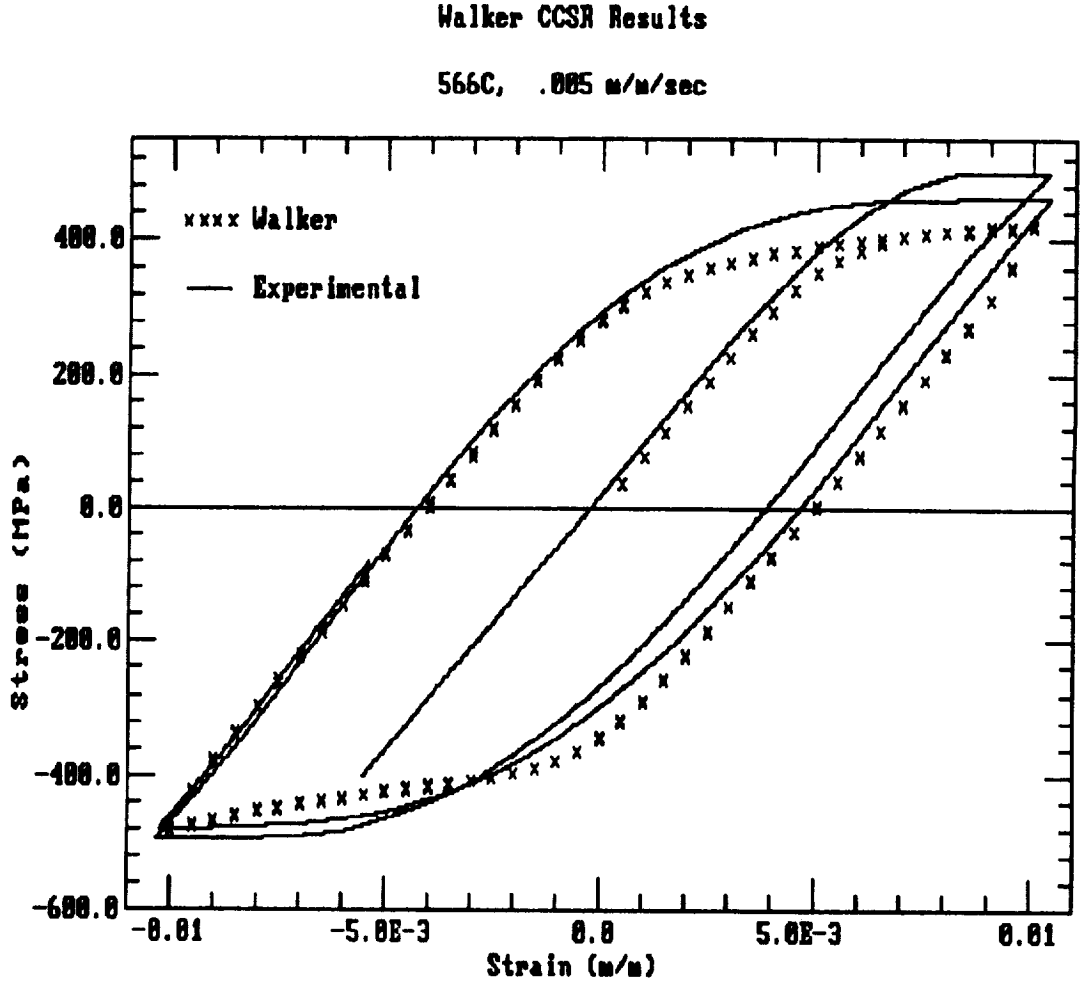

Figure B.56 Walker model prediction vs experimental results for Ti-15-3, CCSR test at 566 C, .005 m/m/sec.

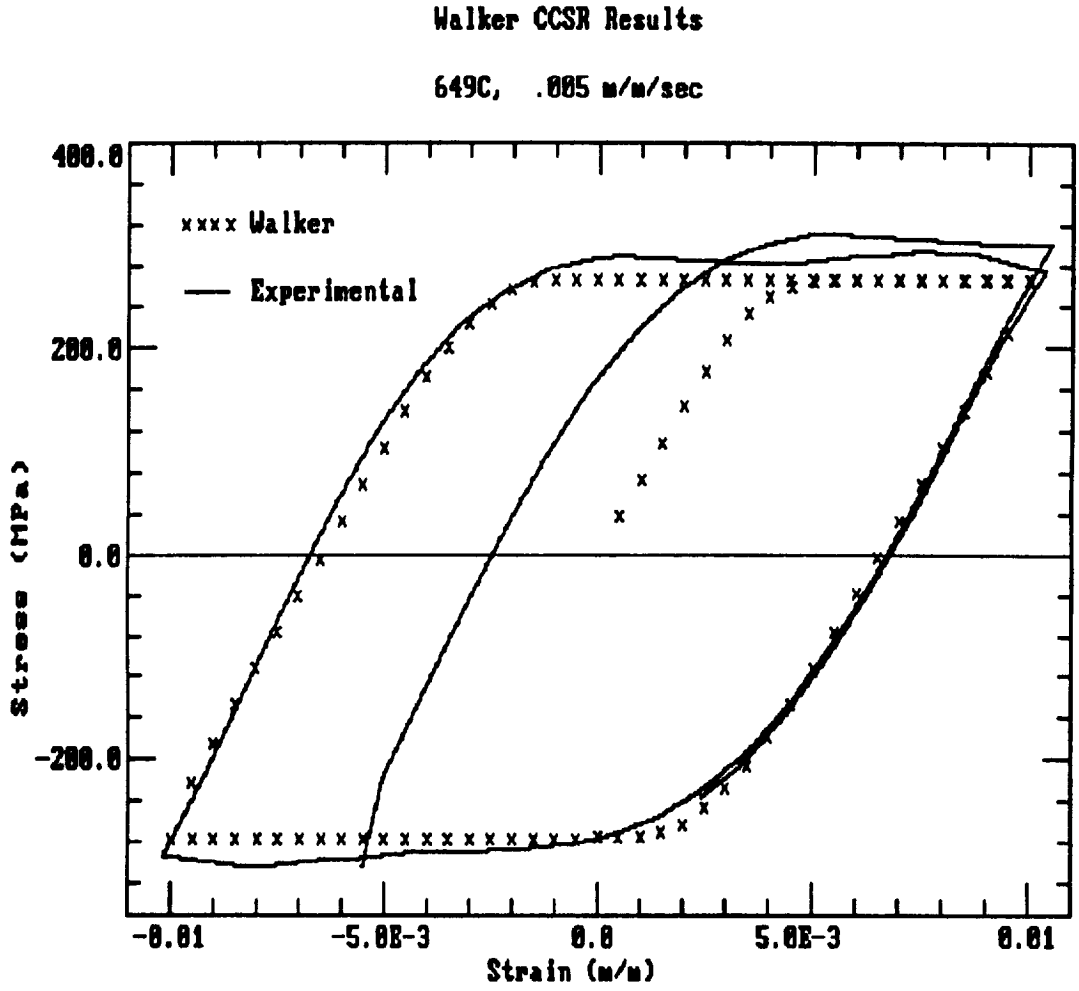

Figure B.57 Walker model prediction vs experimental results for Ti-15-3, CCSR test at 649 C, .005 m/m/sec.

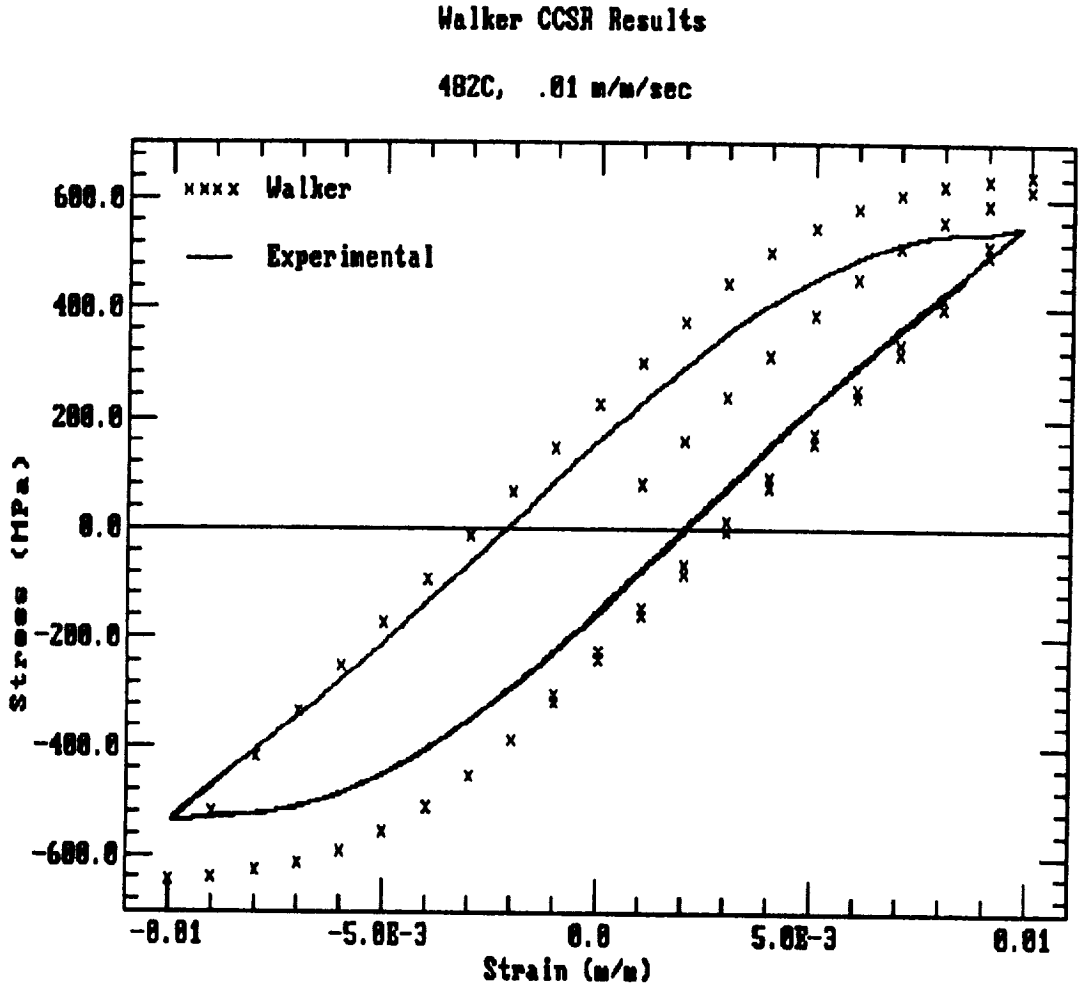

Figure B.58 Walker model prediction vs experimental results for Ti-15-3, CCSR test at 482 C, .01 m/m/sec.

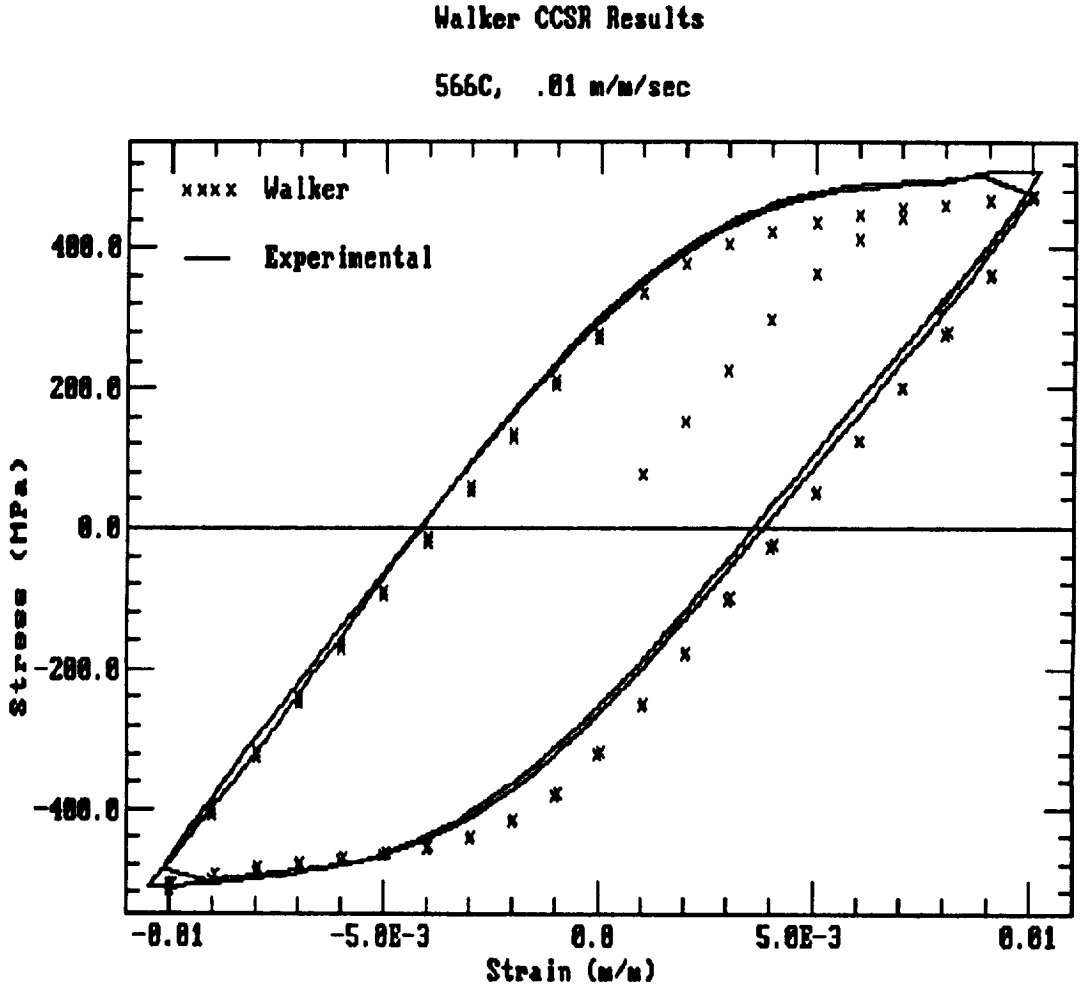

Figure B.59 Walker model prediction vs experimental results for Ti-15-3, CCSR test at 566 C, .01 m/m/sec.

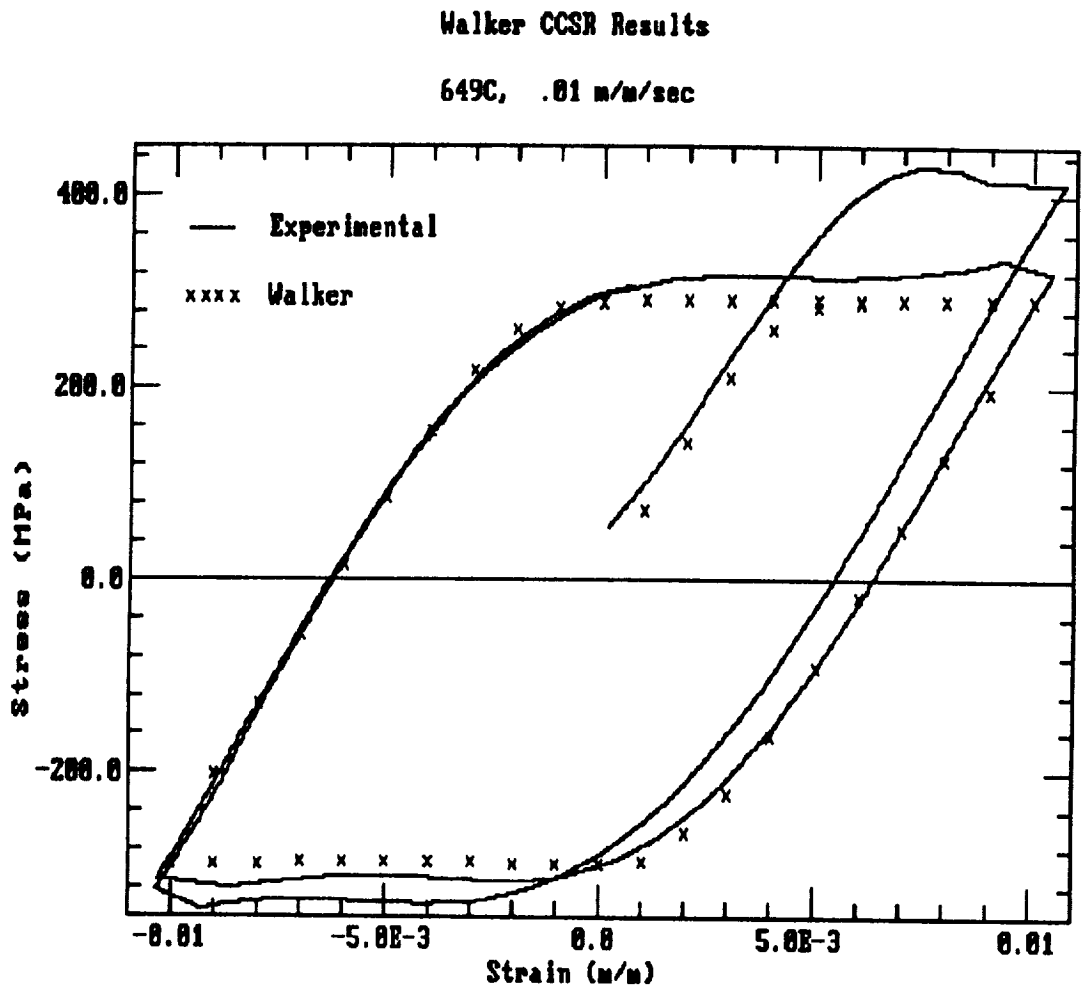

Figure B.60 Walker model prediction vs experimental results for Ti-15-3, CCSR test at 649 C, .01 m/m/sec.

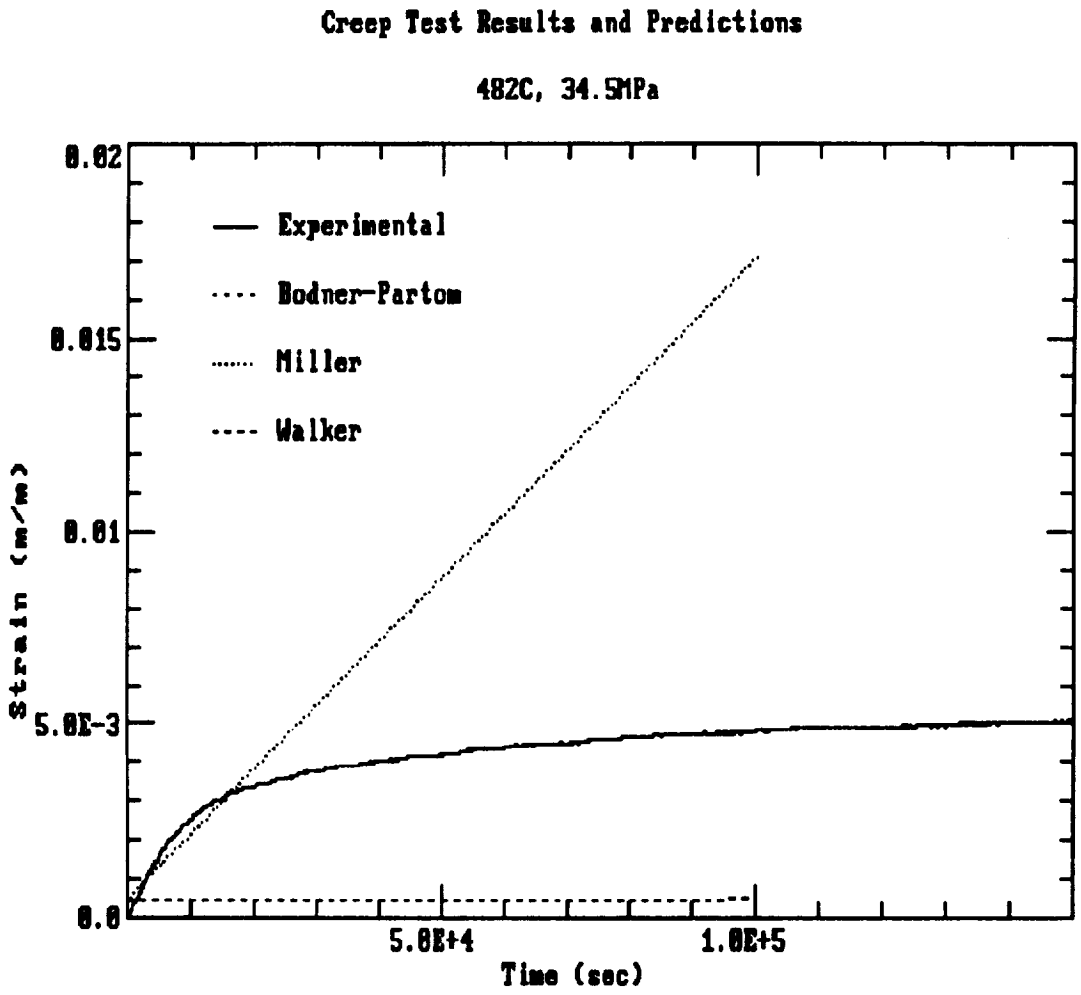

Figure B.61 Experimental results and predicted response for a neat specimen creep test at 482C, 34.5 MPa.

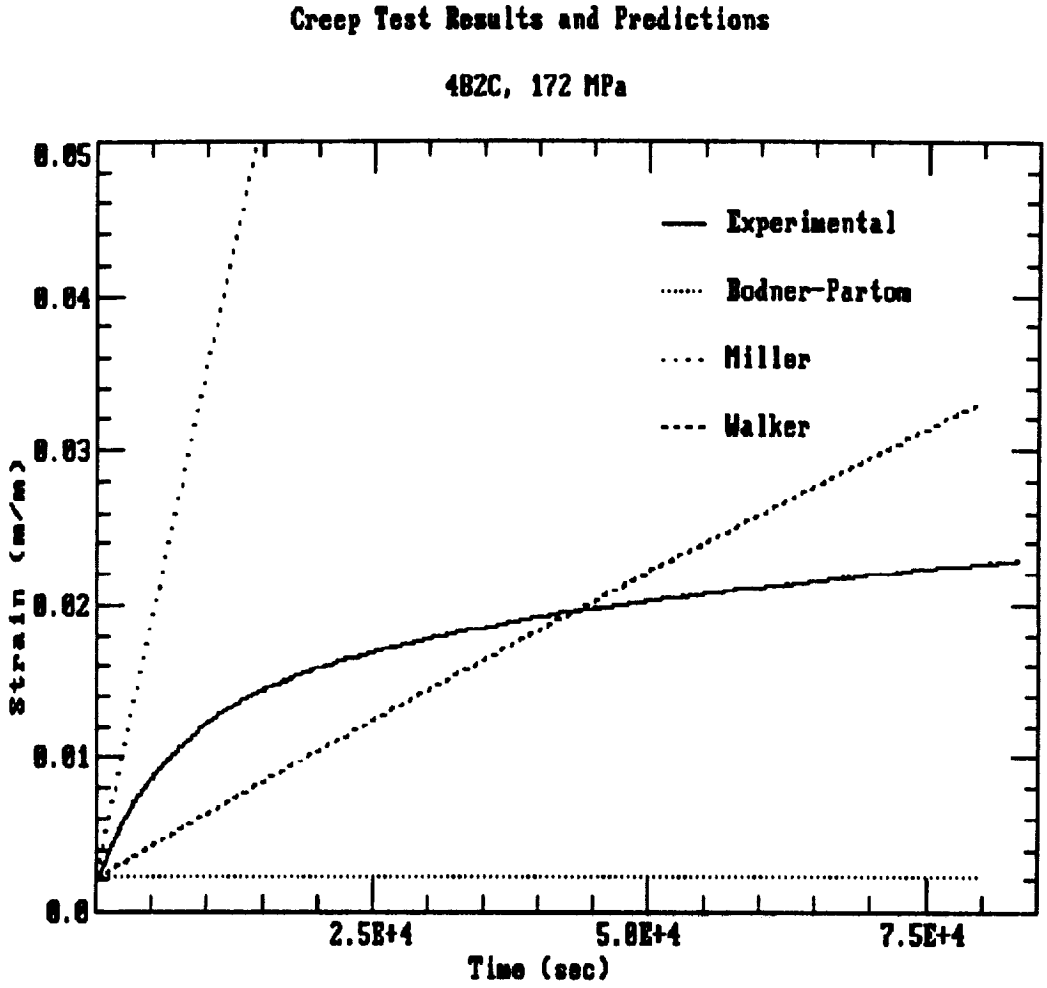

Figure B.62 Experimental results and predicted response for a neat specimen creep test at 482C, 172 MPa.

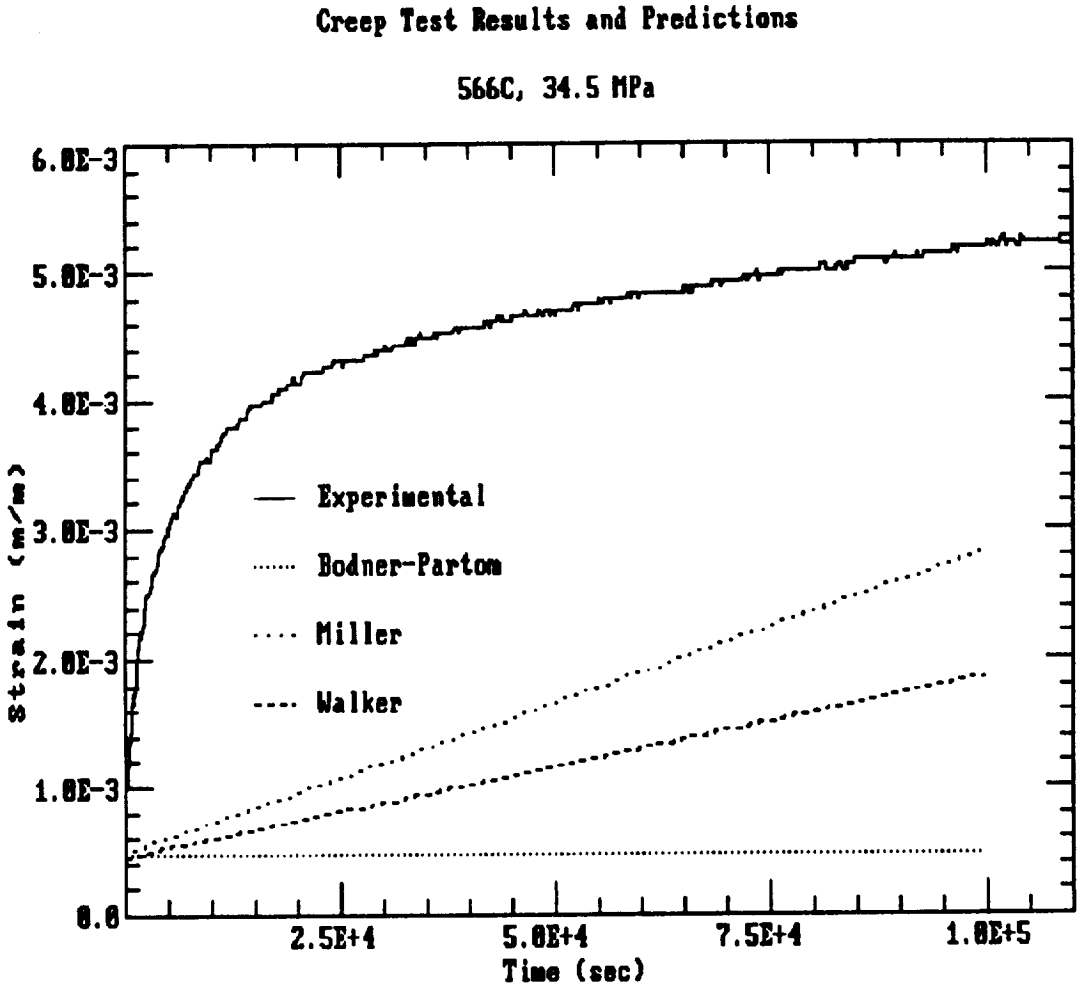

Figure B.63 Experimental results and predicted response for a neat specimen creep test at 5666C, 34.5 MPa.

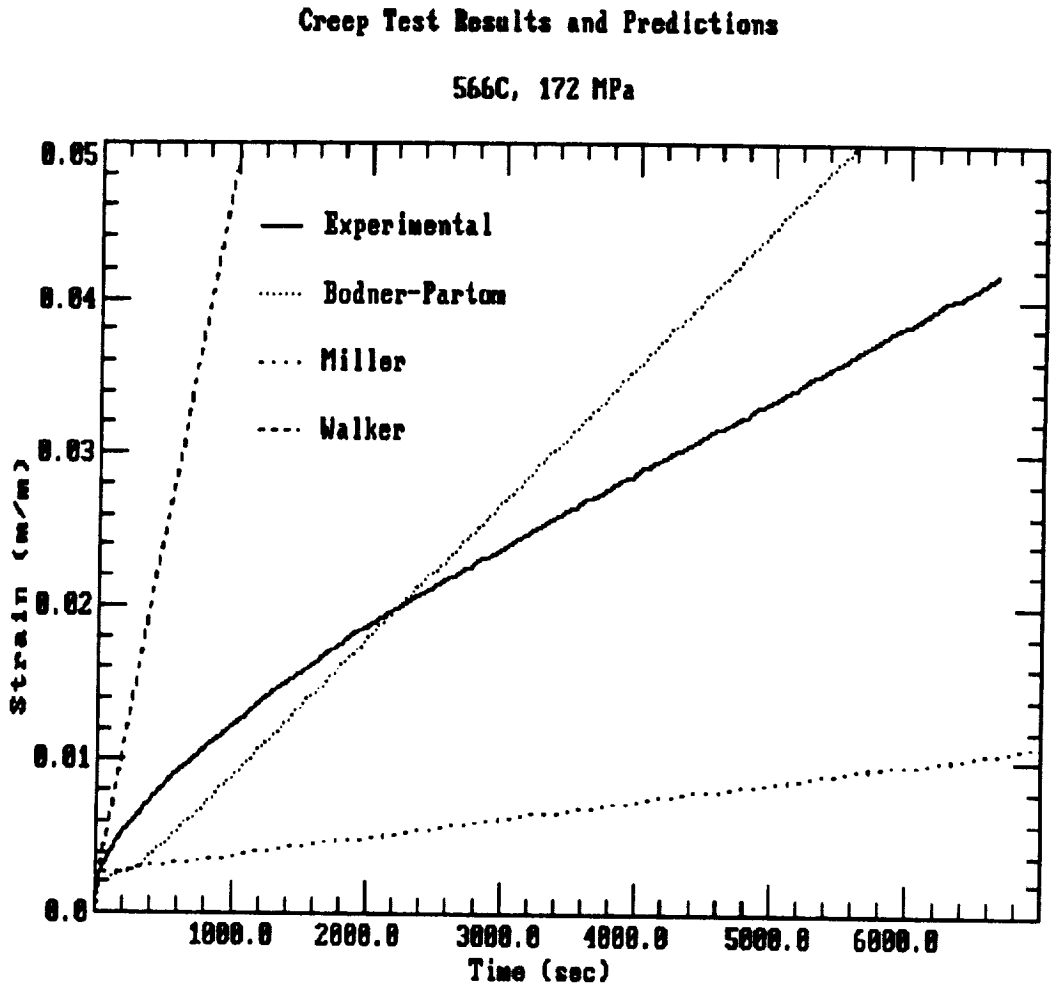

Figure B.64 Experimental results and predicted response for a neat specimen creep test at 566C, 172 MPa.

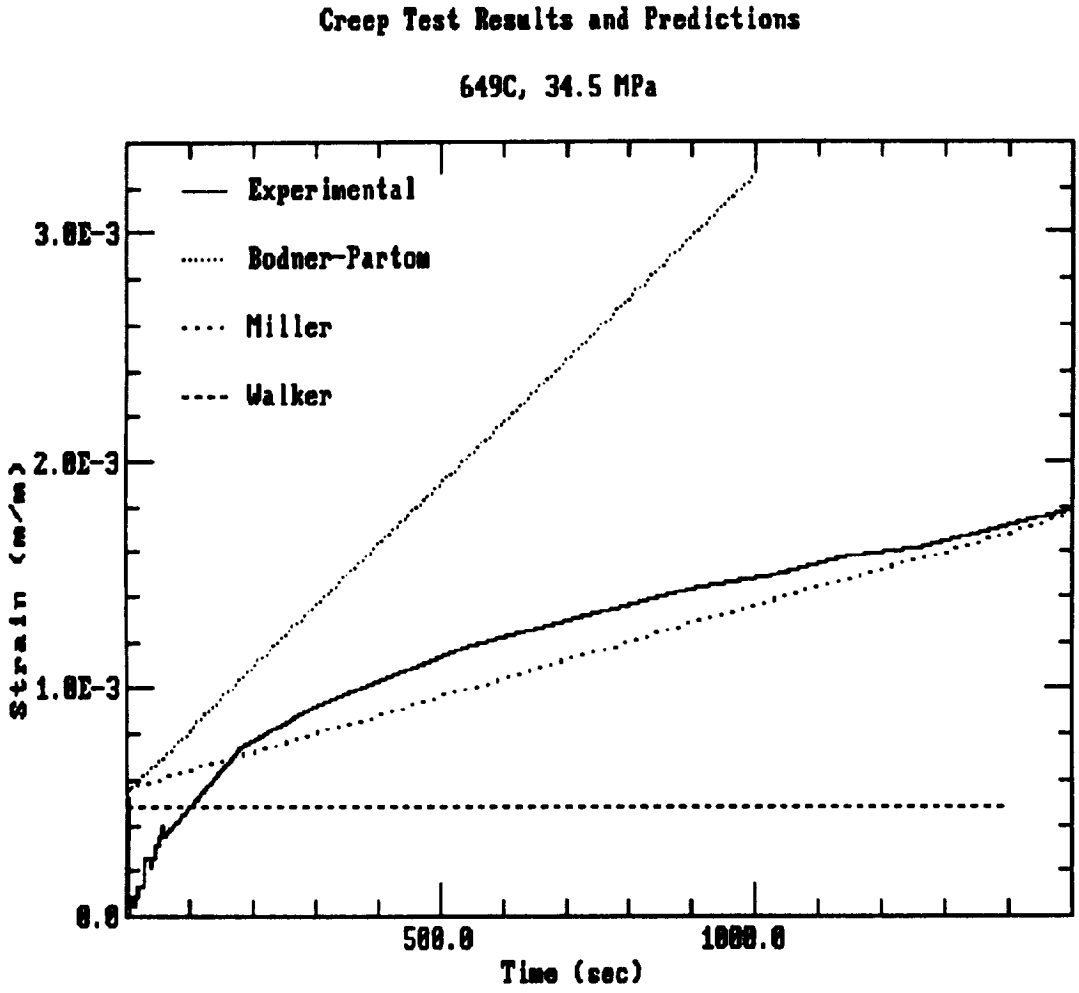

Figure B.65 Experimental results and predicted response for a neat specimen creep test at 649C, 34.5 MPa.

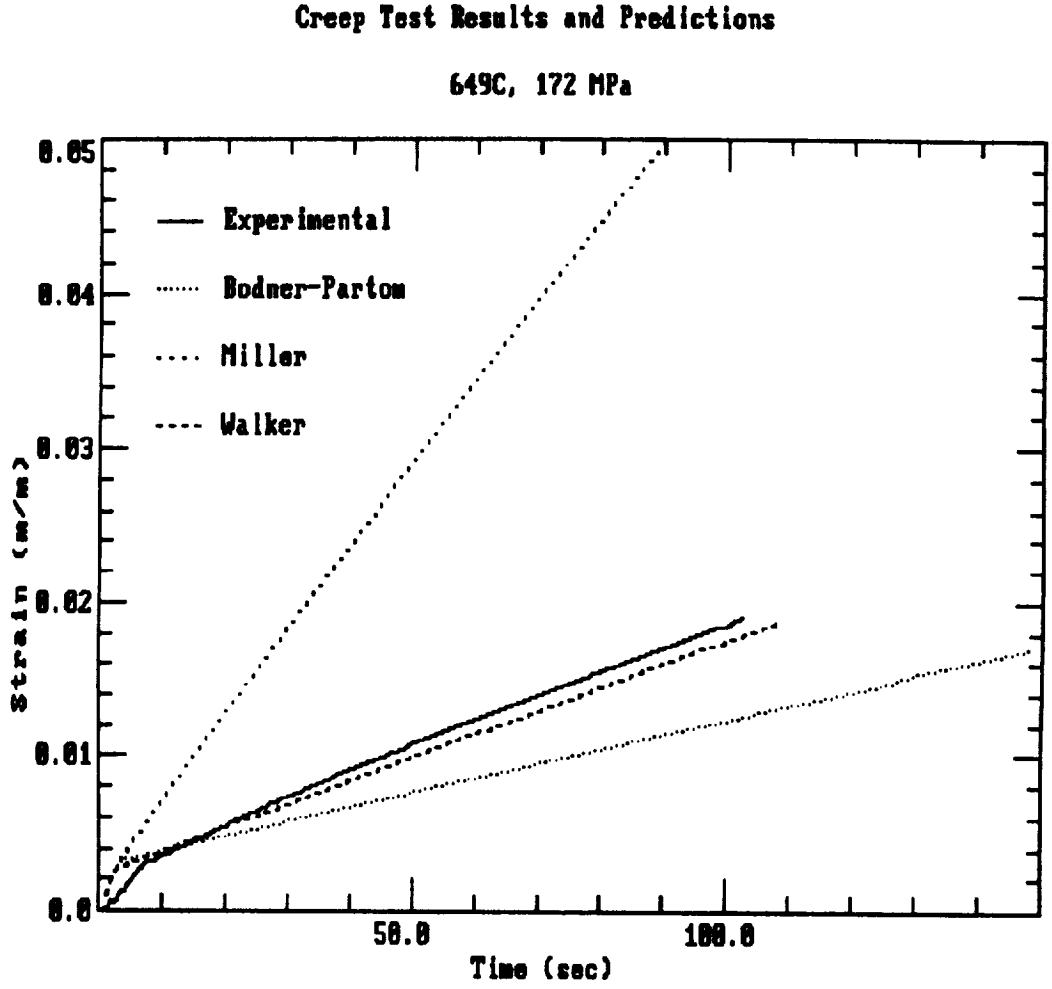

Figure B.66 Experimental results and predicted response for a neat specimen creep test at 649C, 172 MPa.

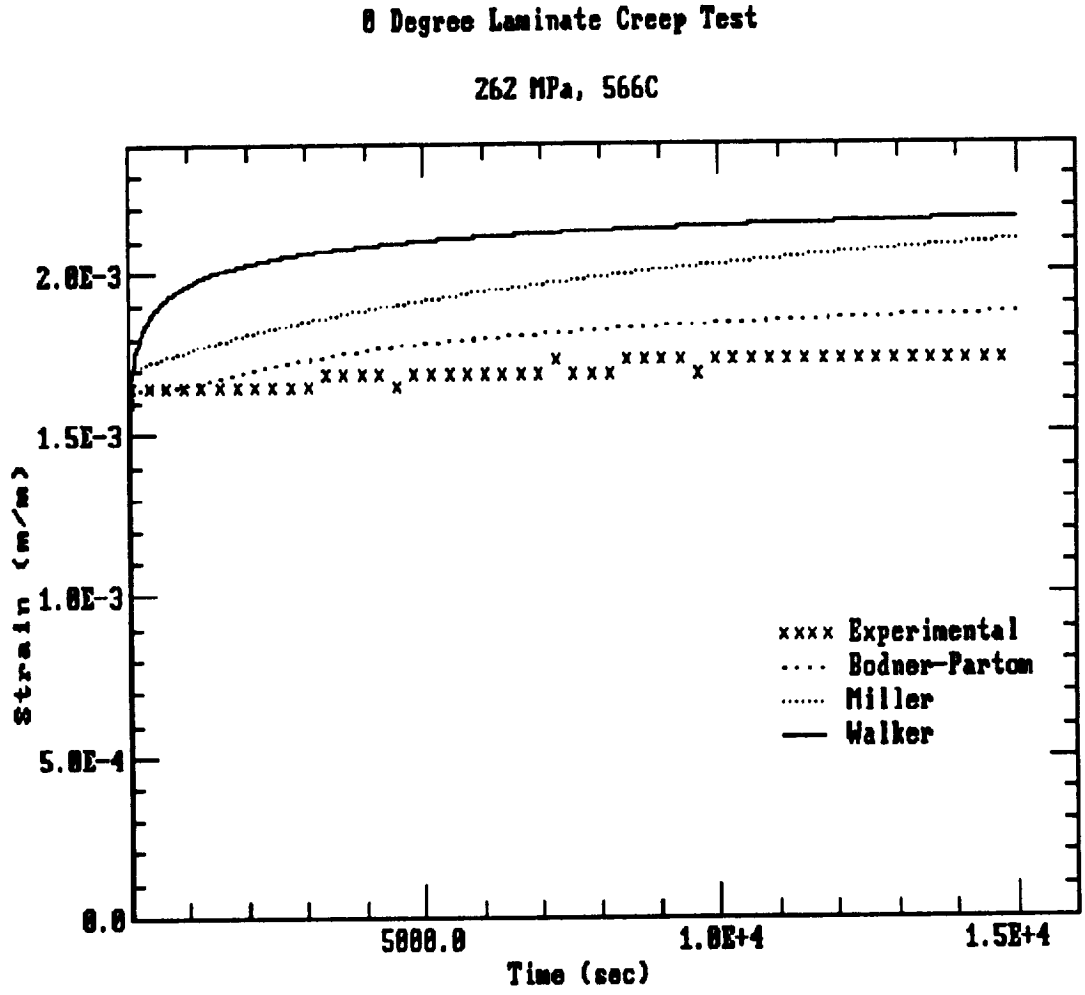

Figure B.67 Experimental results and predicted creep response of a .29 V_f 0 laminate at 566 C and 262 MPa

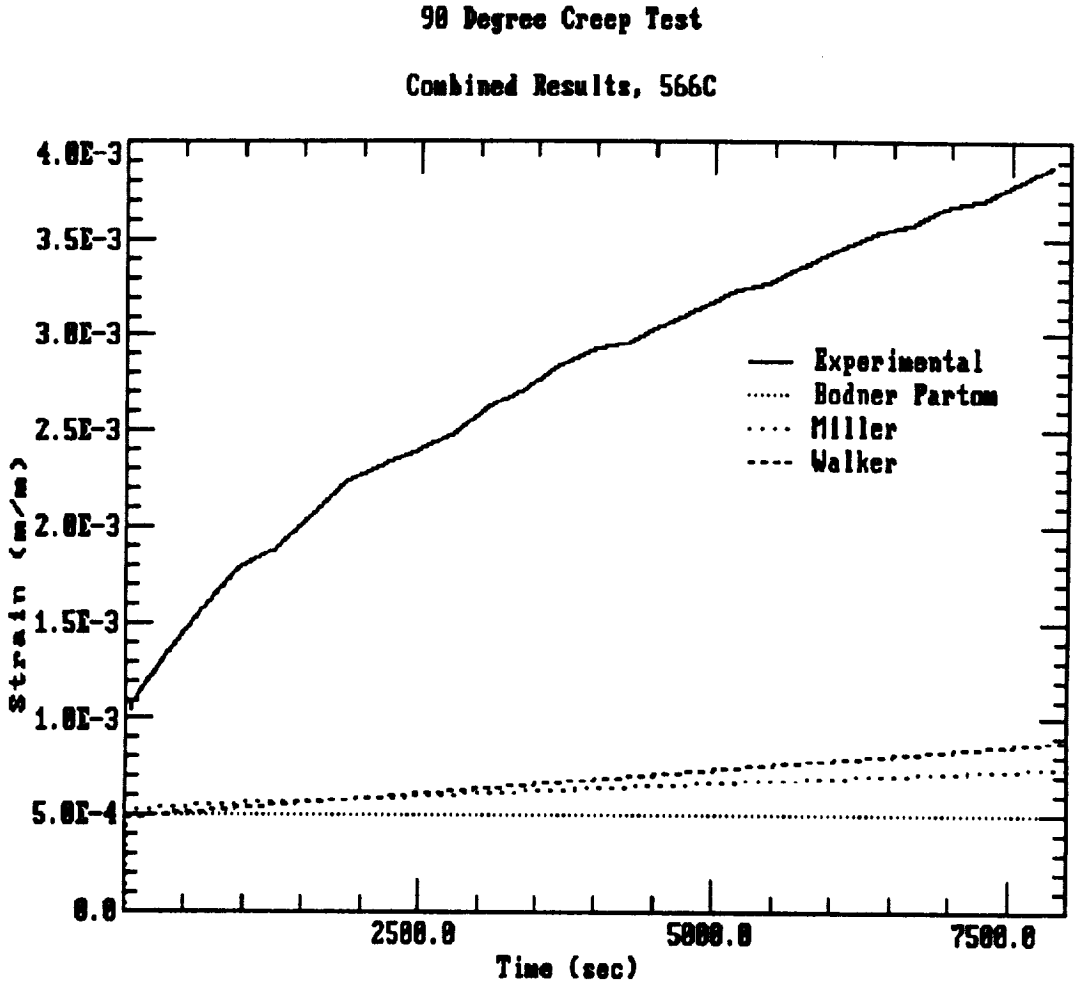

Figure B.68 Experimental results and predicted creep response of a .29 V_f 90 laminate at 566 C and 48.3 MPa

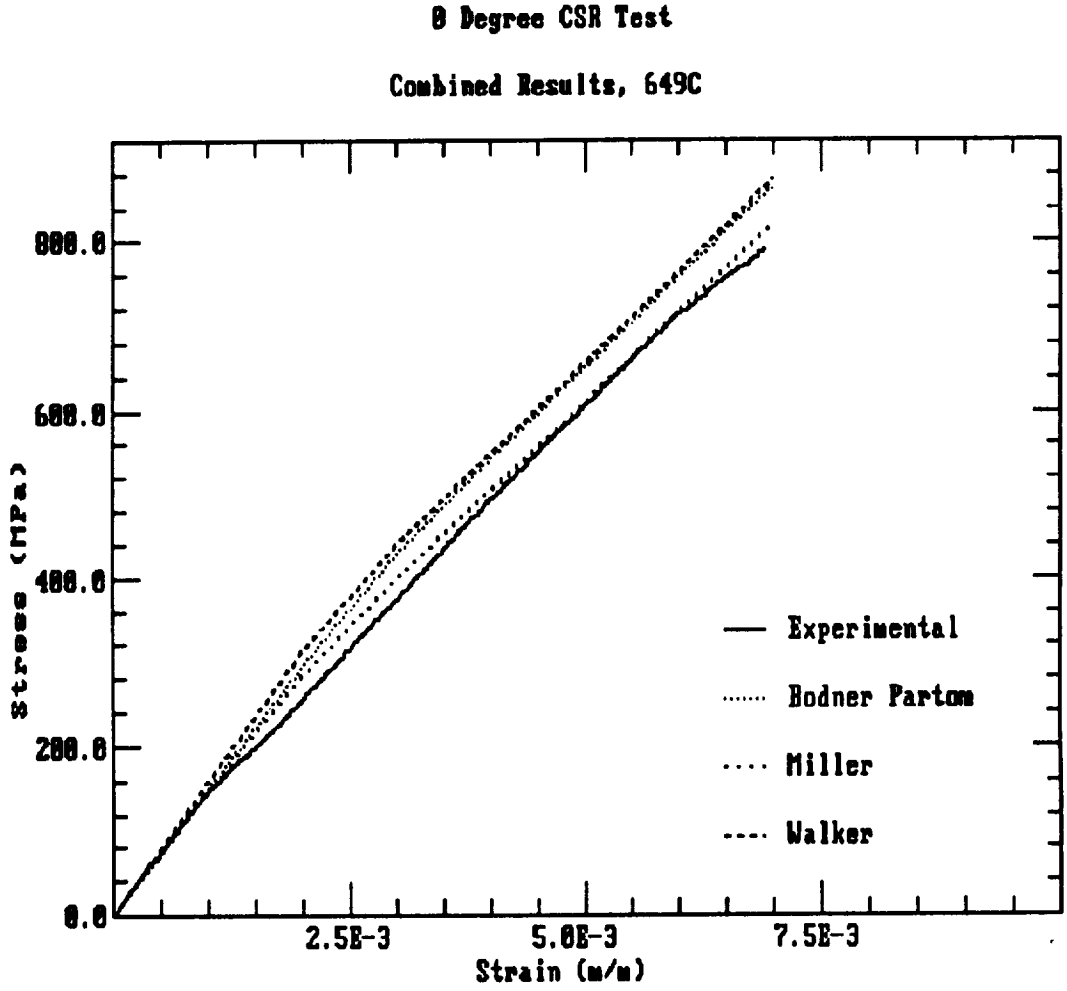

Figure B.69 Experimental results and predicted response of a .29 V_f 0 laminate at 649 C and a strain rate of .0001 m/m/sec.

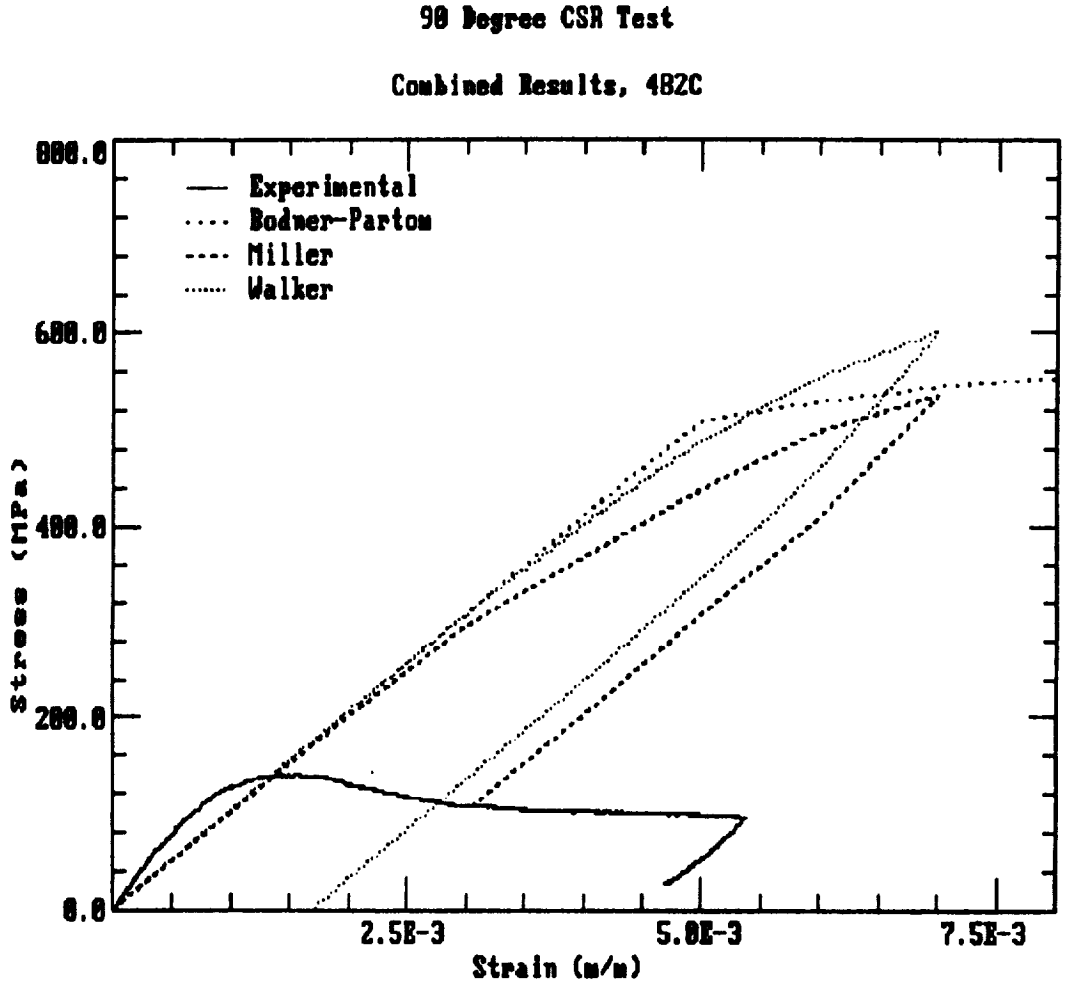

Figure B.70 Experimental results and predicted response of a .29 V_f 90 laminate at 482 C and a strain rate of .0001 m/m/sec.

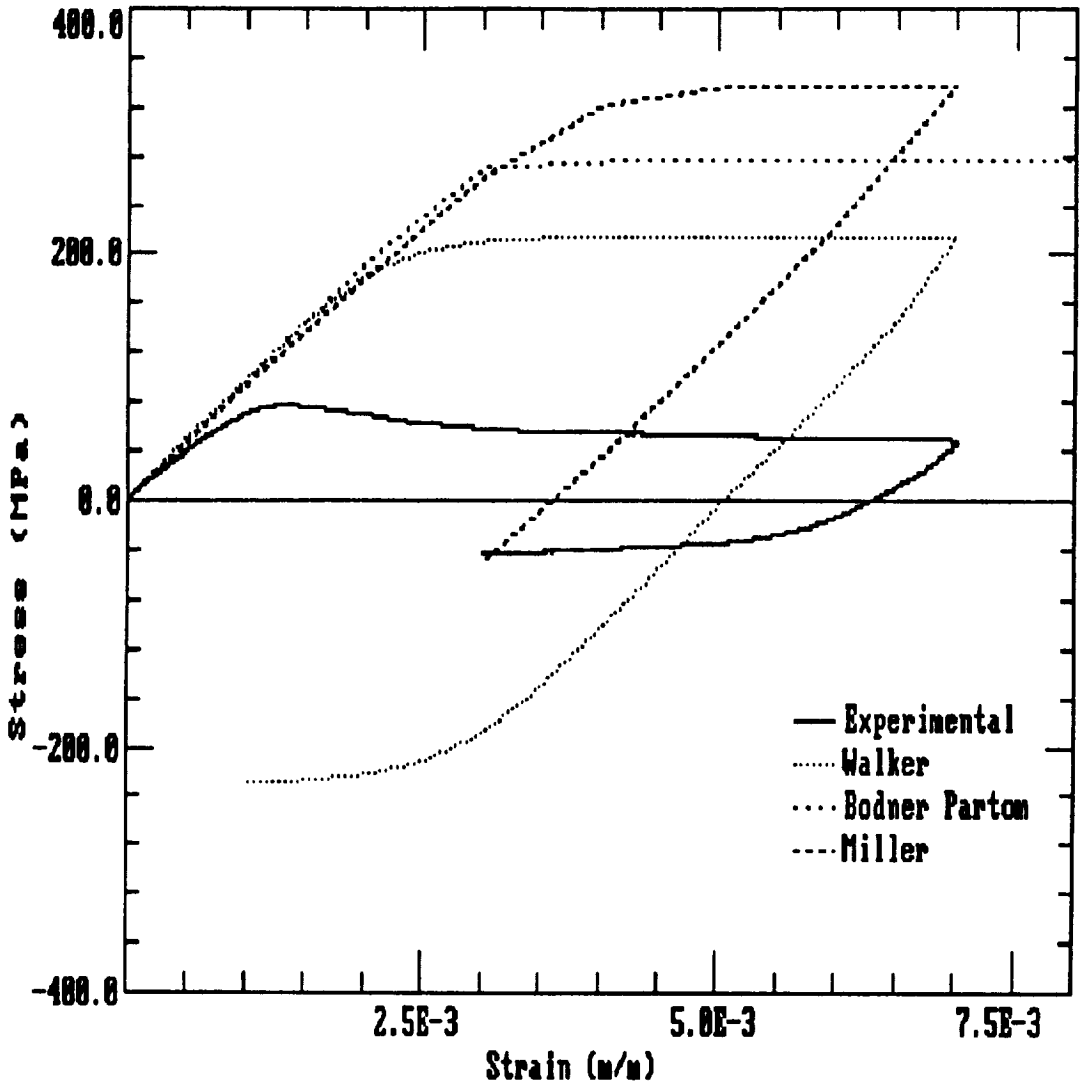

Figure B.71 Predicted response of a .29 V_f 90 laminate at 566 C and a strain rate of .0001 m/m/sec.

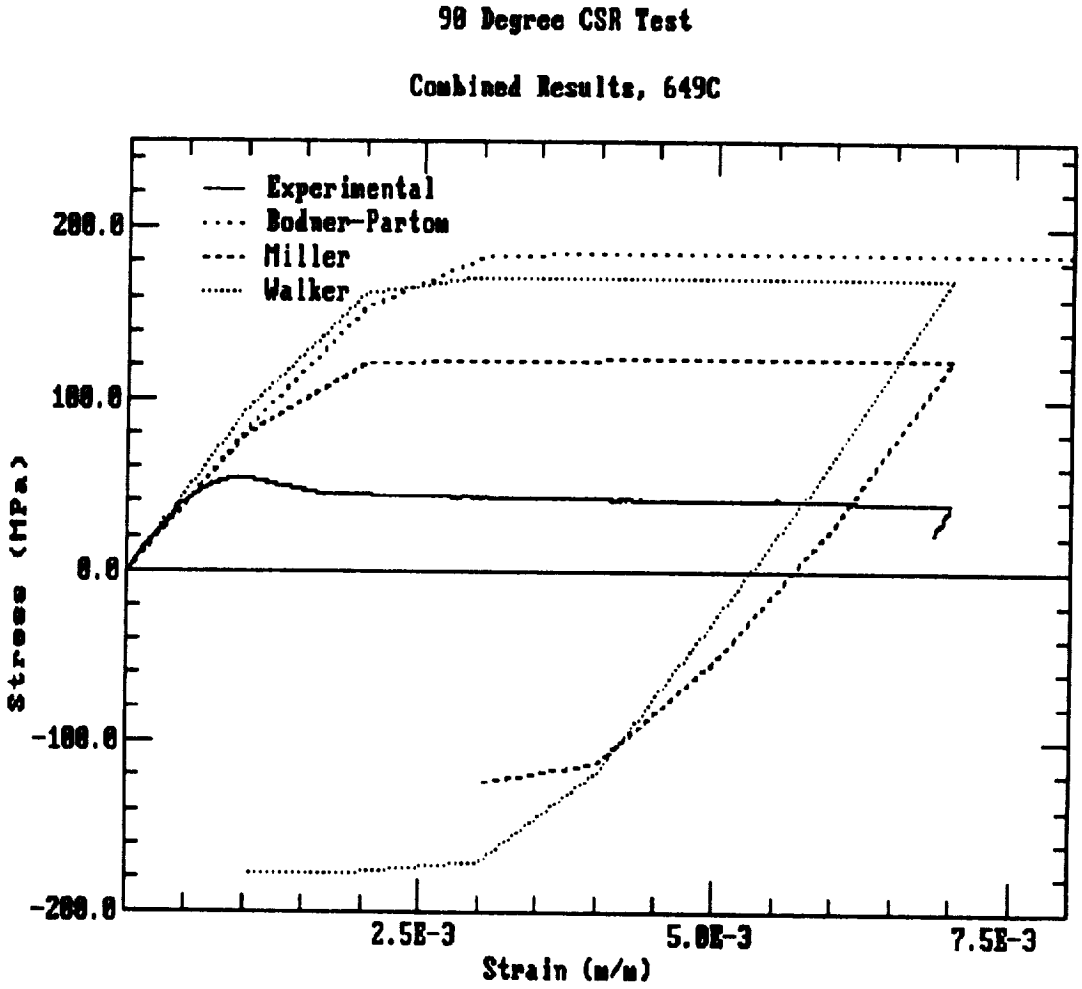

Figure B.72 Predicted response of a .29 V_f 90 laminate at 649 C and a strain rate of .0001 m/m/sec.

REPORT DOCUMENTATION PAGE

Form Approved
OMB No. 0704-0188

1. AGENCY USE ONLY *(Leave blank)*	2. REPORT DATE	3. REPORT TYPE AND DATES COVERED
	October 1992	Contractor Report

4. TITLE AND SUBTITLE
An Investigation of the Thermoviscoplastic Behavior of a Metal Matrix Composite at Elevated Temperatures

5. FUNDING NUMBERS
G NAG1-974
WU 505-63-50-04

6. AUTHOR(S)
John R. Rogacki and Mark E. Tuttle

7. PERFORMING ORGANIZATION NAME(S) AND ADDRESS(ES)
University of Washington
Department of Mechanical Engineering, FU-10
Seattle, WA 98195

8. PERFORMING ORGANIZATION REPORT NUMBER

9. SPONSORING / MONITORING AGENCY NAME(S) AND ADDRESS(ES)
National Aeronautics and Space Administration
Langley Research Center
Hampton, VA 23681

10. SPONSORING / MONITORING AGENCY REPORT NUMBER
NASA CR-189706

11. SUPPLEMENTARY NOTES
Langley Technical Monitor: W. S. Johnson
John R. Rogacki, Research Assistant, University of Washington (presently, Assistant Professor, United States Air Force Academy, Colorado). Mark E. Tuttle, Associate Professor, University of Washington.

12a. DISTRIBUTION / AVAILABILITY STATEMENT
Unclassified-Unlimited
Subject Category 24

12b. DISTRIBUTION CODE

13. ABSTRACT *(Maximum 200 words)*

This research investigates the response of a fiberless 13 layer hot isostatically pressed Ti-15-3 laminate to creep, constant strain rate, and cyclic constant strain rate loading at temperatures ranging from 482°C to 649°C. Creep stresses from 48 to 260 MPa and strain rates of .0001 to .01 m/m/sec were used. Material parameters for three unified constitutive models (Bodner-Partom, Miller, and Walker models) were determined for Ti-15-3 from the experimental data.

Each of the three models was subsequently incorporated into a rule of mixtures and evaluated for accuracy and ease of use in predicting the thermoviscoplastic response of unidirectional metal matrix composite laminates (both 0° and 90°). The laminates were comprised of a Ti-15-3 matrix with 29 volume percent SCS_6 fibers. The predicted values were compared to experimentally determined creep and constant strain rate data. It was found that all three models predicted the viscoplastic response of the 0° specimens reasonably well, but seriously underestimated the visoplastic response of the 90° specimens. It is believed that this discrepancy is due to compliant and/or weak fiber-matrix interphase.

In general, it was found that of the three models studied, the Bodner-Partom model was easiest to implement, primarily because this model does not require the use of cyclic constant strain rate tests to determine the material parameters involved. However, the version of the Bodner-Partom model used in this study does not include back stress as an internal state variable, and hence may not be suitable for use with materials which exhibit a pronounced Baushinger effect. The back stress is accounted for in both the Walker and Miller models; determination of the material parameters associated with the Walker model was somewhat easier than in the Miller model.

14. SUBJECT TERMS	15. NUMBER OF PAGES
Metal matrix composites; Thermoviscoplasticity; Titanium; Creep; Bodner-Partom model; Miller model; Walker model	160
	16. PRICE CODE: A08

17. SECURITY CLASSIFICATION OF REPORT	18. SECURITY CLASSIFICATION OF THIS PAGE	19. SECURITY CLASSIFICATION OF ABSTRACT	20. LIMITATION OF ABSTRACT
Unclassified	Unclassified		